Current-Drive on the Versator II Tokamak
with a Slotted-Waveguide Fast-Wave Coupler

Colborn, J.A.

Plasma Fusion Center
Massachusetts Institute of Technology
Cambridge, MA 02139

November 1987

CURRENT-DRIVE ON THE VERSATOR-II TOKAMAK WITH A
SLOTTED-WAVEGUIDE FAST-WAVE COUPLER

by

JEFFREY ALAN COLBORN
B.S., University of California, Berkeley, 1983

Submitted to the
Department of Electrical Engineering and Computer Science
in Partial Fulfillment of the Requirements
for the Degree of

MASTER OF SCIENCE

at the

MASSACHUSETTS INSTITUTE OF TECHNOLOGY

August 31, 1987

© Massachusetts Institute of Technology, 1987

Signature of Author_____
Department of Electrical Engineering
and Computer Science
August 31, 1987

Certified by_____
Professor Ronald R. Parker
Thesis Supervisor

Accepted by_____
Professor Arthur C. Smith
Chairman, Departmental Committee
on Graduate Students

CURRENT-DRIVE ON THE VERSATOR-II TOKAMAK WITH A SLOTTED-WAVEGUIDE FAST-WAVE COUPLER

by

JEFFREY ALAN COLBORN

Submitted to the Department of Electrical Engineering and Computer Science
in September 1987 in Partial Fulfillment of the Requirements
for the Degree of Master of Science

ABSTRACT

A slotted-waveguide fast-wave coupler has been constructed, without dielectric, and used to drive current on the Versator-II tokamak. Up to 35 kW of net microwave power at 2.45 GHz has been radiated into plasmas with $2 \times 10^{12} \mathrm{cm}^{-3} \leq \bar{n}_e \leq 1.2 \times 10^{13} \mathrm{cm}^{-3}$ and $B_{tor} \approx 1.0$ T. The launched spectrum had a peak near $N_{\parallel} = -2.0$ and a larger peak near $N_{\parallel} = 0.7$. Radiating efficiency of the antenna was roughly independent of antenna position except when the antenna was at least 0.2 cm outside the limiter, in which case the radiating efficiency slightly improved as the antenna was moved farther outside. When the coupler was inside the limiter, radiating efficiency improved moderately with increased $\bar{n}_e$. Current-drive efficiency was comparable to that of the slow wave and was not affected when the antenna spectrum was reversed; however, no current was driven for $\bar{n}_e \leq 2 \times 10^{12} \mathrm{cm}^{-3}$. These results indicate the fast wave was launched, but a substantial part of the power may have been mode-converted to the slow wave, possibly via a downshift in $N_{\parallel}$, and these slow waves may have been responsible for most of the driven current. Relevant theory for waves in plasma, current-drive efficiency, and coupling of the slotted-waveguide is discussed, the antenna design method is explained, and future work, including the construction of a much-improved probe-fed antenna, is described.

Thesis Supervisor: Dr. Ronald R. Parker
Titles: Professor of Electrical Engineering
Associate Director, MIT Plasma Fusion Center

ACKNOWLEDGEMENTS

CONTENTS

FIGURES

5

1 BACKGROUND AND THEORY OF CURRENT-DRIVE

1.1 Magnetic Fusion and Current-Drive

Nuclear Fusion is the workhorse of the Universe. It supplies energy to the sun and stars, making them shine and preventing their collapse. In an effort to harness this energy source, physicists and engineers have been developing fusion since the early 1950s. The easiest fusion reaction to accomplish is that of deuterium nuclei (or ions), which consist of one proton and one neutron, with tritium nuclei, which consist of one proton and two neutrons:

$$D^+ + T^+ \longrightarrow He^{2+} + n + 17.6 \text{ MeV}$$
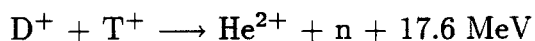
where He^{2+} is a helium nucleus, n is a neutron, 17.6 MeV is the energy released per reaction, and the superscripts indicate charge. This reaction requires some energy input. For the nuclei to fuse, the Coulomb repulsive force must be overcome and the ions brought together to within $\sim 10^{-15}$ meters. At this distance the nuclear strong force, an attractive force, can overcome the Coulomb repulsion and pull the nuclei together.

In magnetic fusion, the repulsive force is overcome by confining the ions by a magnetic field and heating them to extremely high temperatures, forming a plasma. The quality of a fusion plasma is measured by its ion temperature and Lawson parameter,[1] which is the product of the plasma density n, and energy confinement time τ. The energy confinement time is defined in equilibrium as the total plasma energy divided by the total power input to (or loss from) the plasma. For an economically feasible fusion reactor, the Lawson parameter must be greater than about $10^{14} \text{cm}^{-3} \cdot \text{s}$, and the ion temperature must be about 200,000,000 K.

The most successful magnetic confinement scheme to date has been the toka-
mak (see Figure 1), which was invented by Russian physicists[2] in the 1950s and
is continually being refined and improved. As shown in **Figure 1**, the tokamak
has two components of the magnetic field—a toroidal component directed the long
way around the torus, and a poloidal component circulating the short way around.
These components add to give field lines that twist helically around the tokamak.
Both field components are needed for the equilibrium and stability of the plasma.

The toroidal magnetic field is produced by a set of coils that are outside the
plasma, as shown in Figure 1. The poloidal field is produced by a *toroidal* plasma
current (often several megaamps in contemporary tokamaks). Traditionally, this
current has been generated via induction, the plasma being a one-turn secondary
coil of a transformer. This current cannot be steady-state, because it is proportional
to the time-rate-of-change of the poloidal magnetic flux linked by the plasma (see
Figure 2). That is, the tokamak must be pulsed and the transformer recocked
between pulses. Pulsing a reactor fatigues its structure and lowers its average
power output. If current could be driven noninductively in plasmas, a steady-
state reactor could be realized. Methods have been proposed for driving current
using radiofrequency electromagnetic waves (rf), relativistic electron beams, phased
injection of frozen hydrogen pellets, and oscillating magnetic fields.[3] [4] [5] [6] [7] In
this thesis, I report my investigations on driving current using rf to excite the "fast
lower-hybrid wave" in the Versator-II tokamak.

1.2 Cold-Plasma Wave Theory

The polarization and dispersion of the lower-hybrid fast- and slow-waves can
be obtained for a cold plasma from Maxwell's equations and the fluid or kinetic
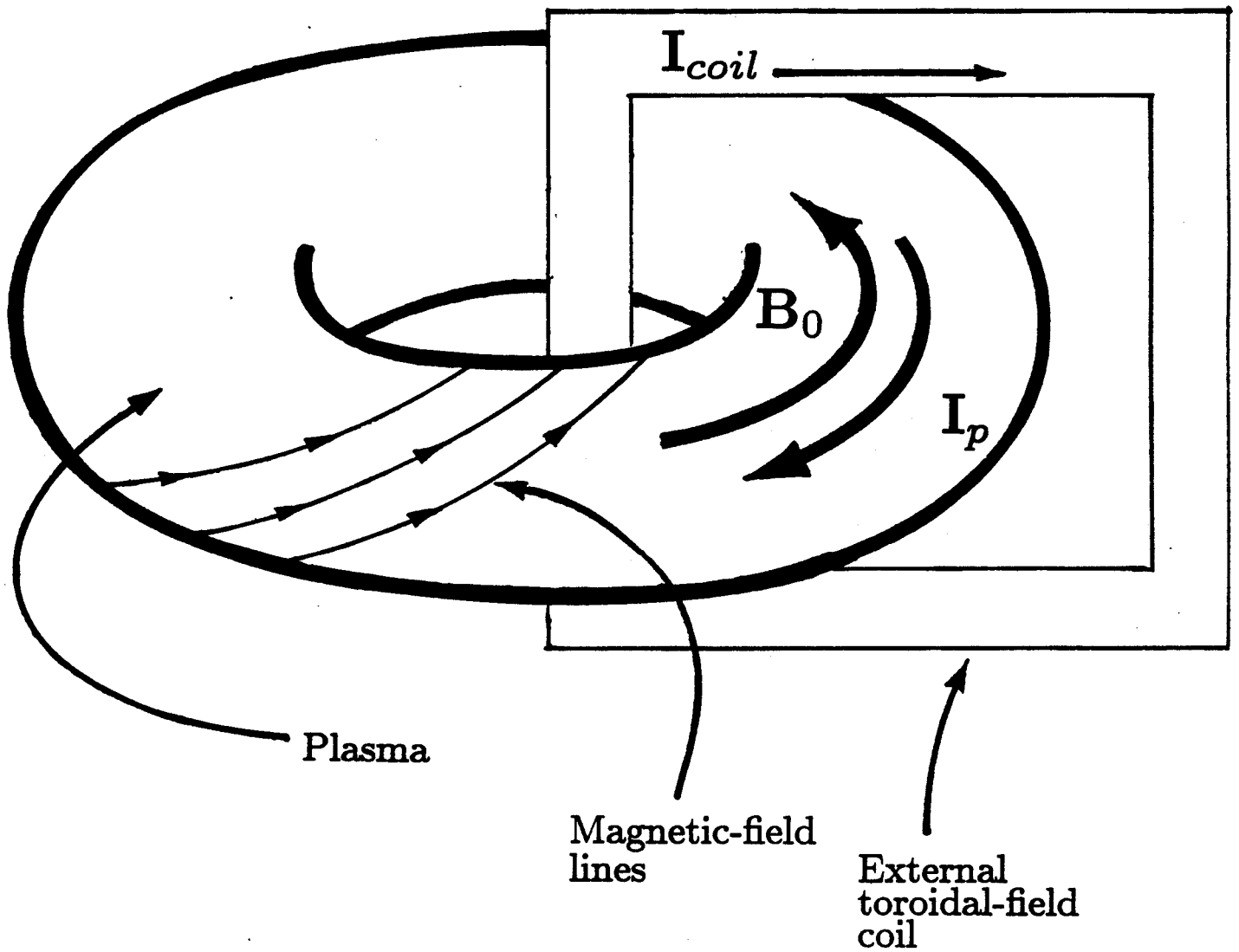
Figure 1: Schematic Diagram of a Tokamak. The toroidal-field coils are spaced uniformly around the torus; only one is shown for clarity.

$$\frac{\partial \mathbf{B}}{\partial t}$$

$v(t)$
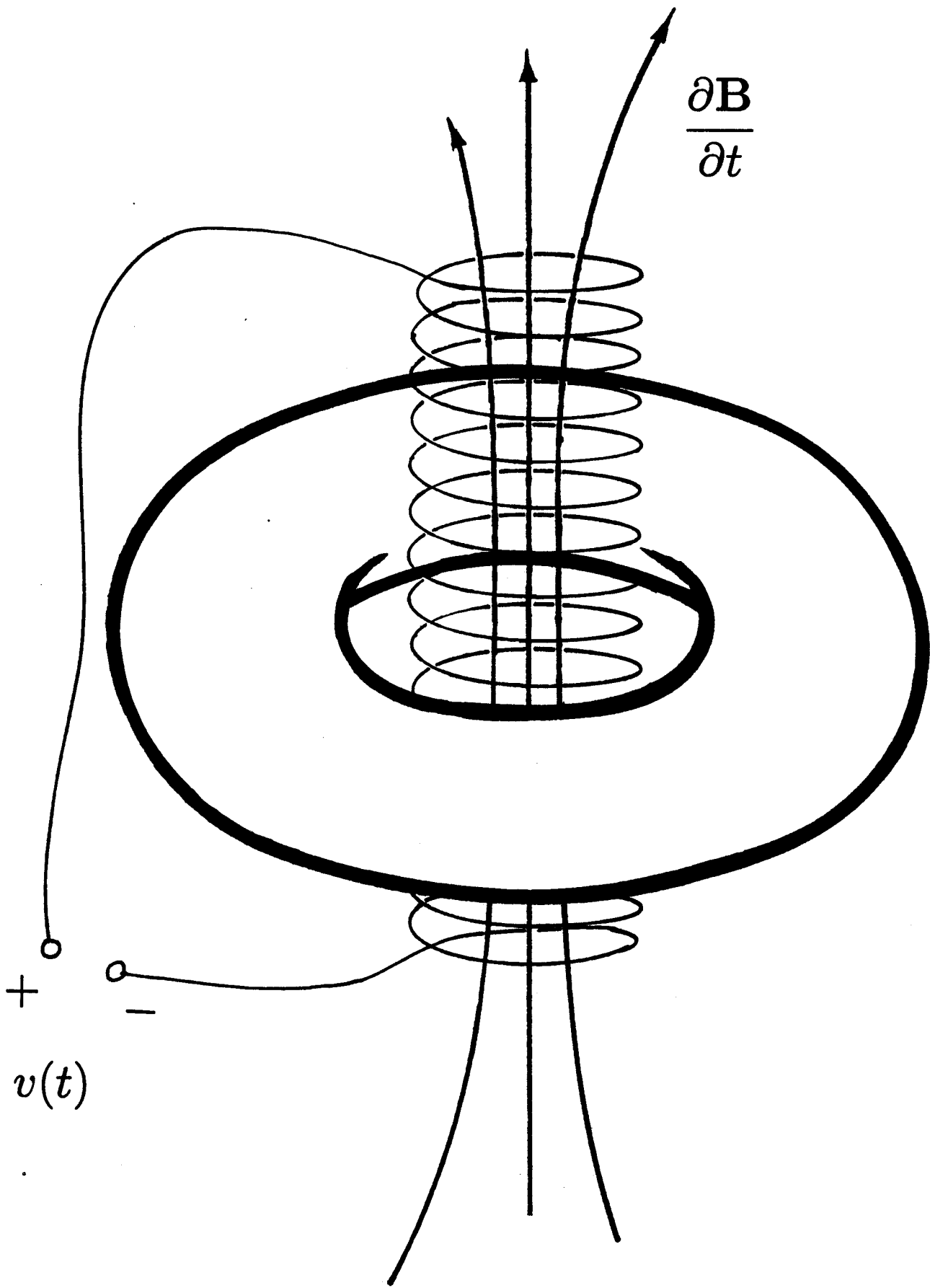
Figure 2:   The transformer circuit of a tokamak.

10

equations. The cold plasma approximation accurately describes the wave dispersion in the current-drive regime because in this regime there are no resonance layers ($k_\perp \to \infty$) in the plasma. Landau damping, the mechanism by which lower-hybrid waves drive current, is a very important thermal effect that does not affect wave dispersion.

Starting with Maxwell's equations, assuming waves varying as $\exp(i\mathbf{k} \cdot \mathbf{r} - i\omega t)$, using the WKB approximation ($|\mathbf{k}| \gg |\partial/\partial \mathbf{r}|$), and assuming a linear, dispersive medium, we obtain the wave equation:

$$\mathbf{k} \times (\mathbf{k} \times \mathbf{E}) + \frac{\omega^2}{c^2}\overline{\overline{\mathbf{K}}} \cdot \mathbf{E} = 0 \tag{1}$$

where the equation has been transformed in time and space, $\mathbf{k}$ is the wave vector, $\mathbf{E}$ is the wave electric-field, ω is the wave frequency, c is the speed of light, and $\overline{\overline{\mathbf{K}}}$ is the dielectric tensor, incorporating free-current effects. It is defined as follows:

$$\overline{\overline{\mathbf{K}}} \cdot \mathbf{E} = \mathbf{E} + \frac{i}{\omega\epsilon_0}\mathbf{J} \tag{2}$$

where $\mathbf{J} = \sum_j n_{j0} Z_j e v_{j1}$ is the plasma current (summed over species), n_0 is the zeroth-order density, Z is the charge state of the species, e is the magnitude of the charge of the electron, and v_1 is the first-order (wave-induced) particle velocity. Applying cold-plasma theory, i. e. , using the fluid equations or the reduced kinetic equations, the dielectric tensor for $\mathbf{B} = \hat{z}B(\mathbf{r})$ becomes

$$\overline{\overline{\mathbf{K}}} = \begin{pmatrix} K_{xx} & K_{xy} & 0 \\ -K_{xy} & K_{xx} & 0 \\ 0 & 0 & K_{zz} \end{pmatrix} \tag{3}$$

11

where

$$K_{xx} = 1 - \frac{\omega_{pe}^2}{\omega^2 - \omega_{ce}^2} - \frac{\omega_{pi}^2}{\omega^2 - \omega_{ci}^2} \tag{4}$$

$$K_{xy} = \frac{i\omega_{ce}}{\omega} \frac{\omega_{pe}^2}{\omega^2 - \omega_{ce}^2} - \frac{i\omega_{ci}}{\omega} \frac{\omega_{pi}^2}{\omega^2 - \omega_{ci}^2} \tag{5}$$

$$K_{zz} = 1 - \frac{\omega_{pe}^2}{\omega^2} - \frac{\omega_{pi}^2}{\omega^2}, \tag{6}$$

$\omega_{pj} = \sqrt{n_j e^2 Z_j^2 / m_j \epsilon_0}$ is the plasma frequency of the jth species (e. g. electrons or hydrogen ions), and $\omega_{cj} = Z_j e B / m_j$ is the cyclotron frequency of the jth species. For the plasma interior (i. e. , *not* in the coupling region), we may assume, without loss of generality, the situation shown in Figure 3, so that $N_\parallel = ck_\parallel/\omega = (ck/\omega)\cos\theta$ and $N_\perp = ck_\perp/\omega = (ck/\omega)\sin\theta$. Substituting into the wave equation, we get

$$\begin{pmatrix} K_{xx} - N_\parallel^2 & K_{xy} & N_\parallel N_\perp \\ -K_{xy} & K_{xx} - N^2 & 0 \\ N_\parallel N_\perp & 0 & K_{zz} - N_\perp^2 \end{pmatrix} \begin{pmatrix} E_x \\ E_y \\ E_z \end{pmatrix} = 0. \tag{7}$$

The dispersion relation is obtained by setting the determinant of this system of equations to zero. This yields the following quadratic equation for $N_\perp^2$:

$$K_{xx}N_\perp^4 + N_\perp^2[(K_{xx} + K_{zz})N_\parallel^2 - (K_{xy}^2 + K_{xx}^2 + K_{xx}K_{zz})] \\ + K_{zz}[(N_\parallel^2 - K_{xx})^2 + K_{xy}^2] = 0. \tag{8}$$

Applying the lower-hybrid approximating condition, $\omega_{ci}^2 \ll \omega^2 \ll \omega_{ce}^2$, yields the following for the dielectric tensor elements:

$$K_{xx} \approx 1 + \frac{\omega_{pe}^2}{\omega_{ce}^2} - \frac{\omega_{pi}^2}{\omega^2} \tag{9}$$

12
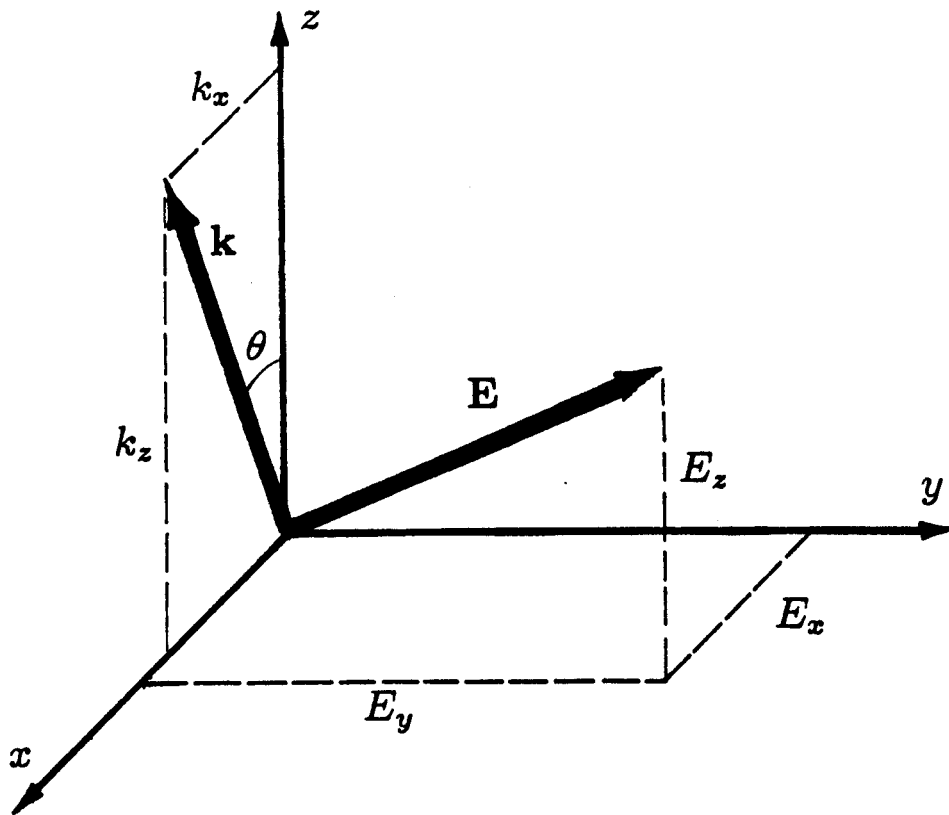
Figure 3: Coordinate system for accessibility calculation in slab geometry.

$$A = \left(\sqrt{K_{zz}} - \sqrt{K_{zy}^2/K_{zz}} \right)^2$$

$$B = \left(\sqrt{K_{zz}} + \sqrt{K_{zy}^2/K_{zz}} \right)^2$$
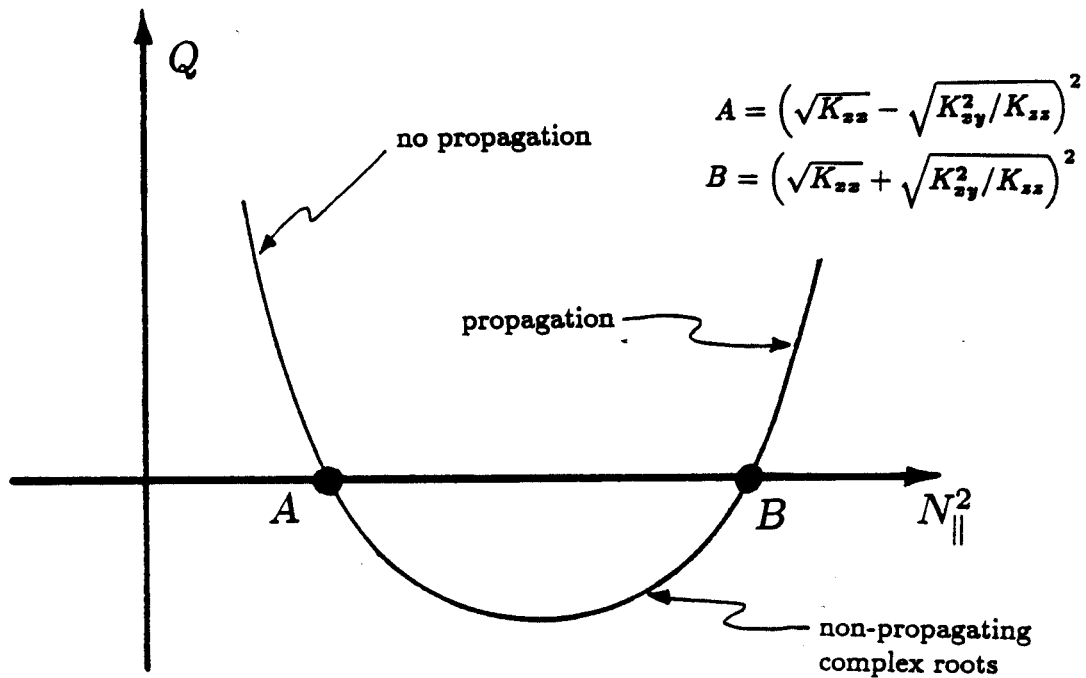
Figure 4: Q versus $N_\parallel^2$ for accessibility.

$$K_{xy} \approx \frac{-i\omega_{pe}^2}{\omega\omega_{ce}} \tag{10}$$

$$K_{zz} \approx 1 - \frac{\omega_{pe}^2}{\omega^2} \tag{11}$$

Making the further approximations that $|K_{zz}| \gg K_{xx}$ and $|K_{xy}^2| \gg (N_\parallel^2 - K_{xx})^2$ yields the following dispersion relation[8] :

$$\frac{2K_{xx}}{-K_{zz}}N_\perp^2 = N_\parallel^2 - \left(K_{xx} + \frac{K_{xy}^2}{K_{zz}}\right)$$

$$\pm\sqrt{\left[N_\parallel^2 - (\sqrt{K}_{xx} + \sqrt{K_{xy}^2/K_{zz}})^2\right]\left[N_\parallel^2 - (\sqrt{K}_{xx} - \sqrt{K_{xy}^2/K_{zz}})^2\right]} \tag{12}$$

Calling the quantity under the large radical Q, we get the situation shown in Figure 4. Requiring $N_\perp^2$ to be positive yields the following condition on $N_\parallel$:[8]

$$N_\parallel^2 > \left[\frac{\omega_{pi}}{\sqrt{\omega_{ci}\omega_{ce}}} + \sqrt{1 + \frac{\omega_{pi}^2}{\omega_{ci}\omega_{ce}}\left(1 - \frac{\omega_{ci}\omega_{ce}}{\omega^2}\right)}\right]^2. \tag{13}$$

Waves are evanescent in regions of the plasma for which the above inequality is violated. Making an equality out of it and solving for ω_{pi} gives the density at which the fast and slow wave roots coalesce, i. e. , the mode-conversion layer. Here an inward-propagating fast wave is converted to an outward-propagating slow wave:[9]

$$\frac{\omega_{pi}}{\omega} = N_\parallel Y \pm \sqrt{1 + N_\parallel^2(Y^2 - 1)} \tag{14}$$

where $Y^2 = \omega^2/\omega_0^2$ and $\omega_0^2 = \omega_{ce}\omega_{ci}$. Curves showing the accessibility condition for the fast and slow waves with $Y^2 < 1$ are shown in Figure 5.[10] For $Y^2 > 1$ the

14

accessibility curve looks like the left half of Figure 5a. For $Y^2 < 1$ as shown in Figure 5, a local maxima of Equation 13 exists at $\omega_{pi}^2/\omega^2 = Y^2/(1 - Y^2)$ where

$$N_{\|min} = \frac{1}{\sqrt{1 - Y^2}} \tag{15}$$

Propagation to higher densities requires no further increase in $N_\|$, as can be seen from Figure 9.

To determine the fast-wave cutoff properly, all three components of the wave-vector, N_x, N_y, and N_z, must be explicitly included. This is necessary for the following reason. For the accessibility calculation, the region of interest is near the mode-conversion layer, in the interior of the plasma. Therefore we may use the WKB approximation and assume the scale lengths for density and field gradients are small compared to a wavelength so we may treat the plasma as locally homogeneous. This enables us to rotate the coordinate system so that $\mathbf{k}$ and $\mathbf{B}_0$ are always in the x-z plane and the problem is reduced to two dimensions so $\mathbf{k} = k_\perp \hat{\mathbf{x}} + k_\| \hat{\mathbf{z}}$. For the coupling problem, however, the plasma boundary is an inherent inhomogeneity. The direction of $\mathbf{B}_0$ and the normal to the plasma surface are innate to the problem. The wave-vector can have components in each of these directions and perpendicular to both. Hence, three components are required.

The wave equation becomes

$$\begin{pmatrix} K_{xx} - N_z^2 - N_y^2 & K_{xy} + N_y N_x & N_z N_x \\ K_{yx} + N_x N_y & K_{yy} - N_x^2 - N_z^2 & N_z N_y \\ N_x N_z & N_y N_z & K_{zz} - N_x^2 - N_y^2 \end{pmatrix} \begin{pmatrix} E_x \\ E_y \\ E_z \end{pmatrix} = 0. \tag{16}$$

The dispersion relation is obtained as before by setting the determinant of this system of equations to zero. The cold plasma approximation yields $K_{zx} = K_{zy} = K_{xz} = K_{yz} = 0$, $K_{yy} = K_{xx}$, and $K_{xy} = -K_{yx}$. The lower-hybrid approximating condition gives simplified dielectric tensor elements as before, and the fast- and
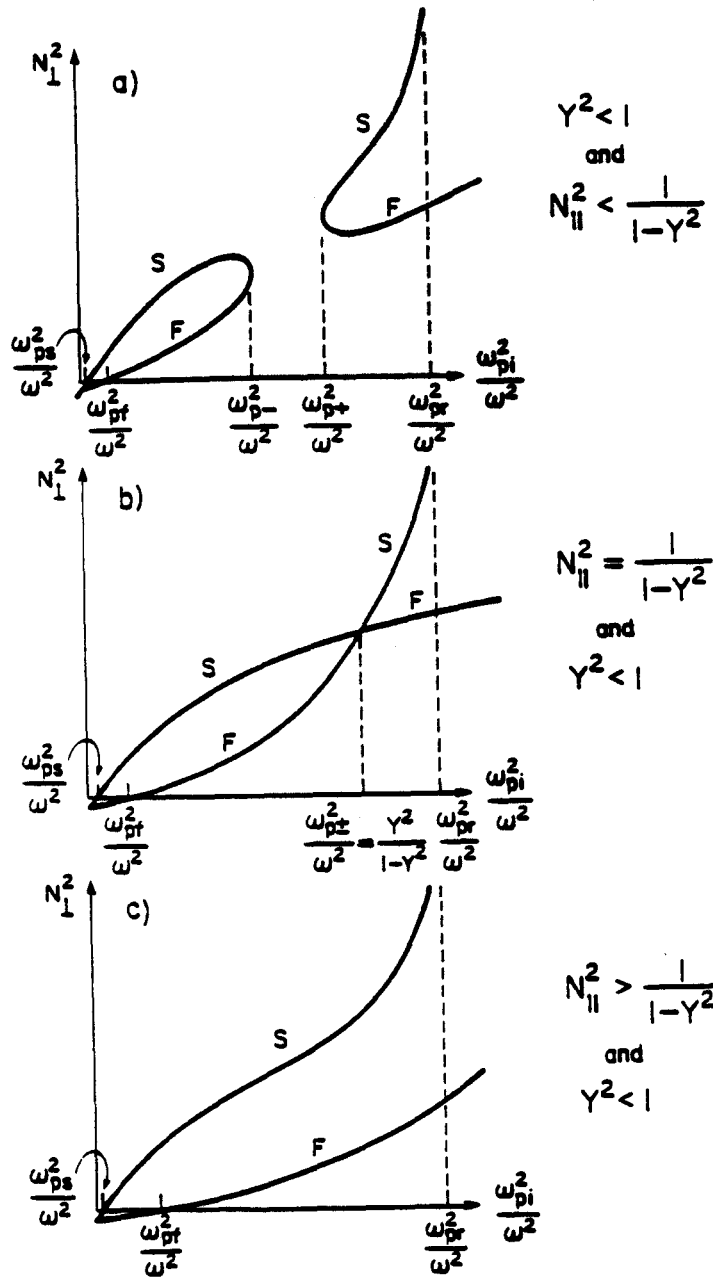
Figure 5: Plot of $N_\perp^2$ versus density (ω_{pi}^2/ω^2), showing the slow and fast roots of the lower-hybrid dispersion relation. The slow- and fast-wave cutoffs are ω_{ps}^2/ω^2 and ω_{pf}^2/ω^2. The lower-hybrid resonance is at ω_{pr}^2/ω^2 and the points where the slow and fast waves meet are ω_{p-}^2/ω^2 and ω_{p+}^2/ω^2 (from reference [10]).

slow-wave cutoff conditions can quickly be obtained from the resulting equation. For cutoff, $N_x \rightarrow 0$, and we obtain the following:

$$K_{zz}(K_{xx} - N_z^2 - N_y^2)(K_{xx} - N_z^2) + K_{zz}K_{xy}^2 = 0. \tag{17}$$

This equation has two solutions. The slow-wave cutoff density is given by $K_{zz} = 0$, so that the slow-wave is evanescent at electron densities below $n_{cutoff}^s = \omega^2 m_e \epsilon_0 / e^2$. The fast-wave cutoff is given by

$$(K_{xx} - N_z^2 - N_y^2)(K_{xx} - N_z^2) + K_{xy}^2 = 0, \tag{18}$$

giving an approximate cutoff density of

$$n_{cutoff}^f = (m_e \epsilon_0 / e^2) \omega \omega_{ce} \sqrt{(1 - N_z^2 - N_y^2)(1 - N_z^2)}. \tag{19}$$

For typical Versator-II parameters of $\omega_{ce}/2\pi = 28$ GHz, $\omega/2\pi = 2.45$ GHz, $N_z^2 = 4$, $N_y^2 = 0$, this gives $n_{cutoff}^f \approx 34 n_{cutoff}^s$, making the fast-wave more difficult to launch with an external antenna.

17

1.3 Simple Picture of Current-Drive Efficiency

The current-drive efficiency, J/P_d, is the toroidal current density divided by the wave power dissipated per unit volume. An approximate expression for it can be obtained by balancing the rf power required to diffuse electrons outward in velocity-space with the power lost due to collisions with the bulk plasma.[11]

Consider the resonant interaction of waves with phase velocity $v_p \gg v_{te}$ and electrons with velocity v_p parallel to the confining magnetic field, where $v_{te} = \sqrt{2T_e/m_e}$ is the electron thermal speed. The current density generated from pushing the electrons in velocity-space with the rf is given by

$$J = n_r e v_p \tag{20}$$

where n_r is the density of the resonant electrons. These electrons are slowed by Coulomb collisions with the bulk plasma, which exerts a drag force given by the following:

$$F_d = n_r m_e v_p^{-2} \left(\frac{\omega_{pe}^4 \log \Lambda}{4\pi n} \right) \tag{21}$$

where $\log \Lambda$ is the Coulomb logarithm, n is the bulk density, and $\omega_{pe} = \sqrt{n_e e^2/m_e \epsilon_0}$ is the electron plasma frequency. Note that F_d is proportional to v_p^{-2}. For steady-state current-drive, the rf power density is equal to the power lost to the bulk via drag:

$$P_d = F_d \cdot v_p = \frac{n_r}{v_p} \left(\frac{\omega_{pe}^4 m_e \log \Lambda}{4\pi n} \right). \tag{22}$$

The current-drive efficiency is the driven current divided by the dissipated power density:

$$\frac{J}{P_d} = v_p^2 \left(\frac{4\pi n e}{\omega_{pe}^4 m_e \log \Lambda} \right).$$ (23)

Volume averaging yields the following figure of merit for steady-state current-drive in a tokamak:

$$\tilde{\eta} = \frac{\bar{n}(10^{20} \mathrm{m}^{-3})I(\mathrm{kA})R(\mathrm{m})}{P_{rf}(\mathrm{kW})} = v_p^2 \cdot \mathrm{constant}$$ (24)

where $\bar{n}$ is the line-averaged electron density, I is the driven toroidal plasma current, and R is the major radius.

The figure of merit is proportional to v_p^2, which shows higher phase-velocity waves drive current more efficiently. This is because they resonate with faster, less collisional electrons.

1.4 Fisch-Karney-Boozer Theory of Current Drive

To gain a more realistic qualitative picture of how current-drive works, and to obtain accurate quantitative predictions of current-drive efficiency, kinetic theory must be used. The interaction of the waves and the electron distribution function must be examined, taking into account two-dimensional effects.

Following the analysis of Fisch and Boozer,[12] the current-drive efficiency J/P_d may be calculated using an "impulse response" method, where J is the driven current density and P_d is the power dissipated per unit volume.

19

Consider the displacement in velocity space of a small number of electrons δf from velocity $\mathbf{v}_1$ to $\mathbf{v}_2$. The energy required for this displacement is

$$\Delta E = (E_2 - E_1)\delta f, \tag{25}$$

where $E_1 = \frac{1}{2}m_e v_1^2$ and $E_2 = \frac{1}{2}m_e v_2^2$. Recall from the previous section that the collisional drag on an electron is dependent on its velocity. Assigning a velocity decay rate $\nu_i(v)$ to each velocity v_i gives the following transient current:

$$\mathcal{J}(t) = -e\delta f \left[v_{\|2} e^{-\nu_2 t} - v_{\|1} e^{-\nu_1 t} \right], \tag{26}$$

where the $\|$ subscript indicates the component of v_i parallel to the confining magnetic field. The first term on the right results from the new electron at velocity v_2, and the second term results from the missing electron at v_1. These currents decay at different rates ν_1 and ν_2, which depend only on v_1 and v_2.[12]

The average of $\mathcal{J}(t)$ over a time Δt that is large compared to $1/\nu_1$ and $1/\nu_2$ is defined as J:

$$J \equiv \frac{1}{\Delta t} \int_0^{\Delta t} \mathcal{J}(t) dt = \frac{e\delta f}{\Delta t} \left(\frac{v_{\|1}}{\nu_1} - \frac{v_{\|2}}{\nu_2} \right), \tag{27}$$

where J can be interpreted as the current generated in a time Δt by an amount of energy ΔE. Substituting from Equation 25 for δf and identifying $\Delta E/\Delta t$ as P_d yields the following:

$$\frac{J}{P_d} = -e \left(\frac{v_{\|1}/\nu_1 - v_{\|2}/\nu_2}{E_1 - E_2} \right). \tag{28}$$

Taking the limit as $\mathbf{v}_2 \to \mathbf{v}_1$ yields[12]

$$\frac{J}{P_d} = \frac{-e\hat{\mathbf{s}} \cdot \nabla_v (v_{\|}/\nu)}{\hat{\mathbf{s}} \cdot \nabla_v E} \tag{29}$$

20

where $\hat{s}$ is the unit vector (in velocity space) in the direction of $\Delta \mathbf{v}$, ∇_v is the gradient operator in velocity space, and the subscripts have been dropped.

This equation shows that the current-drive efficiency depends on the velocity of the electrons absorbing the power, *and* on the direction in velocity space in which these electrons are accelerated. This can be seen by taking the limit $\mathbf{v}_1 \to \mathbf{v}_2$ of Equation 27:[13]

$$\mathbf{J} = -e\frac{\Delta \mathbf{v}}{\Delta t} \cdot \nabla_v \left(\frac{v_\parallel}{\nu(v)} \right) \tag{30}$$

where $\Delta \mathbf{v} = \mathbf{v}_2 - \mathbf{v}_1$ and $v = |\mathbf{v}|$. Differentiating,

$$\mathbf{J} = -e\frac{\Delta \mathbf{v}}{\Delta t} \cdot \left(\frac{\hat{z}}{\nu} + \frac{v_\parallel}{\nu^2} \nabla_v \nu \right). \tag{31}$$

The first term represents the contribution to the current via direct parallel momentum transfer from the rf to the electrons and is proportional to the z-component of $\Delta \mathbf{v}$. The second term, present even if no parallel momentum is imparted to the electrons, is due to the velocity dependence of the collision frequency. If electrons traveling in one toroidal direction are preferentially heated, even if this heating is purely perpendicular, they will become less collisional, resulting in an asymmetric resistivity and a net toroidal current.

Now $\Delta \mathbf{v}$ is related to the characteristics of the rf wave that produces it. Energy and momentum are absorbed by the electron when it is in "resonance" with the wave, that is, when the Doppler-shifted wave frequency (as seen by the electron streaming parallel to the confining magnetic field) is an integer multiple of the cyclotron frequency:

$$\omega - k_\parallel v_\parallel = n\omega_{ce} \tag{32}$$

where $n = 0, \pm 1, \pm 2, \ldots$. The parallel velocity at which an electron will strongly absorb energy from the wave is then

$$v_{\parallel} = \frac{\omega - n\omega_{ce}}{k_{\parallel}}.$$ (33)

For waves in the lower-hybrid range of frequencies (LHRF), such as those radiated by the present antenna, $\omega \ll \omega_{ce}$ and resonance occurs for $n = 0$, yielding $v_{\parallel} = \omega/k_{\parallel} = v_{phase}$. Because we want electrons with a particular sign of $v_{\parallel}$ to be preferentially heated, this shows that in the LHRF, we must launch rf waves with a phase velocity in a particular parallel direction.

The basic idea of current drive through parallel momentum transfer can best be understood by considering the original paper on the subject by Fisch.[3] The one-dimensional treatment presented there shows how the first term in Equation 31 contributes to the current-drive efficiency of a broad spectrum of waves interacting with a distribution of electrons.

In the parallel direction, the rf diffuses electrons outward in velocity space, competing with the collisional relaxation of the plasma, which attempts to restore itself to a Maxwellian. The effect of the rf is encapsulated into a quasilinear diffusion coefficient, D_{QL}, which enters the one-dimensional Fokker-Planck equation as follows:

$$\frac{\partial f}{\partial t} = \left[\frac{\partial}{\partial v_{\parallel}} D_{QL}(v_{\parallel}) \right] \frac{\partial f}{\partial v_{\parallel}} + \left. \frac{\partial f}{\partial t} \right|_{c}$$ (34)

where $\left. \frac{\partial f}{\partial t} \right|_{c}$ is the Fokker-Planck collision operator, which includes Coulomb scattering in both the parallel and perpendicular directions. Integrating Equation 34

22

over the perpendicular direction, assuming f is Maxwellian in this direction, yields the following equation for high velocity electrons:

$$\frac{\partial f}{\partial \tau} = \frac{\partial D(w)}{\partial w}\frac{\partial f}{\partial w} + \frac{\partial}{\partial w}\left(\frac{1}{w^3}\frac{\partial f}{\partial w} + \frac{f}{w^2}\right) \tag{35}$$

where $w = v_{\parallel}/v_{th}$, $\tau = \nu_0 t$, $\nu_0 = \nu' w^3$, $\nu' = \omega_{pe}^4 \ln\Lambda/2\pi n_e v_{\parallel}^3$, and $D(w) = D_{QL}/\nu_0 v_{th}^2$.

With strong rf, $D(w)$ is very large for $w_1 < w < w_2$ and zero otherwise, and the steady-state solution to Equation 35 is approximately flat for $w_1 < w < w_2$ and roughly Maxwellian outside this region (see Figure 6).

The height of the plateau is found by evaluating the bulk Maxwellian at $w = w_1$:

$$f(w)\Big|_{w_1 < w < w_2} \approx f(w_1) = \frac{e^{-w_1^2}}{\sqrt{\pi}}. \tag{36}$$

The current carried by the resonant electrons with $w_1 < w < w_2$ is given by

$$J = \int_{w_1}^{w_2} n_e e w v_{th} f(w_1)\, dw$$
$$= n_e e v_{th}\frac{e^{-w_1^2}}{\sqrt{\pi}}\left(\frac{w_2^2 - w_1^2}{2}\right). \tag{37}$$

In the steady-state, the power absorbed by the resonant electrons from the rf is equal to the power absorbed by the bulk from the resonant electrons via Coulomb collisions. This dissipated power is given by the following:

$$P_d = \int_{w_1}^{w_2} n_e m_e v_{th}^2 \nu_s w^2 f(w_1)\, dw \tag{38}$$

23
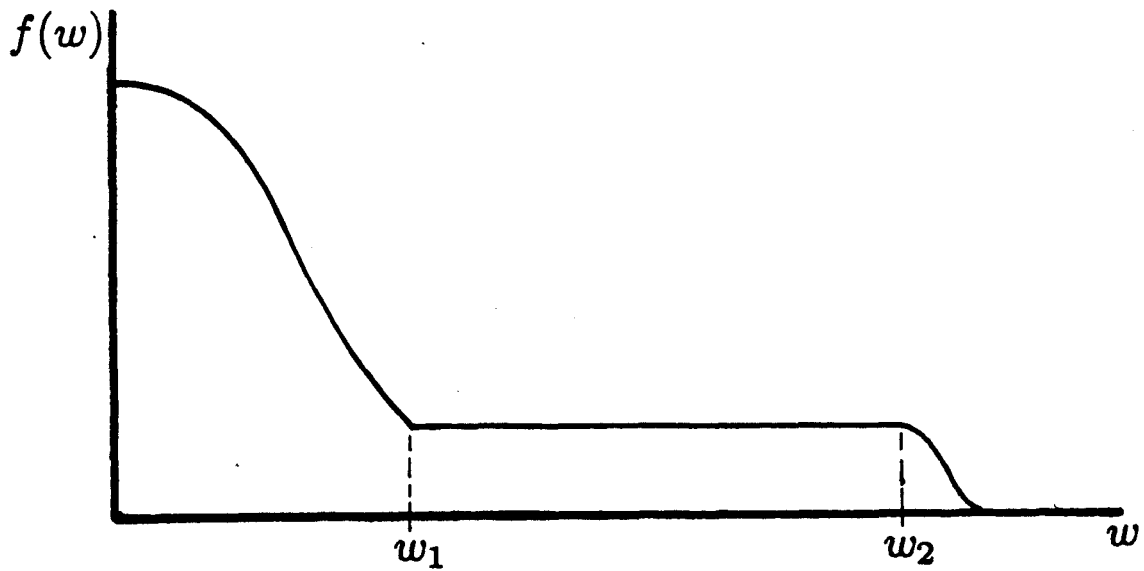
Figure 6: Distribution function for electrons in the presence of strong rf.
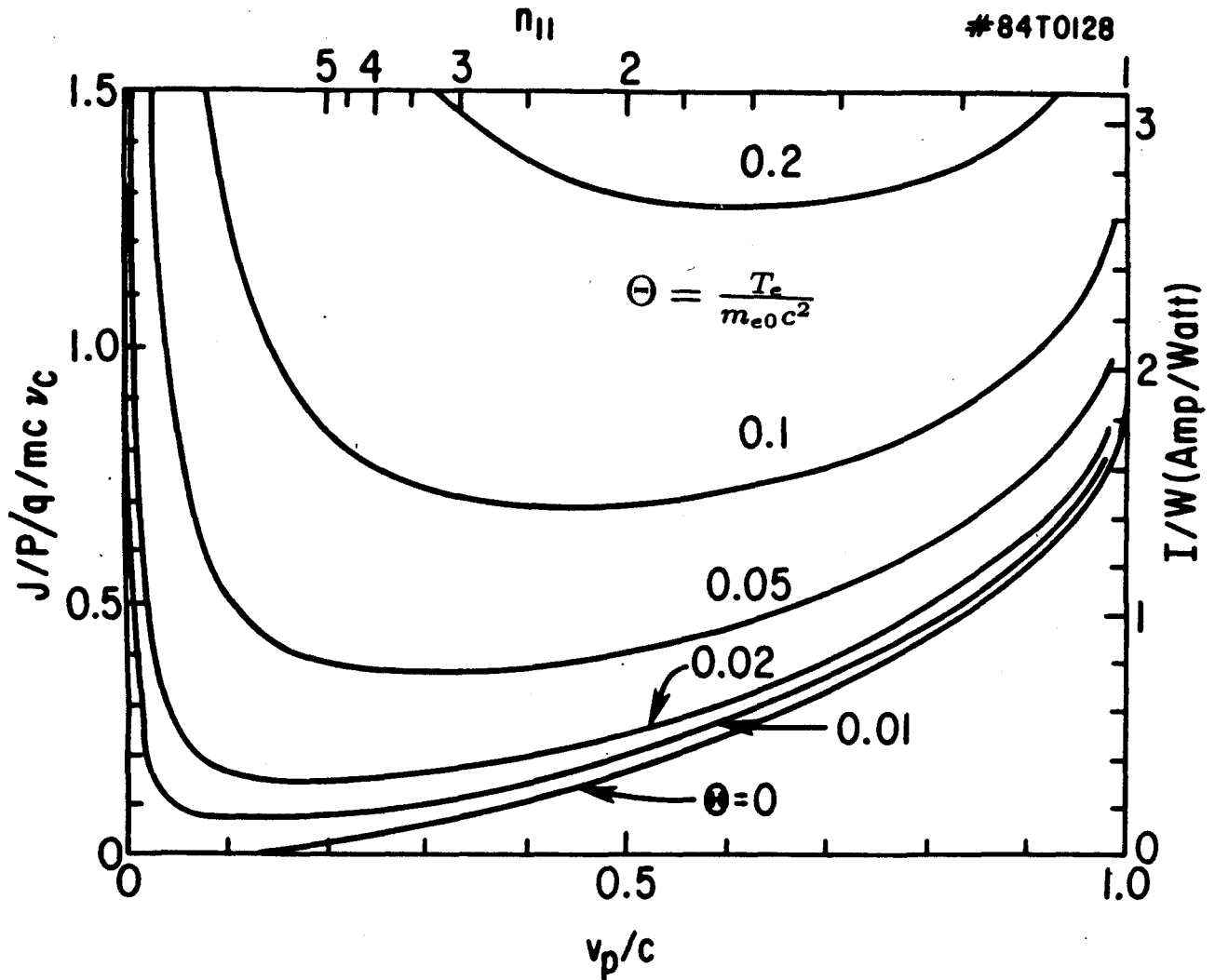
Figure 7: Plot of relativistic current-drive efficiency (from reference [14]).

where $\nu_s = \nu'(v_{th}^3/v_{\parallel}^2)(2 + Z_i)$ in the limit $v_{\parallel}/v_{th} \gg 1$, which is a good approximation for the high velocity resonant electrons,[3] and Z_i is the charge state of the background ions. Evaluating the above integral yields

$$P_d = n_e m_e v_{th}^2 \nu' \; \frac{e^{-w_1^2}}{\sqrt{\pi}} \; (2 + Z_i) \; \ln(w_2/w_1). \tag{39}$$

The total driven current over the total input power is given by

$$\frac{I}{P} \;=\; \frac{\langle J \rangle}{2\pi R \langle P_d \rangle} \tag{40}$$

where $\langle \; \rangle$ indicates an average over the plasma cross-section, and toroidal symmetry is assumed. The current-drive figure of merit $\tilde{\eta}$ is obtained by combining Equations 37, 39 and 40, giving

$$\begin{aligned}
\tilde{\eta} \;&=\; \frac{\overline{n}_e(10^{20}\mathrm{m}^{-3}) I(\mathrm{kA}) R(\mathrm{m})}{P(\mathrm{kW})} \\
&\approx 0.0054\, T(\mathrm{keV}) \left(\frac{w_2^2 - w_1^2}{2} \right) \frac{1}{(2 + Z_i)\ln(w_2/w_1)}.
\end{aligned} \tag{41}$$

Note that $\tilde{\eta}$ is proportional to velocity squared, as given in the simple picture of section 1.3.

Expressed in terms of the $N_{\parallel}$ of the rf wave spectrum, the figure of merit is

$$\tilde{\eta} \;\cong\; \frac{1.4}{2 + Z_i} \; \frac{1/N_{\parallel 2}^2 - 1/N_{\parallel 1}^2}{2\ln(N_{\parallel 1}/N_{\parallel 2})} \tag{42}$$

where $N_{\parallel 2} < N_{\parallel} < N_{\parallel 1}$. This shows that waves with high parallel phase velocity (low $N_{\parallel}$) drive current more efficiently.

Recall that an asymmetric resistivity is produced by the perpendicular-velocity-space structure of the interaction of the rf with the plasma. This makes current drive by cyclotron damping possible. However, this effect is not important for current drive by lower-hybrid waves, which diffuse particles only in the $v_\parallel$-direction.

An additional effect neglected in Equation 35 is the two-dimensional structure of the collision operator. When this structure is retained, the calculated current-drive efficiency is improved by a factor of two.[12] This is because when electrons are pitch-angle scattered out of the resonance region by the bulk, resulting in a loss of parallel momentum, they gain (on the average) perpendicular energy. This decreases their collisionality relative to what one would expect if the increase in perpendicular energy were ignored. Because these electrons are on the average traveling in the same direction as before they were scattered, the calculated current-drive efficiency is higher than one would expect taking into account only the parallel dynamics.

A fully relativistic calculation of the current-drive efficiency of low-$N_\parallel$ lower-hybrid waves is given by Karney and Fisch.[14] They find that two relativistic effects set an upper limit on the efficiency. First, the relativistic electrons slow down faster because they are heavier. Second, the current carried by the electrons is proportional to their velocity, which approaches a constant (equal to the speed of light) as momentum is imparted to them and they become heavier. Each of these effects reduces the efficiency by a factor of γ, so combined they reduce $\bar{\eta}$ by a factor of $\gamma^2 \sim p^2$, where p is momentum, cancelling the nonrelativistic v^2 dependence and forcing $\bar{\eta}$ to approach a constant at high velocities. This dependence is shown in Figure 7.[14]

1.5 The History of Lower-Hybrid Current Drive Experimentation

Soon after Fisch's paper[3] was published, slow-wave current-drive results were reported on the JFT-2 tokamak in Japan[15] and the Versator-II tokamak at MIT.[16]

26

The slow wave was used in these experiments because it is easy to launch, and because it has a higher Landau damping rate, making it more effective in driving current in the relatively small, cold, tenuous plasmas of these tokamaks. The current was sustained mostly by the Ohmic Heating (OH) transformer and current drive of ~ 15 kA was inferred by comparing the currents and loop voltages of plasma shots with and without rf. On Versator, the increased current was not due to a reduction in plasma resistivity caused by the rf, because the electron temperature (as measured by Thomson scattering) went down during the rf pulse, thereby increasing the resistance.[16] Also, the current-drive efficiency went abruptly to zero above a certain critical density, called the "density limit." This was unexpected because Fisch's theory predicts the efficiency to scale as $\bar{n}_e^{-1}$. On the Versator 800 MHz experiment, this density limit was about $6 \times 10^{12} \text{cm}^{-3}$, for which the lower-hybrid frequency $\omega_{LH}/2\pi$ is about 400 MHz.

Current was "flattopped" for the first time on the PLT tokamak at Princeton,[17] where a fully rf-driven current of 165 kA was maintained for 3.5 s with the loop voltage near zero. The OH transformer primary current was clamped after plasma start-up, and the subsequent L/R decay of the plasma current was fully arrested by the rf, so that a steady-state current was maintained (see Figure 8). A flattopping current-drive efficiency $\bar{\eta} = \bar{n}IR/P_{rf} \approx 0.1$ was attained, in reasonably good agreement with Fisch's theory.[3] A density limit was observed on this experiment of $8 \times 10^{12} \text{cm}^{-3}$, for which $\omega_{LH}/2\pi \approx 600$ MHz.

Current was first driven at high densities ($\sim 10^{14} \text{cm}^{-3}$) on the Alcator tokamak at MIT. Up to 200 kA was maintained by 1.1 MW of 4.6 GHz slow waves launched by a 4×4 phased array of waveguides. Efficiency was measured over a wide density range and found to agree well with the Fisch[3] theory; $\bar{\eta} \approx 0.12$ was attained with $\mathbf{B}_0 = 10$ T and $\bar{\eta} \approx 0.08$ for $\mathbf{B}_0 = 8$ T.[18] Since these results were obtained, current has been driven by slow waves on other tokamaks throughout the world.

Mayberry, et. al. ,[19] showed that the density limit is a function of the source frequency by driving current on Versator-II with a 2.45 GHz source at densities
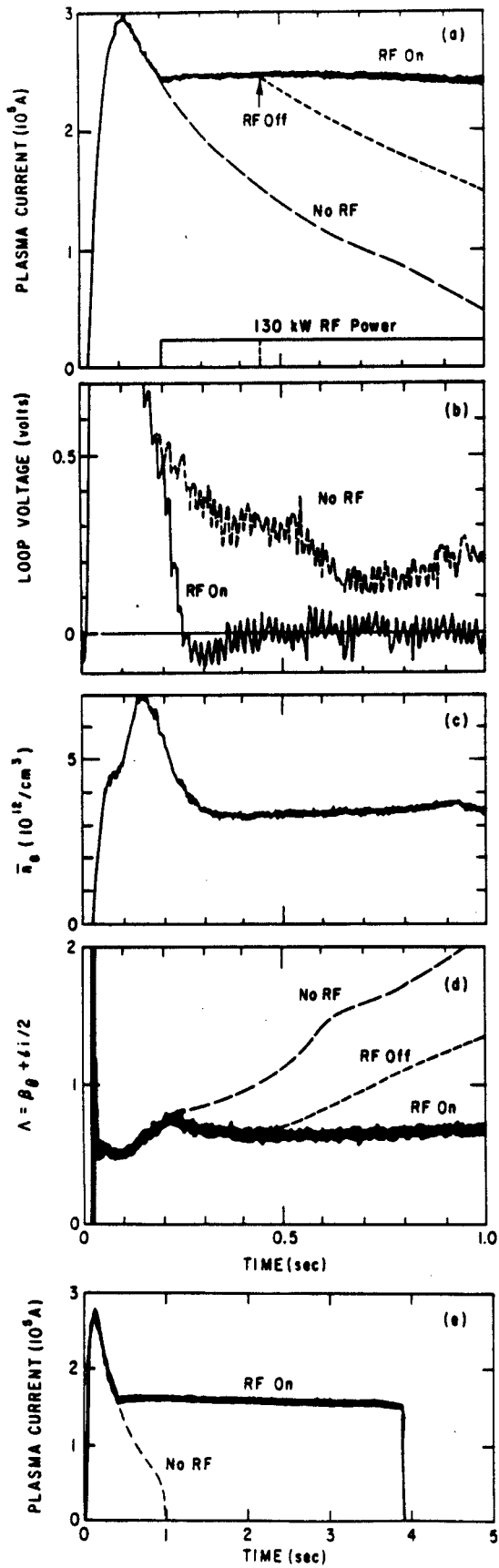
Figure 8:

(a)-(d) Characteristics of deuterium discharges in
the PLT tokamak with and without 130 kW of rf,
$B_0 = 3.1$ T. (e) A long-pulse discharge with 70 kW of rf,
$B_0 = 2.3$ T (from reference [17]).

28

above $1 \times 10^{13} \text{cm}^{-3}$ with the same toroidal magnetic field as for the 800 MHz experiments. A flattopping current-drive efficiency $\tilde{\eta} = 0.0072$ was attained. This efficiency is considerably lower than that of the PLT and Alcator experiments. This could be due to poorer confinement of the fast current-carrying electrons, poorer accessibility of low-$N_{\|}$ waves, or the larger "spectral gap." The first two are caused by the lower toroidal magnetic field on Versator, and the third by the lower electron temperature.

Little experimental data has been obtained on fast-wave current-drive. Experiments have been performed on PLT at 800 MHz,[20] JIPPT-IIU at 40 MHz[21] and 800MHz,[22] JFT2-M at 200 MHz,[23] and ACT-I at 18 MHz.[24] In the 800 MHz experiments, both fast and slow waves could propagate in the plasma. Antenna coupling characteristics indicated that the fast wave was being launched, but the current-drive efficiency and "density limit" were identical to those of the slow wave. Although some authors[22] claim to have driven current with the fast wave, it is probable that in both the 800 MHz experiments, fast waves were lauched, but much of the power in the waves was subsequently mode-converted to the slow wave via a toroidal $N_{\|}$-shift, and the slow wave (which interacts with electrons much more strongly) was driving most of the current.

1.6 Motivation for Fast-Wave Current-Drive

The primary motivation for studying the fast-wave is that it is more capable than the slow wave of penetrating to the core of a hot, dense, reactor-grade plasma and driving current efficiently there. This is because low $N_{\|}$ waves, which drive current most efficiently, are only accessible to the plasma center in the fast mode.

This can be seen in the following way.[25] Recall from section 1.2 the accessibility condition for waves in the LHRF:

$$N_{\parallel}^2 > \left[\frac{\omega_{pi}}{\omega_0} + \sqrt{1 + \frac{\omega_{pi}^2}{\omega_0^2}\left(1 - \frac{\omega_0^2}{\omega^2}\right)} \right]^2 , \qquad (43)$$

where $\omega_0 = \sqrt{\omega_{ce}\omega_{ci}}$ is the mean gyrofrequency and ω is the source frequency. Waves can propagate anywhere in the plasma where this inequality is satisfied. Figure 9a is a plot of $|N_{\parallel min}|$ as a function of ω_{pi}/ω_0 for various values of ω/ω_0, where $N_{\parallel min}$ is obtained by making the above inequality an equality. Propagation can occur above a given curve for the corresponding ω/ω_0, as shown in Figure 9b. I refer to these curves as "frequency curves."

Note that the quantity under the radical in Equation 43 is negative below the slope $= 1$ line on the graph. This line corresponds to the lower-hybrid resonance layer, which the slow wave cannot penetrate. Therefore, only the fast wave has a solution below this line, and for a given frequency, the slow wave has no solution anywhere to the right of the intersection of the corresponding frequency curve and this line. This is illustrated in Figure 9b. Note that frequency curves with $\omega/\omega_0 > 1$ never approach the lower-hybrid layer at any density; it does not exist in this case. At high density these curves approach asymptotes with slope $1 + \sqrt{1 - \omega_0^2/\omega^2}$.

Now examine the following problem: for a tokamak plasma with a given magnetic field and density on axis, what is the lowest $N_{\parallel}$ wave that can propagate everywhere in the plasma, and hence can reach the center from the edge?

Assuming the magnetic field gradient is less than the gradient of the square root of the density, monotonic motion from the plasma edge to its center corresponds to monotonic motion to the right on the plot. Fixing the plasma density and magnetic field on axis fixes a vertical line that represents the plasma center on the graph. This is shown on Figure 9a as the heavy dashed line. The edge of the plasma corresponds
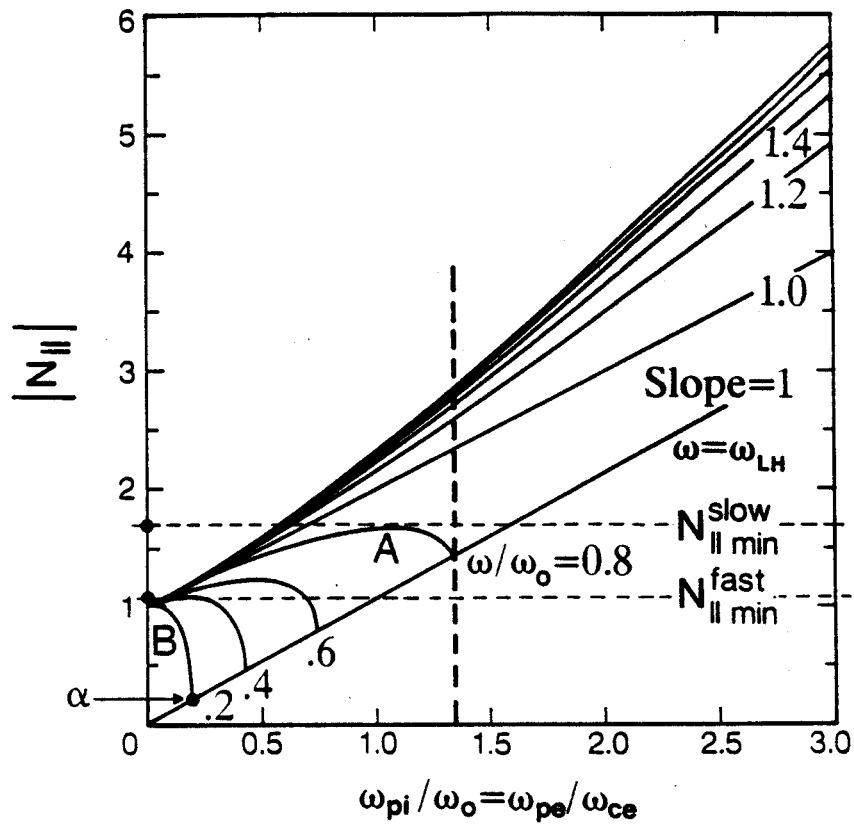
Figure 9a: Plot of accessibility condition. Waves can propagate for $N_{\parallel}$ above the curve corresponding to the source frequency.
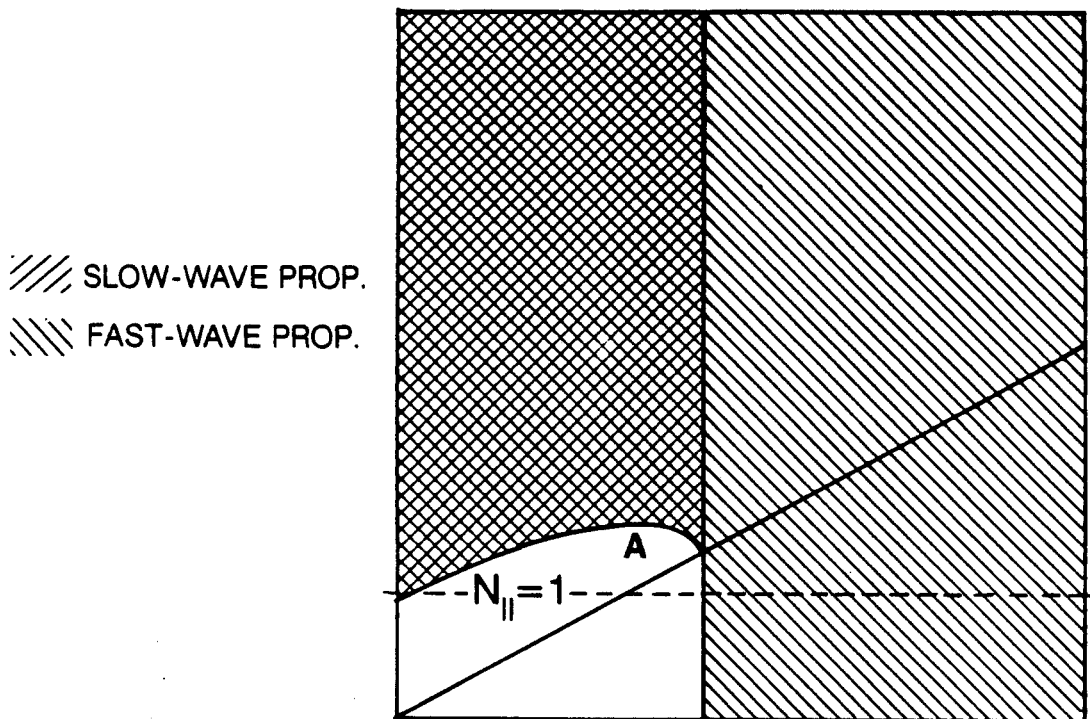

Figure 9b: Plot showing regions of propagation for the fast and slow waves.

31

to the vertical axis on the far left of the graph, the region between these two lines corresponds to the plasma, and the region to the right of the dashed line is now irrelevant and should be ignored.

Because propagation can only occur in the region above a given curve and we want the minimum $N_\parallel$ that can propagate everywhere in the plasma, it is best to lower the frequency as much as possible to reduce ω/ω_0, shifting to lower curves on the diagram. If the slow wave is launched in a plasma corresponding to the vertical line in the figure, the lowest acceptable is curve A, because for lower curves the lower-hybrid resonance layer prevents the wave from penetrating to the right of the point of intersection of the curve and the resonance line. Having chosen the best frequency curve, we note the lowest $N_\parallel$, labeled $N_{\parallel min}^{slow}$, that will propagate everywhere in the plasma. Maximizing Equation 43 with respect to ω_{pi}/ω_0 gives $N_{\parallel min} = \sqrt{1 - \omega^2/\omega_0^2}^{-1}$ for the peak of each curve. Setting $\omega = \omega_{LH_a}$ in this equation gives $N_{\parallel min}^{slow} = 1 + \omega_{pe_a}^2/\omega_{ce_a}^2$, where the subscript a denotes quantities on axis.[26] This is the condition for slow-wave accessibility all the way to the lower-hybrid resonance layer.

Because the fast wave can, in theory, propagate through the lower-hybrid resonance, it can propagate to the right of the intersection of the chosen frequency curve and the resonance line. This implies an arbitrarily low frequency may be chosen in principle. Taking the frequency curve B as an example, we can launch a fast wave with $|N_\parallel| = N_{\parallel min}^{fast} \approx 1$, and because there are no accessibility restrictions on $|N_\parallel|$ below the resonance line, it will propagate to the plasma center. A similar slow wave, however, would be stopped by the lower-hybrid resonance near the plasma edge at point α.

A secondary reason for prefering the fast wave for reactors is as follows.[27] Because the fast wave has a small electric-field component parallel to the confining magnetic field $\mathbf{B}_0$, its Landau-damping rate is much smaller than that of the slow wave. In the small, relatively cold and tenuous plasmas of most present-day tokamaks, full absorption would require many passes through the plasma, with possibly

deleterious effects on the $N_\parallel$-spectrum due to reflections and toroidicity. However, this would not be the case in a reactor. The damping rate is proportional to $e^{-v_p^2/v_{th}^2}$ where $v_p = \omega/k_\parallel$; this implies that $v_p/v_{th} \geq 2.3$ (approximately)[27] to avoid strong Landau damping on the bulk. Therefore in a hot, dense, reactor-grade plasma, where v_p/v_{th} is substantially smaller for a wave with a given parallel phase velocity, the damping rate is much higher. This affects both the slow and fast waves, so in reactors slow waves will be completely damped near the plasma edge, and fast waves will be absorbed in the hot core on the first or second pass. Slow waves, therefore, will probably not drive large toroidal currents in reactors, but may be useful for edge current-profile control and shaping.

It is important to consider the effect on E_z and on the Landau damping rate of lowering ω. The power absorbed via Landau damping is proportional to $|E_z|^2$. This will determine the number of passes required for complete absorption of the wave by the current-carrying electrons. It can be estimated as follows.

The total power flux density S_x is given by

$$S_x \approx \frac{P_{ant}}{A_{ant}} \tag{44}$$

where P_{ant} is the power launched by the antenna, and A_{ant} is the antenna area. For the fast wave with $\omega^2 \ll \omega_{pi}^2$,[28]

$$|E_z|^2 \approx \frac{2S_x\omega^6 N_z^2}{\epsilon_0 c_A \omega_{pi}^4 \omega_{ce}^2} \qquad \propto \qquad \omega^6 \tag{45}$$

where $c_A = B_0/\sqrt{\mu_0 n m_i}$ is the Alfvén speed. For $N_y = 0$, the fast-wave dispersion relation is[29]

$$N_x^2 \approx \frac{K_{xy}^2}{N_z^2 - K_{xx}} - N_z^2 + K_{xx} \tag{46}$$

33

where $K_{xx} \approx -\omega_{pi}^2/\omega^2$ and $K_{xy} \approx \omega_{pe}^2/\omega\omega_{ce}$. This yields

$$k_x \approx \frac{\omega\omega_{pi}}{c\omega_{ci}}. \tag{47}$$

The Landau damping rate is given by[28]

$$k_{xi} = k_x \left(\frac{\omega^2}{\omega_{pi}\omega_0}\right)^2 N_z^2 \sqrt{\pi}\zeta^3 e^{-\zeta^2} \quad \propto \quad \omega^5 \tag{48}$$

where $\omega_0 = \sqrt{\omega_{ce}\omega_{ci}}$. So we see that the magnitude of E_z and the Landau damping rate decrease sharply as the source frequency is lowered much below the ion plasma frequency.

For $\omega > \omega_{pi}$, the dispersion relation becomes

$$k_x = \frac{\omega_{pe}^2}{c\omega_{ce}\sqrt{N_z^2 - 1 - \omega_{pe}^2/\omega_{ce}^2 + \omega_{pi}^2/\omega^2}}. \tag{49}$$

Here, the dependence on ω is weak. The electric field is given by[28]

$$|E_z|^2 \approx \frac{2S_x k_x \omega}{\epsilon_0 N_z^2 \omega_{ce}^2}, \tag{50}$$

which is roughly proportional to ω. The Landau damping rate is[28]

$$k_{xi} \approx k_x \left(\frac{\omega_{pe}}{\omega_{ce}N_z}\right)^2 \sqrt{\pi}\zeta^3 e^{-\zeta^2} \sim \text{constant}. \tag{51}$$

We see that E_z and the Landau damping rate are weakly dependent on the source frequency for $\omega > \omega_{pi}$. So for the fast wave, single-pass absorption via electron

34

Landau damping will not occur if the source frequency is too far below $\omega_{pi} \sim \omega_{LH}$. In this case, however, transit-time magnetic pumping (TTMP) may strongly damp the waves.

It is important to understand that if the fast wave suffers from the same experimentally observed "density limit" that the slow wave does, the above arguments for fast-wave current-drive will be irrelevant. This is because, for a given density and magnetic field (say, those of the vertical line on Figure 9a), as the frequency is lowered, the density limit is encountered well before the lower-hybrid layer appears in the plasma. In other words, those regions of the plot that can be accessed by the fast wave but not the slow wave may be regions where no current can be driven by either wave due to the density limit. If the fast wave cannot break the density limit (for a fixed source frequency), it is no better than the slow wave for current drive in tokamaks.

There is a theoretical basis for expecting the fast wave to have a higher density limit than the slow wave. The cause of the density limit is not known; it is not predicted by linear wave propagation and absorption theory. However, a likely candidate is the parametric decay instability.[30] In theory, higher powers or higher electron densities are necessary for the parametric decay instability to be excited by the fast wave than by the slow wave.[31] Thus the density limit should be higher for fast-wave current-drive than for slow-wave current-drive if it is caused by the parametric decay instability.

35

2 THE SLOTTED-WAVEGUIDE

2.1 Motivation

The principal reason for experimenting with the slotted-waveguide is to find out if it couples to the fast-wave and, if so, how well it drives current. Others have performed FWCD experiments using the waveguide grill and the loop array, as shown in Figures 10 and 11.[20] [22]

The slotted-waveguide is shown in Figures 12 and 13. It has several advantages over the grill and loop array. First, the antenna area can be much greater than the port area. This is because the open-ended grill comes straight into the port and terminates at the plasma, but the slotted waveguide comes into the port, bends ninety degrees, and travels toroidally around the plasma edge for a distance many times the port width, radiating from its entire length. This creates an $N_{\parallel}$ spectrum with much narrower peaks than those of the grill, enabling more wave power to fit into the "window" in $N_{\parallel}$-space between the cutoff and accessibility limits. Also, the longer source should interact with the plasma electrons in a more spatially distributed way, decreasing the local rf power density in the plasma and lessening the possibility of deleterious nonlinear effects. Second, a slotted waveguide can produce an acceptable $N_{\parallel}$-spectrum without dielectric. This lowers the cost of the antenna enormously and eliminates the plasma impurities that may be generated by plasma/dielectric interaction.
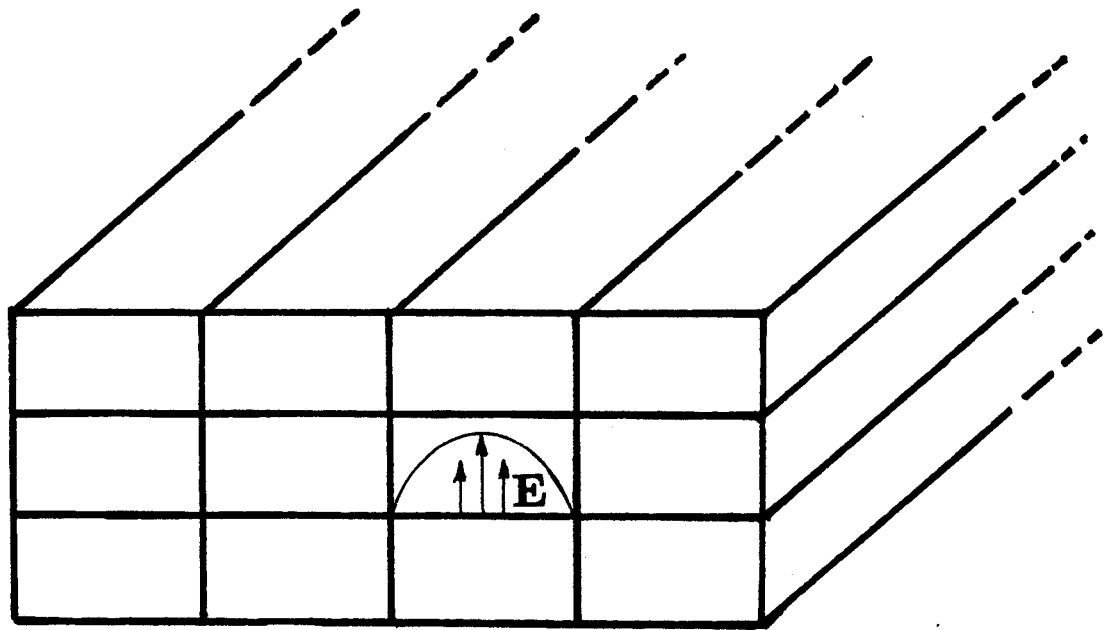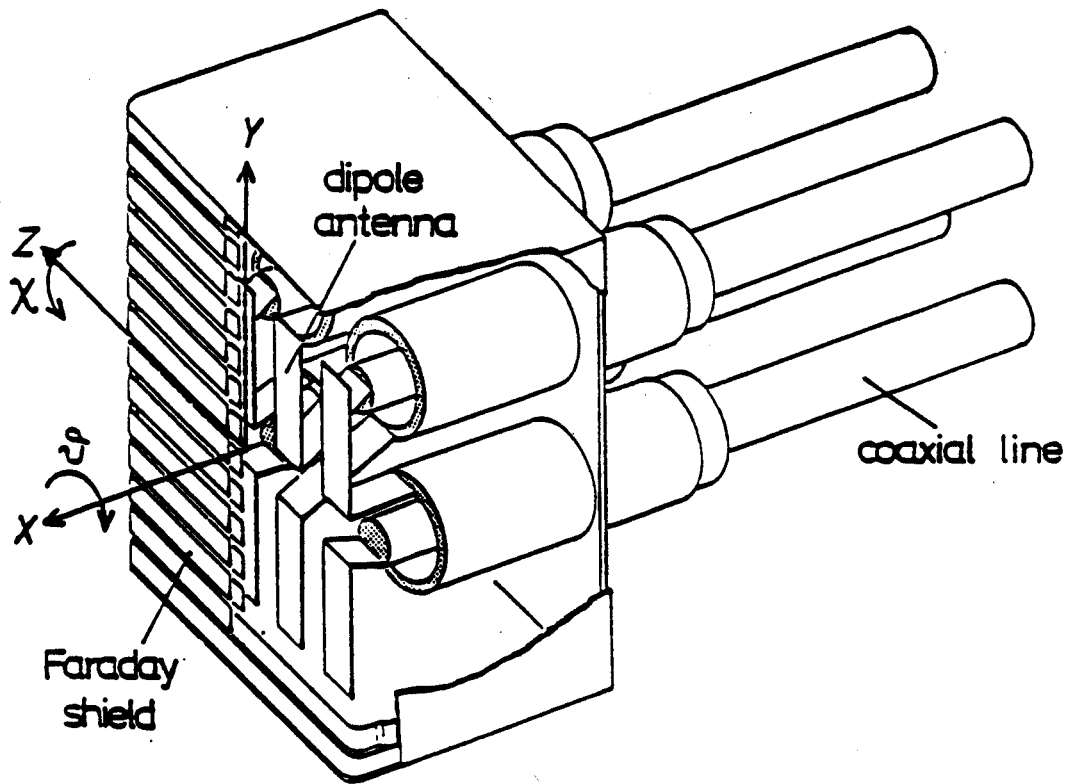
Figure 10: Waveguide grill, as used by Pinsker, et. al. [20].

Figure 11: Loop coupler (from reference [22]).
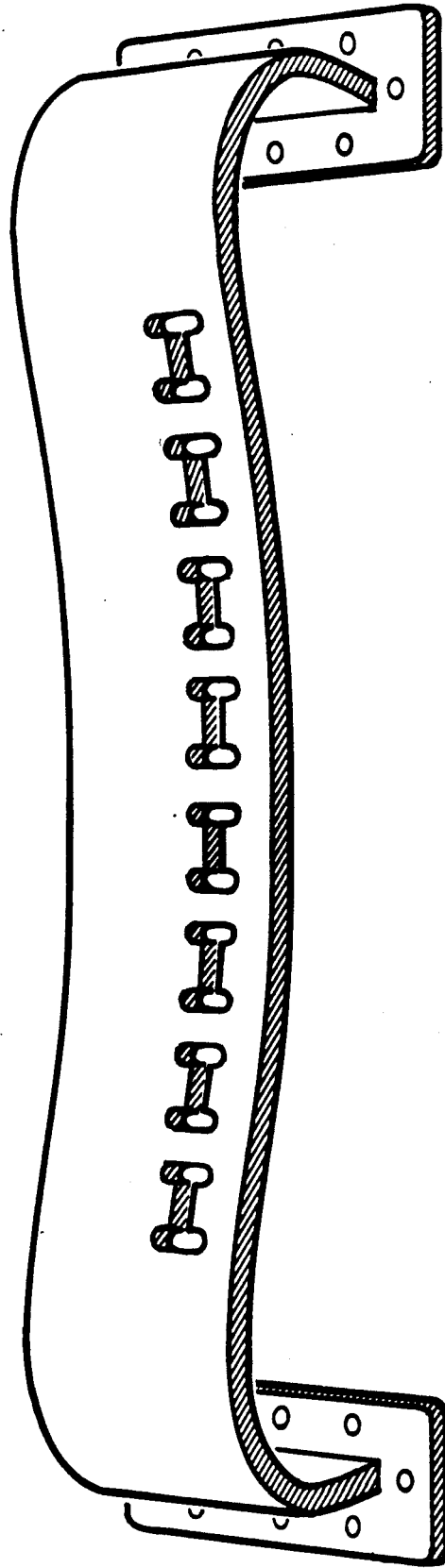
Figure 12: The slotted-waveguide coupler used in Versator-II.

to Directional Coupler and Matched Load

to Directional Coupler and Klystrons

Bellows

ANTENNA

H_α

I_p

B_o
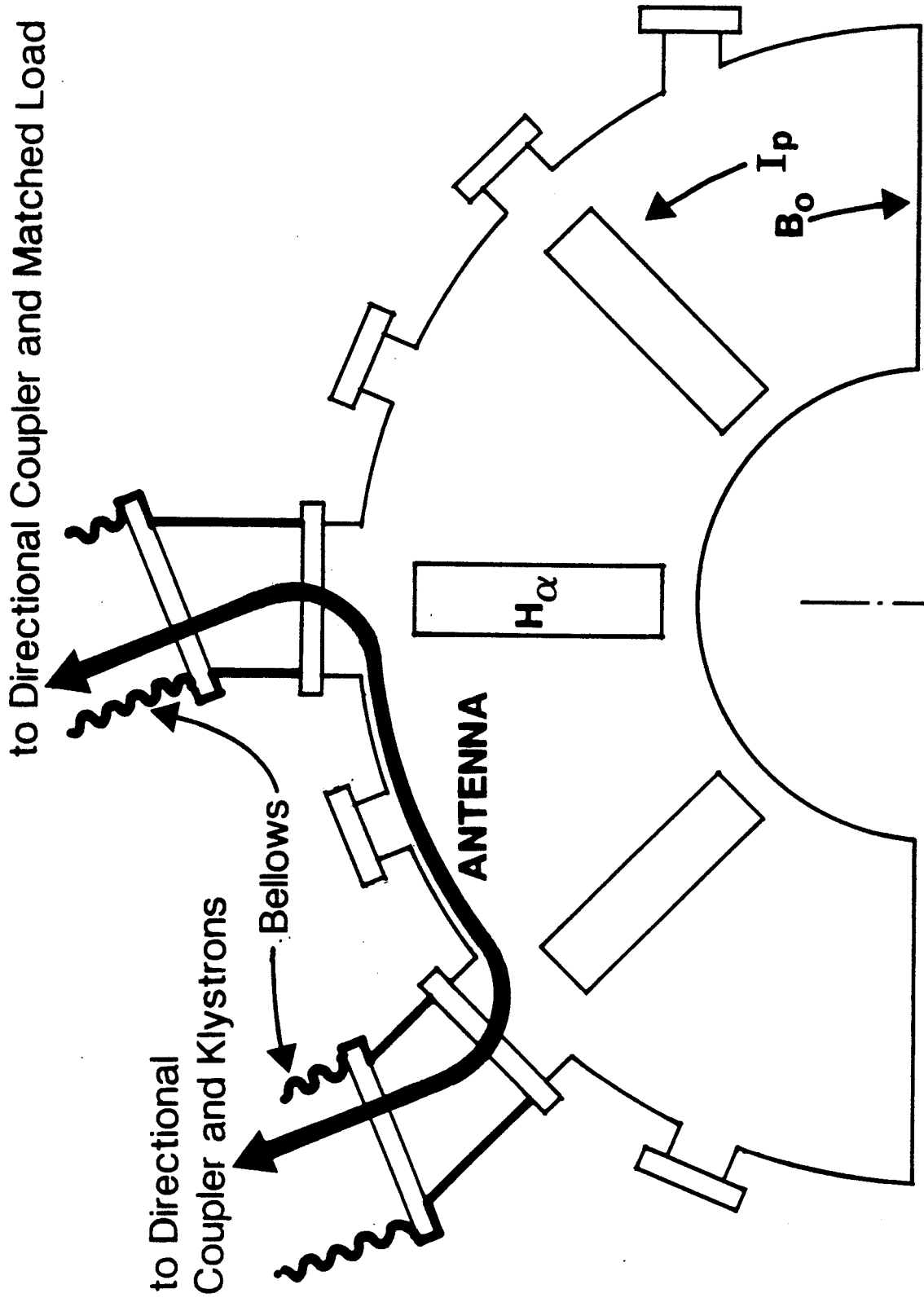
Figure 13: The antenna in Versator-II (shown for reverse spectrum).

2.2 Design Theory for Radiating into Free-Space

2.2.1 Single-Slot Conductance

To determine the free-space conductance of a slot in the broad face of rectangular waveguide that is parallel to the guide axis, we first assume a field distribution in the slot, then use orthogonality to compute the amplitudes of the normal modes excited in the guide by this source, and finally write a power balance equation to determine the relative amplitudes of the radiated and reflected powers, given a known incident power inside the waveguide.[32]

Consider a cylindrical waveguide of arbitrary cross-section as shown in Figure 14. The fields in such a guide can be written in terms of TE_{mn} and TM_{mn} modes, where TE (transverse electric) modes contain no E_z and TM (transverse magnetic) modes contain no H_z. The fields of these modes are

$$\mathbf{E}^t_{mn} = \mathbf{E}^t_{0mn} \exp(\mp j\beta_{mn}z) \tag{52}$$

$$\mathbf{H}^t_{mn} = \pm \mathbf{H}^t_{0mn} \exp(\mp j\beta_{mn}z) \tag{53}$$

$$\mathbf{H}^z_{mn} = j\mathbf{H}^z_{0mn} \exp(\mp j\beta_{mn}z) \tag{54}$$

for the TE_{mn} modes and

$$\mathbf{E}^t_{mn} = \mathbf{E}^t_{0mn} \exp(\mp j\beta_{mn}z) \tag{55}$$

40

Figure 14: Cylindrical waveguide of arbitrary cross-section with arbitrary slot.
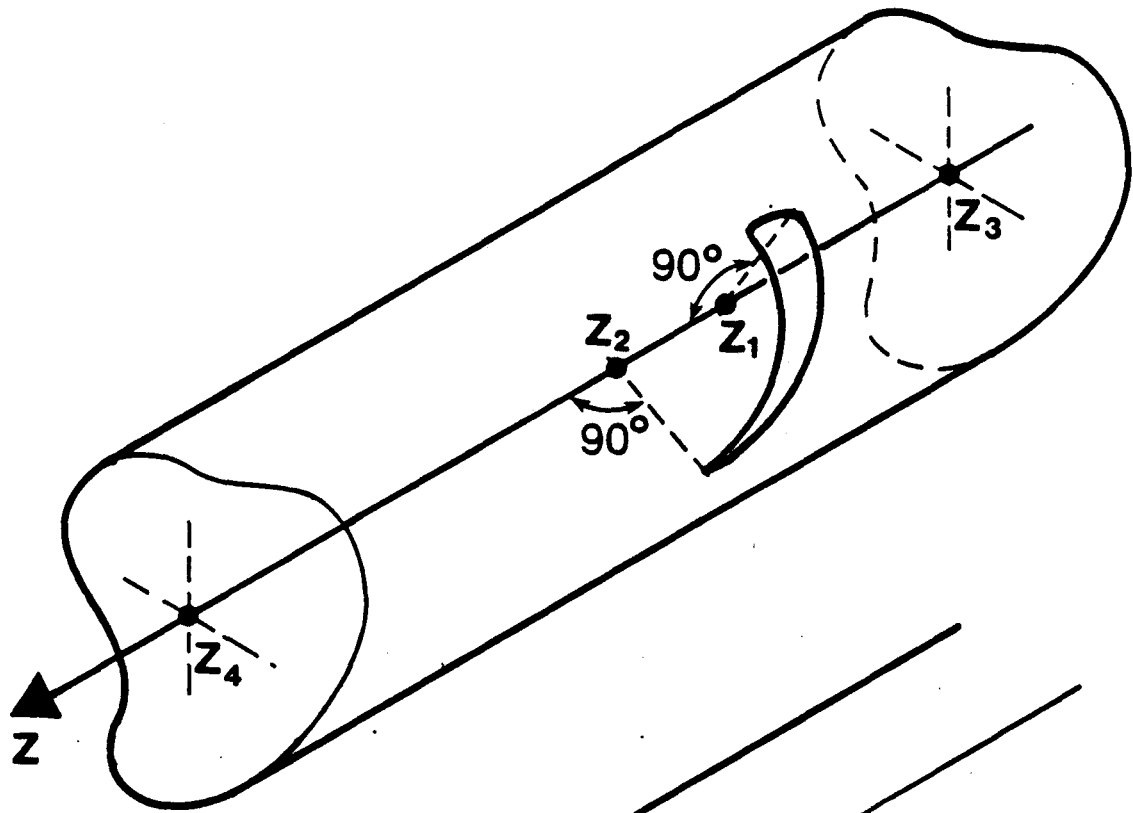
Figure 15: Rectangular waveguide with probe-fed slots.

$$\mathbf{H}_{mn}^{t} = \pm\mathbf{H}_{0mn}^{t}exp(\mp j\beta_{mn}z) \tag{56}$$

$$\mathbf{E}_{mn}^{z} = j\mathbf{E}_{0mn}^{z}exp(\mp j\beta_{mn}z) \tag{57}$$
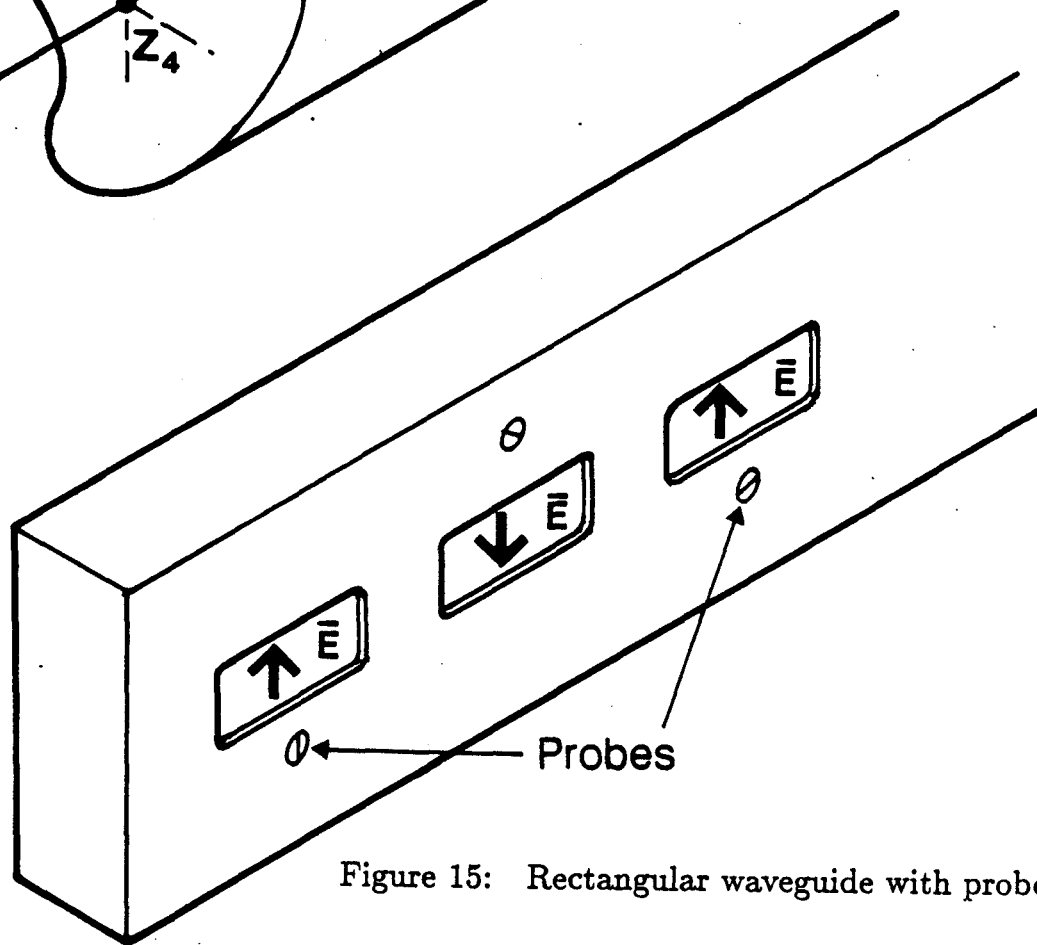
for the TM_{mn} modes, where β_{mn} is the guide propagation constant of the mode with mode numbers m and n, fields varying as $exp(j\omega t - j\mathbf{k}\cdot\mathbf{r})$ are assumed, and quantities with a 0-subscript have unit amplitude, are pure real, and depend only on m, n, x, and y. The waveguide modes are orthogonal over the cross-section of the waveguide, that is,

$$\int_{A}(\mathbf{E}_{0mn}\times\mathbf{H}_{0pq})\cdot\hat{z}dS = \begin{cases} 2S_{mn} & \text{if } m = p \text{ and } n = q \\ 0 & \text{otherwise} \end{cases} \tag{58}$$

where S_{mn} is the Poynting energy flux of the mnth mode with unit amplitude.[32]

Placing a self-excited slot from z_1 to z_2 in the wall of the infinite waveguide will excite waves in the guide that travel away from the slot. The wave fields are

$$\mathbf{E}_{g}^{t} = \sum_{mn}A_{mn}\mathbf{E}_{0mn}^{t}exp(-j\beta_{mn}z) \qquad z > z_2 \tag{59}$$

$$\mathbf{E}_{g}^{t} = \sum_{mn}B_{mn}\mathbf{E}_{0mn}^{t}exp(j\beta_{mn}z) \qquad z < z_1 \tag{60}$$

$$\mathbf{H}_{g}^{t} = \sum_{mn}A_{mn}\mathbf{H}_{0mn}^{t}exp(-j\beta_{mn}z) \qquad z > z_2 \tag{61}$$

$$\mathbf{H}_{g}^{t} = \sum_{mn}B_{mn}\mathbf{H}_{0mn}^{t}exp(j\beta_{mn}z) \qquad z < z_1 \tag{62}$$

where the coefficients A_{mn} and B_{mn} are the amplitudes of the mnth mode traveling in the positive-z and negative-z directions, respectively. To obtain the coefficients,

42

an additional relation is needed. Assuming $\mathbf{E}_g$, $\mathbf{H}_g$ and $\mathbf{E}_\dagger$, $\mathbf{H}_\dagger$ are two fields that satisfy Maxwell's Equations in free space gives

$$\nabla \cdot [\mathbf{E}_g \times \mathbf{H}_\dagger] = \nabla \cdot [\mathbf{E}_\dagger \times \mathbf{H}_g]. \tag{63}$$

Using the divergence theorem yields

$$\int_S (\mathbf{E}_g \times \mathbf{H}_\dagger - \mathbf{E}_\dagger \times \mathbf{H}_g) \cdot \mathbf{dA} = 0 \tag{64}$$

where the integration is over a closed surface S.[32]

We apply this equation to evaluate A_{mn}, choosing a surface S that includes the plane sections at z_3 and z_4 and the walls of the guide between these sections (see Figure 14). We call the fields excited in the slot $\mathbf{E}_g$, $\mathbf{H}_g$ as given by Equations 59-62, and let $\mathbf{E}_\dagger$, $\mathbf{H}_\dagger$ be a mode with unit amplitude and indices m and n propagating to the left in the waveguide. Integrating over the plane at z_3 and using the orthogonality relation (Equation 64) gives zero because the fields g and $\dagger$ are waves traveling in the same direction. Integrating at z_4 gives $-4A_{mn}S_{mn}$. For a normal waveguide mode, the tangential component of $\mathbf{E}$ must be zero at the metal wall. Therefore the second term of the integrand vanishes for the integration over the wall and we obtain

$$4A_{mn}S_{mn} = -\int_{slot} (\mathbf{E}_g \times \mathbf{H}_\dagger) \cdot \mathbf{dA} \tag{65}$$

$$= -\int_{slot} (j E_g^\tau H_{mn}^z + E_g^z H_{mn}^\tau) \exp(j\beta_{mn}z) dA \tag{66}$$

43

where the superscript τ indicates quantities in the direction $\hat{z} \times \hat{n}$ where $\hat{n}$ is the normal to the guide surface. Following a similar procedure with $\mathbf{E}_\dagger$, $\mathbf{H}_\dagger$ a normal mode of indices mn traveling to the right yields

$$4B_{mn}S_{mn} = \int_{slot} (-jE_g^\tau H_{mn}^z + E_g^z H_{mn}^\tau) \exp(-j\beta_{mn}z)dA. \qquad (67)$$

These relations can be written in terms of the surface current $\mathbf{K}_{mn}$ that would exist in the region of the slot if there were no slot. The above equations then become

$$4A_{mn}S_{mn} = \int_{slot} (jE_g^\tau K_{mn}^\tau - E_g^z K_{mn}^z) \exp(j\beta_{mn}z)dA \qquad (68)$$

$$4B_{mn}S_{mn} = \int_{slot} (jE_g^\tau K_{mn}^\tau + E_g^z K_{mn}^z) \exp(-j\beta_{mn}z)dA \qquad (69)$$

where K_{mn}^τ and K_{mn}^τ depend only on m, n, x, and y.

Proceeding to the explicit evaluation of the slot conductance, we are interested in resonant slots (perimeter $\approx \lambda$) in rectangular waveguide that are long and narrow, with the long axes parallel to the guide axis (see Figure 15). The guide propagates only the dominant TE$_{10}$-mode. For this case we would expect that $A_{mn} = B_{mn}$ because the slot is symmetric in z. In the slot, $E_g^z = 0$ so the second terms in the integral vanish. Also, K_{mn}^τ is constant and E_g^τ is an even function along the slot, so that only the real parts of the phase factors contribute to the integrals, resulting in $A_{mn} = B_{mn}$. Thus the slot is a *shunt* element in the transmission-line model of the waveguide. The following assumptions are made:[32] [33]

1. $2\log_{10}$(length of slot/width of slot) $\gg 1$.

2. The guide walls are perfectly conducting and infinitely thin.

3. The field in the slot is in the y-direction and sinusoidal in the z-direction.

4. The radiated field is zero behind the slotted face. This is equivalent to extending this face into an infinite, perfectly-conducting plane.

Assumption 3, in good agreement with experimental conditions, gives the following:

$$E_g^\tau = E_0 \cos(kz) \tag{70}$$

$$E_g^z = 0 \tag{71}$$

where E_0 is the field in the center of the slot. The other quantities in Equations 68 and 69 are the following:

$$K_{10}^\tau = -Y_{10}^0 \frac{\pi}{\beta_{10}a} \sin\left(\frac{\pi x_1}{a}\right) \tag{72}$$

$$S_{10} = Y_{10}^0 \frac{ab}{4} \tag{73}$$

$$\beta_{10}^2 = k^2 - \left(\frac{\pi}{a}\right)^2 \tag{74}$$

and

$$A_{10} = B_{10} \tag{75}$$

where Y_{10}^0 is the characteristic admittance of the TE_{10}-mode at $z = 0$, a and b are the dimensions of the waveguide, x_1 is the distance from the slot axis to the

45

centerline of the slotted face of the guide, and E_{g0} is the field across the center of the guide. Substituting these into Equations 68 and 69 gives

$$A_{10} = B_{10} = -jwE_0 \frac{2}{\pi b} \left(\frac{k}{\beta_{10}} \right)^2 \sin \left(\frac{\pi x_1}{a} \right) \cos \left(\frac{\beta_{10}\lambda}{4} \right) \tag{76}$$

where w is the slot width.

The reflection coefficient $\Gamma(z)$ in a transmission line is related to the normalized admittance $y(z)$ by

$$\Gamma(z) = \frac{1 - y(z)}{1 + y(z)} \tag{77}$$

$$y(z) = \frac{1 - \Gamma}{1 + \Gamma} \tag{78}$$

For a resonant slot, $\Gamma(z = 0)$ must be real because the slot admittance is real and therefore the normalized admittance looking to the right at $z = 0$, $y(0) = 1 + g$ is real, where $g = G/Y_{10}^0$ is the conductance of the slot normalized to the characteristic admittance of the TE_{10}-mode. Thus

$$g = \frac{-2}{1 + \frac{1}{\Gamma}} \tag{79}$$

Note that $\Gamma = A_{10}$, because the incident wave—from the left—has unit amplitude and A_{10} is the magnitude of the wave reflected to the left by the slot.

To find Γ, we set the Poynting flux through the closed surface shown in Figure 14 equal to zero. This includes the power from the incident TE_{10}-mode from the left, the power scattered by the slot in both directions in the guide, and the radiated power. We find the radiated power by using Babinet's Principle[34] to determine the

46

radiation resistance of a resonant slot. The radiation resistance of a center-driven, resonant slot in an infinite, perfectly conducting sheet is

$$R_r = \frac{1}{4 \times 73} \frac{\mu_0}{\epsilon_0} \tag{80}$$

The radiation resistance of the resonant waveguide-slot is twice this, because it radiates to one side only. Thus the radiated power is

$$\frac{1}{2} \frac{V_0^2}{2R_r} = 73 V_0^2 \frac{\epsilon_0}{\mu_0} \tag{81}$$

where $V_0 = E_0 w$ is the voltage across the center of the slot. The incident power from the left in the guide is S_{10} and the reflected power is $\Gamma^2(0)S_{10} = A_{10}^2 S_{10}$. Because $\Gamma(0)$ is real the phase of the wave scattered to the right by the slot is not shifted, and the total amplitude of the right-traveling wave is $1 + B_{10}$. The transmitted power is

$$S_{10}(1 + B_{10})^2 = S_{10}(1 + A_{10})^2 \tag{82}$$

The energy-balance equation is

$$S_{10} = S_{10}A_{10}^2 + S_{10}(1 + A_{10})^2 + 73 V_0^2 \frac{\epsilon_0}{\mu_0} \tag{83}$$

so that, using $A_{10} = \Gamma$ and $V_0 = E_0 w$,

$$1 + \frac{1}{\Gamma} = -73 \frac{\epsilon_0}{\mu_0} \frac{E_0^2 w^2}{2 S_{10} A_{10}^2} \tag{84}$$

47

Using Equations 70-76 to describe $A_{10} = E_{g0}$ in terms of the characteristic admittance of the TE_{10}-mode and substituting the resulting Γ into Equation 79 yields[32]

$$g = \frac{480}{73\pi} \frac{a}{b} \frac{\lambda_g}{\lambda} \cos^2\left(\frac{\pi\lambda}{2\lambda_g}\right) \sin^2\left(\frac{\pi x_1}{a}\right) \tag{85}$$

Figures 16 and 17 show data obtained by Dodds, et. al. on the admittance of longitudinal slots in rectangular waveguide immersed in free-space.[35]

2.2.2 Arrays

Consider radiation from a single-row array of slots in rectangular waveguide as shown in Figure 18. The array is excited by the TE_{10}-mode propagating in the guide. Each slot is excited in its own TE_{10}-mode and picks a single average phase at which to radiate. We are primarily interested in the Fourier spectrum of the array, so that we may calculate the near-field. However, calculating the far-field allows us to develop a neat graphical method for predicting the near-field spectrum (therefore designing the antenna), and it provides a comparison with measurements of the antenna's far-field.

The far-field of an array of radiating elements is the product of the element factor and the array factor. The element factor is the radiation pattern from one slot and the array factor is the pattern that would be obtained from the array if the slots were isotropic radiators. Similarly, the transform of the field in the slots (the source field) is the product of the transform of the field of one slot and the transform of an array of N impulse functions located at the slot centers, that is, the source field is the one-slot field convolved with a train of N impulses. The simplest

48
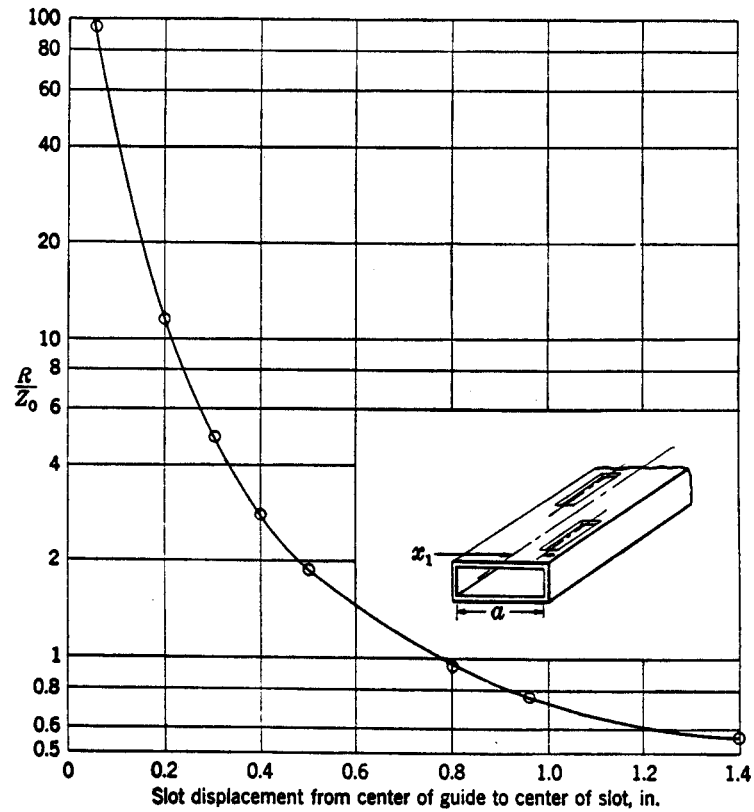
Figure 16: Resistance of longitudinal slot versus its distance from the center. The data fit the relation $G = Z_0/R = 1.73 \sin^2(\pi x_1/a)$ (see Equation 85). (From reference [35].)

49

Figure 17: Admittance of longitudinal slot versus frequency (from reference [35]).

Figure 18: Rectangular waveguide with single row of off-center slots.
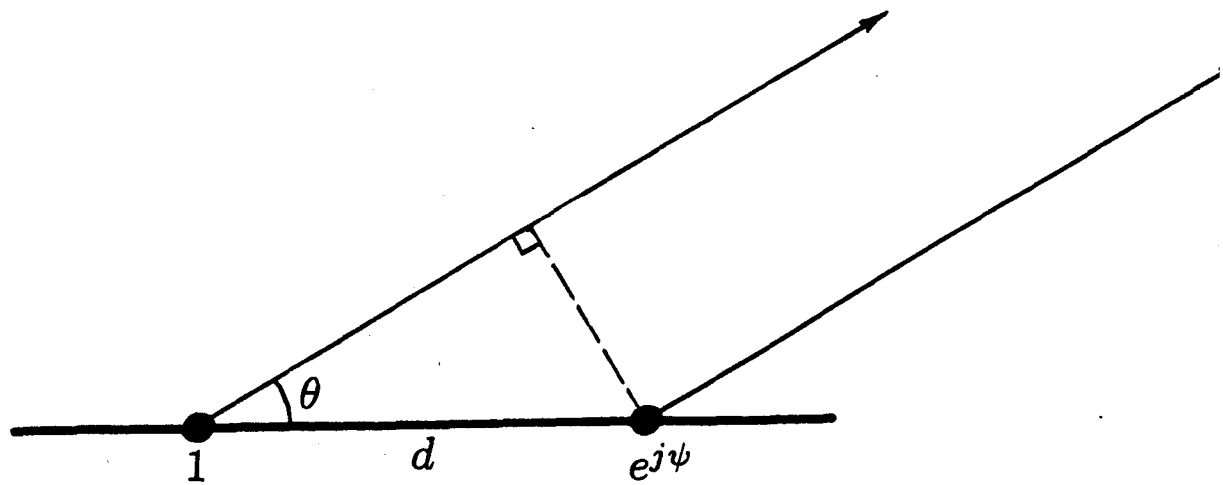
Figure 19: Interference maxima. Constructive interference occurs for
$\psi + kd\cos\theta = m2\pi$, where $k = \omega\sqrt{\epsilon_0\mu_0}$ and $m = 0, \pm1, \pm2, \dots$.

way to find the maxima of the array factor is to determine the condition for far-field constructive interference. For the array shown in Figure 18,

$$\psi = -\beta d \tag{86}$$

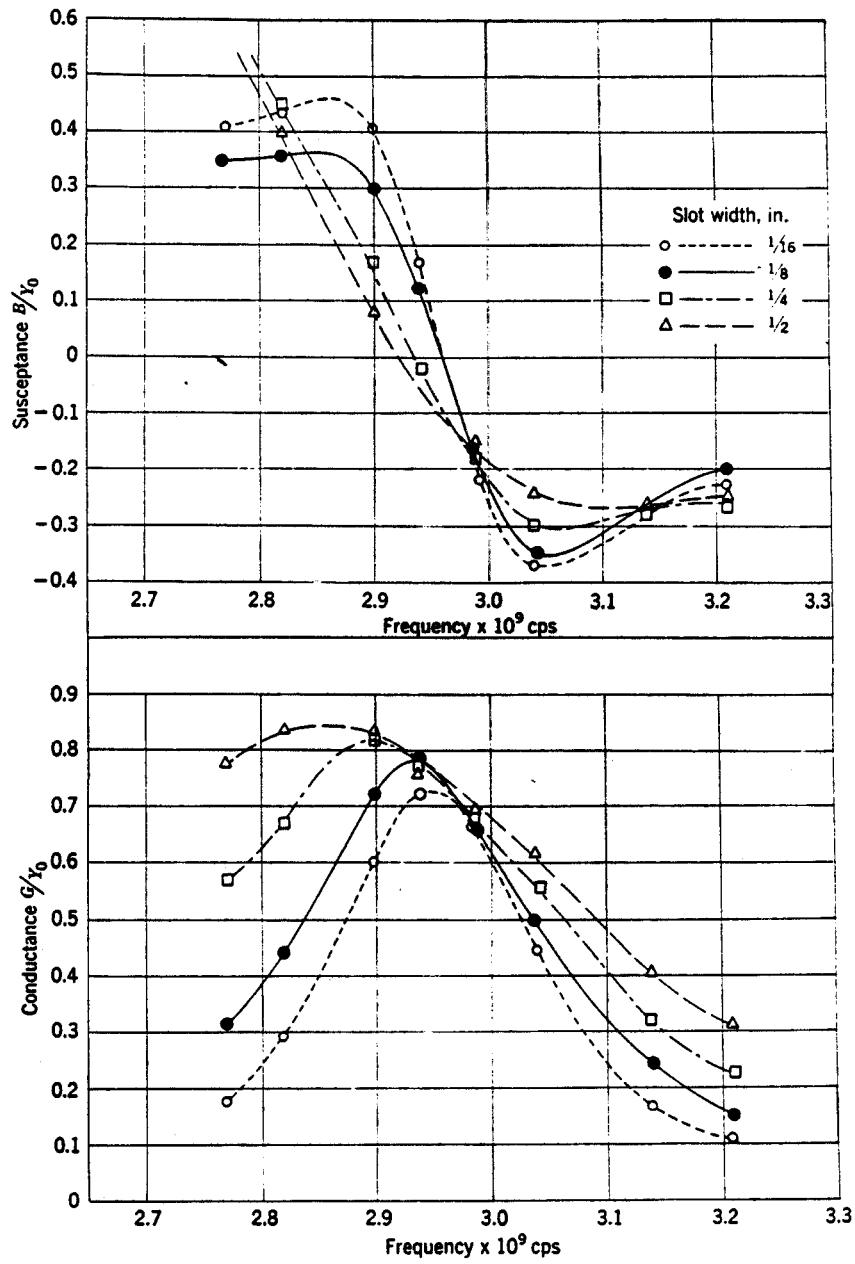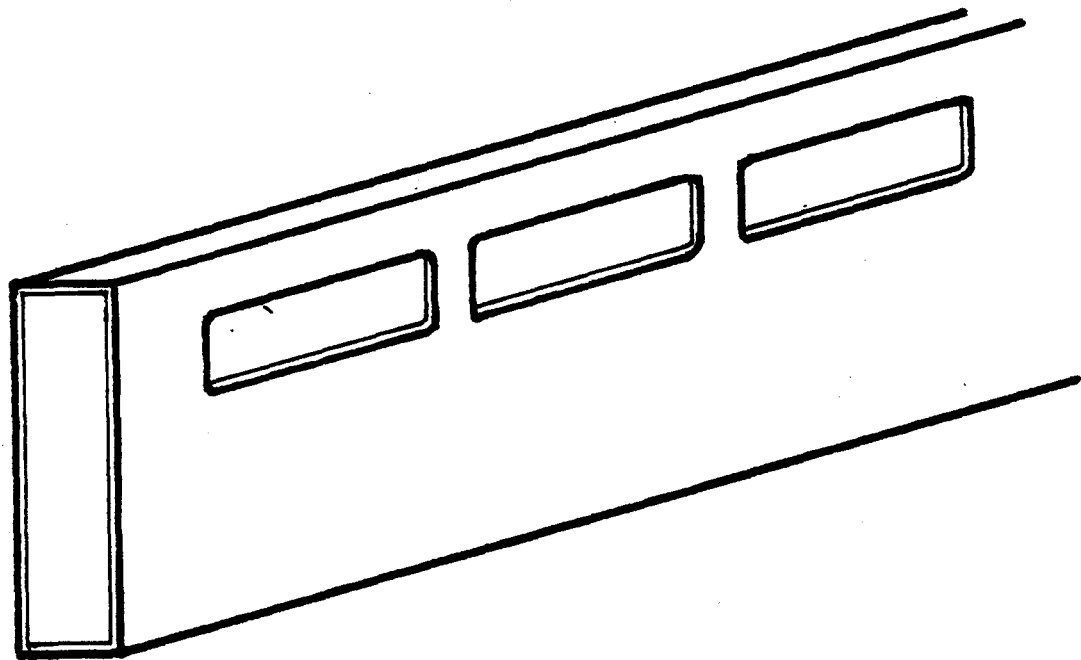where ψ is the phase angle between fields of adjacent slots, d is the slot spacing and β is the propagation constant in the guide. For the probe-fed array shown in Figure 15,

$$\psi = \pi - \beta d \tag{87}$$

So from Figure 19,

$$\psi + kd\cos\theta = m2\pi, \qquad m = 0, \pm1, \pm2, \ldots . \tag{88}$$

Defining $N_\parallel = ck_\parallel/\omega = (ck/\omega)\cos\theta$, we get

$$\psi + N_\parallel \frac{d\omega}{c} = m2\pi. \tag{89}$$

For the array of Figure 18,

$$d = \frac{2m\pi c}{N_\parallel \omega - c\beta} \tag{90}$$

and for the probe-fed array of Figure 15,

$$d = \frac{(2m-1)\pi c}{N_\parallel \omega - c\beta} \tag{91}$$

52

where c is the speed of light, ω is the wave frequency, k is the wave number, and $\parallel$ indicates a component parallel to the array axis. Equations 90 and 91 are used to plot d versus $N_\parallel$ for various m in Figures 20 and 21.

Note that for any fixed slot-spacing d, there is a countably infinite number of $N_\parallel$'s that satisfy the constructive interference condition. The medium determines which can be identified with a propagating wave. For a single row of slots that are not probe-fed,

$$k_\parallel = \frac{2\pi m}{d} + \beta \tag{92}$$

so there is always a radiation peak at $k_\parallel = \beta$ (corresponding to $m = 0$), independent of d.

To illustrate the design procedure, suppose we wish to design a probe-fed antenna that radiates as much power as possible near $|N_\parallel| = 1.4$ and is made from WR-340 waveguide ($1.7'' \times 3.4''$ inside dimensions). The operating frequency is 2.45 GHz. Using Figure 22, we draw vertical lines at $N_\parallel = \pm 1.4$, then draw horizontal lines through the intersections of the vertical lines and the lowest-order curves—here $m = 0$ and $m = 1$. The best solution is at point A, which gives the smallest slot spacing, because this solution forces the next solution, $m = 1$ at point C, to be as far away from $N_\parallel = 0$ as possible. We see this by traveling horizontally from points A and B. Many more maxima will be produced in the range $-5 < N_\parallel < 5$ with a slot spacing of 8.8 cm (point B) than with a slot spacing of 2.9 cm (point A). Because the full spectrum of the source field is the product of the "array factor" and the spectrum from an individual slot—shown in Figure 23—the contribution of a particular solution of Equation 91 is greatly reduced if it is far to the left or right in Figure 22. The two-dimensional spectrum is shown in Figure 24 for a slot spacing of 2.9 cm, slot length of 2.7 cm, and slot width of 1 cm. Note the principal maximum at $N_\parallel = -1.4$ and the smaller but unavoidable maximum at $N_\parallel = +2.8$ (point C in Figure 22).
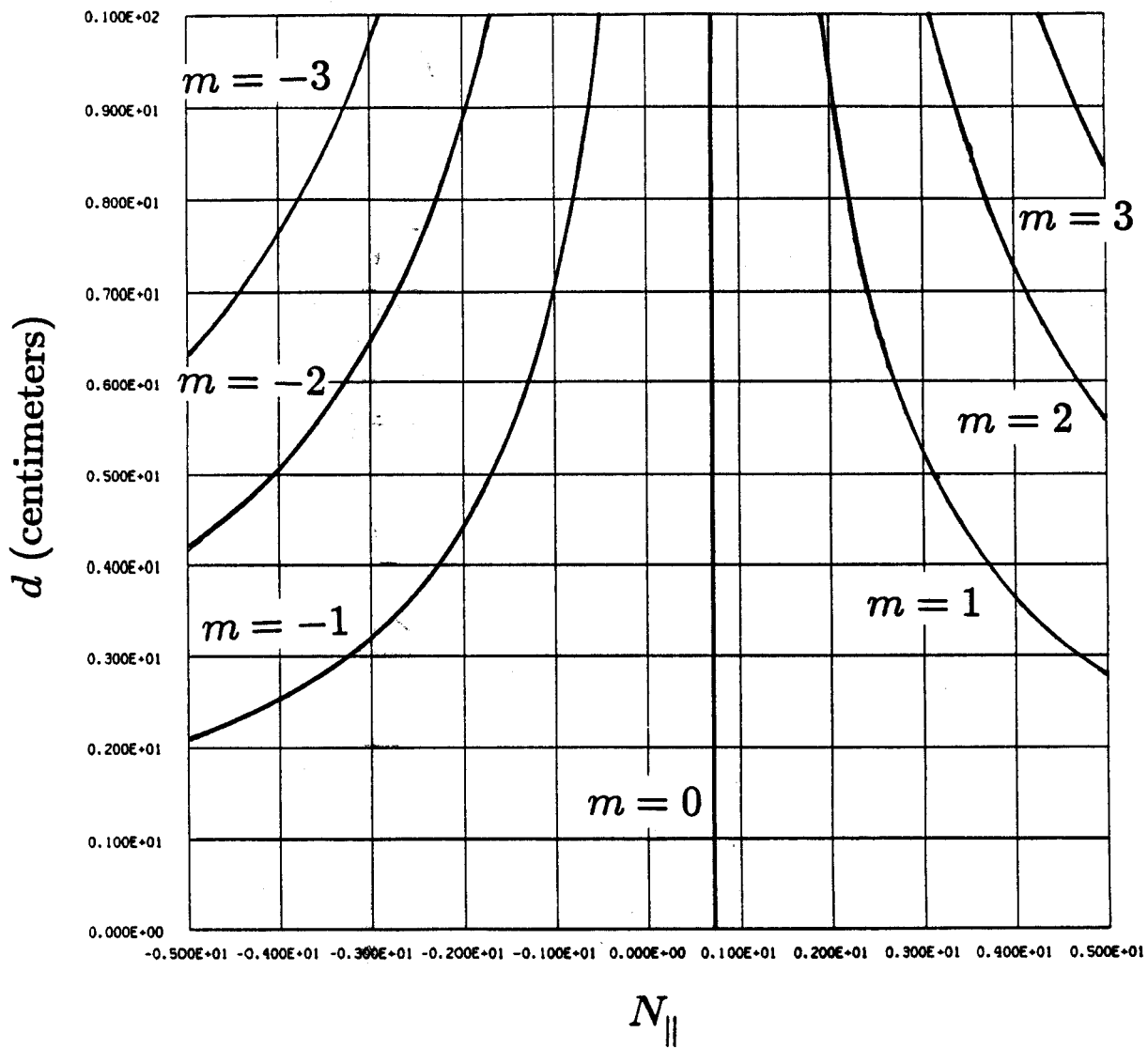
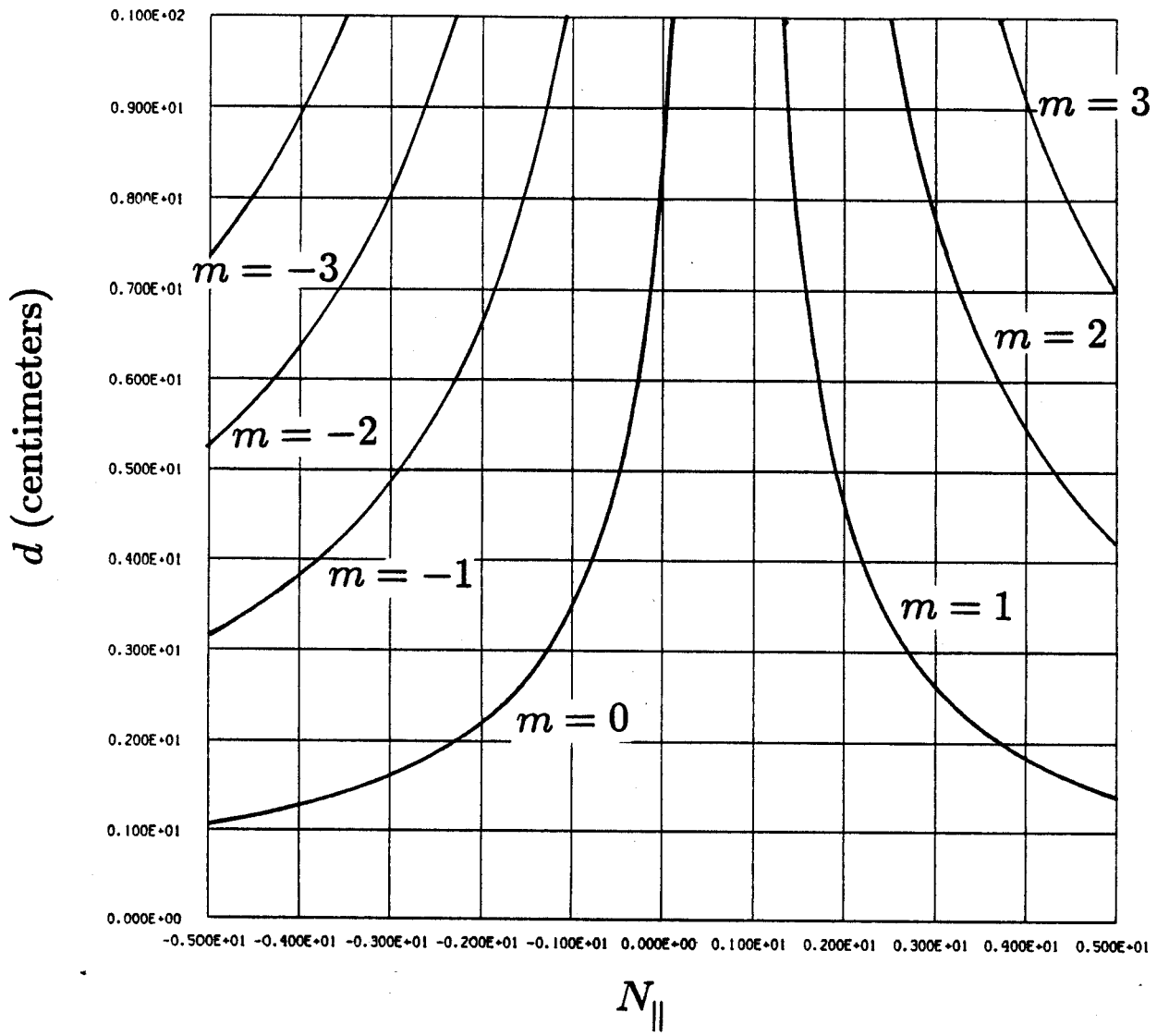Figure 20: Plot of interference maxima for non-probe-fed slots.

Figure 21: Plot of interference maxima for probe-fed slots.

Figures 25 and 26 show the interference plot, element factor, and spectrum for the antenna used in the experiments discussed in this thesis. A much-improved design incorporating probe-fed slots[36] [37] is shown in Figure 27.

2.3 Spectrum and Coupling

The full coupling calculation for the slotted-waveguide is beyond the scope of this thesis, But an approach will be outlined for future work and approximations justifying the design method of section 2.2.2 will be explained.

A real antenna is not infinite, and hence it produces a Fourier spectrum, or superposition of plane waves. This spectrum is the Fourier transform of the space-dependent fields at the source; it must contain as much power as possible in spectral components accessible to the plasma core.

The plasma near the antenna acts like a filter, modifying the spectrum before it is transmitted to the bulk of the plasma. This transmitted spectrum determines the accessibility of the power to the plasma core and the current-drive efficiency. The filtering effect of the coupling region can be encapsulated into a plasma admittance $Y(k_y, k_z)$[38] where k_y and k_z are the poloidal and toroidal wave numbers (Fourier transformed coordinates), respectively. The coupling has been rigorously calculated for the waveguide grill,[39] but not for the slotted waveguide. The calculation for the slotted-waveguide is more complicated because all the modes in the slots are evanescent and the fields in the guide behind the slot are unknown.
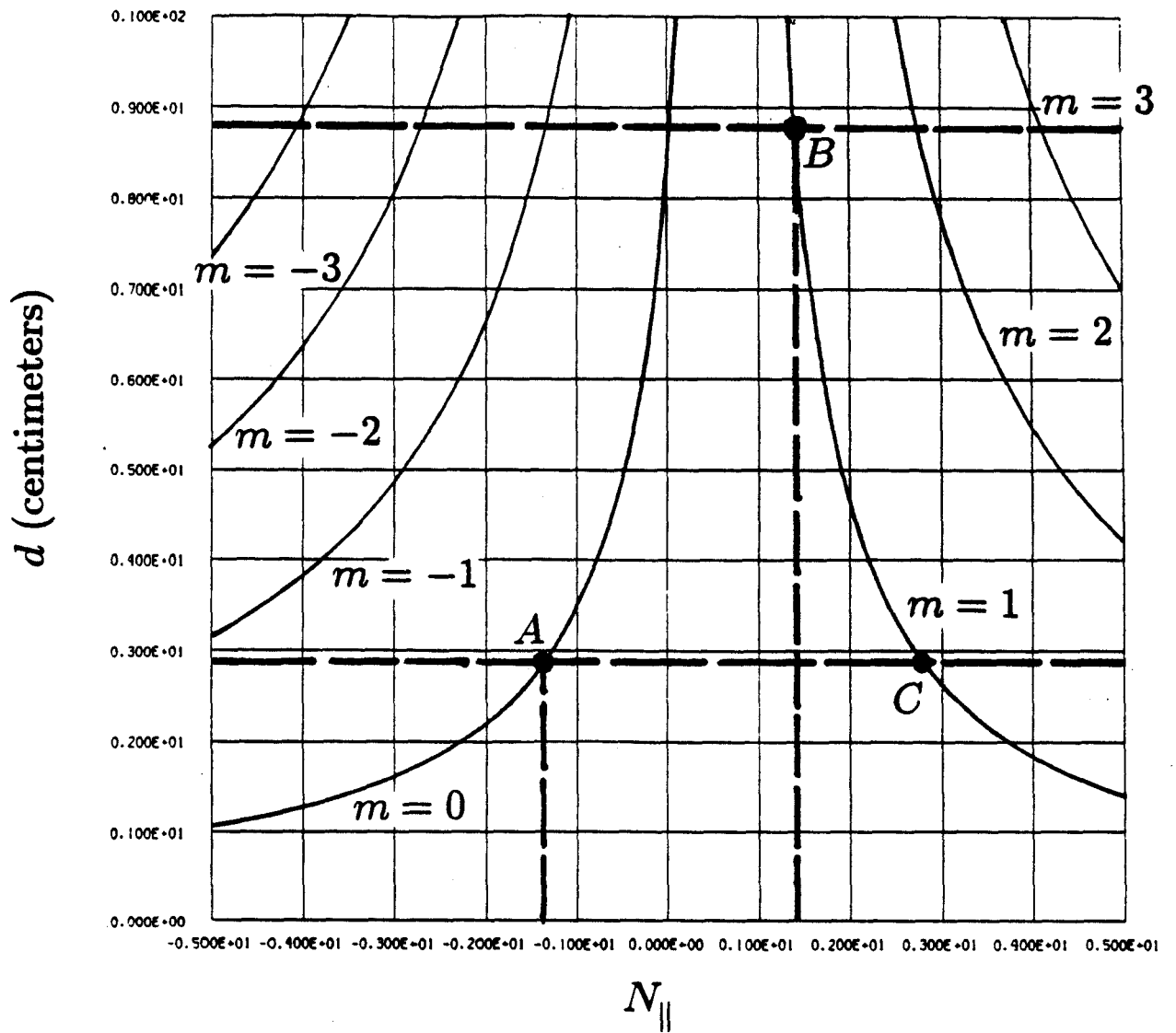
Figure 22: Construction of design for probe-fed antenna radiating at $N_{\|} = -1.4$
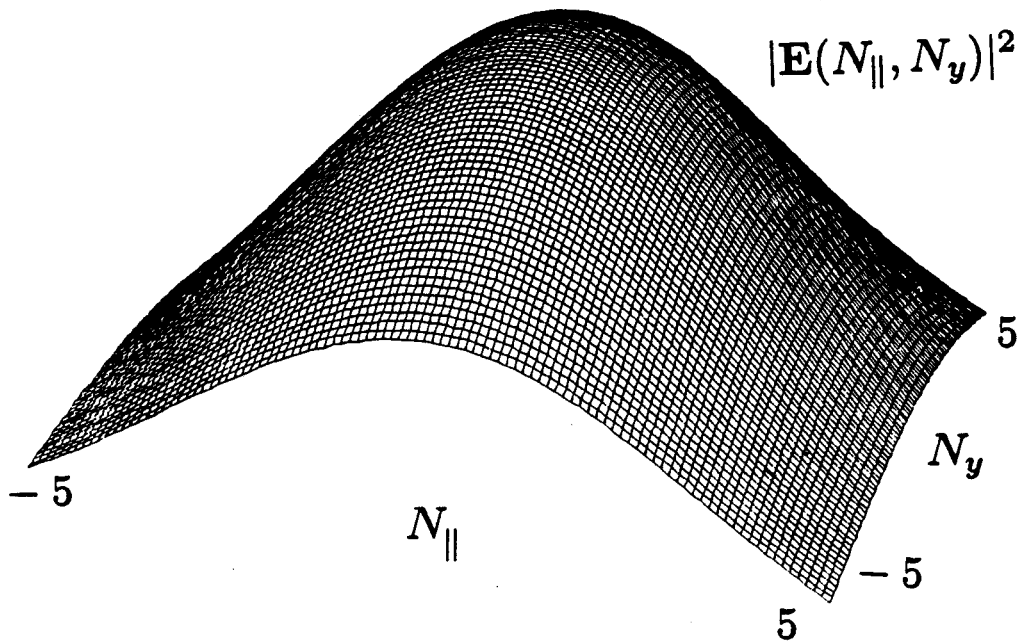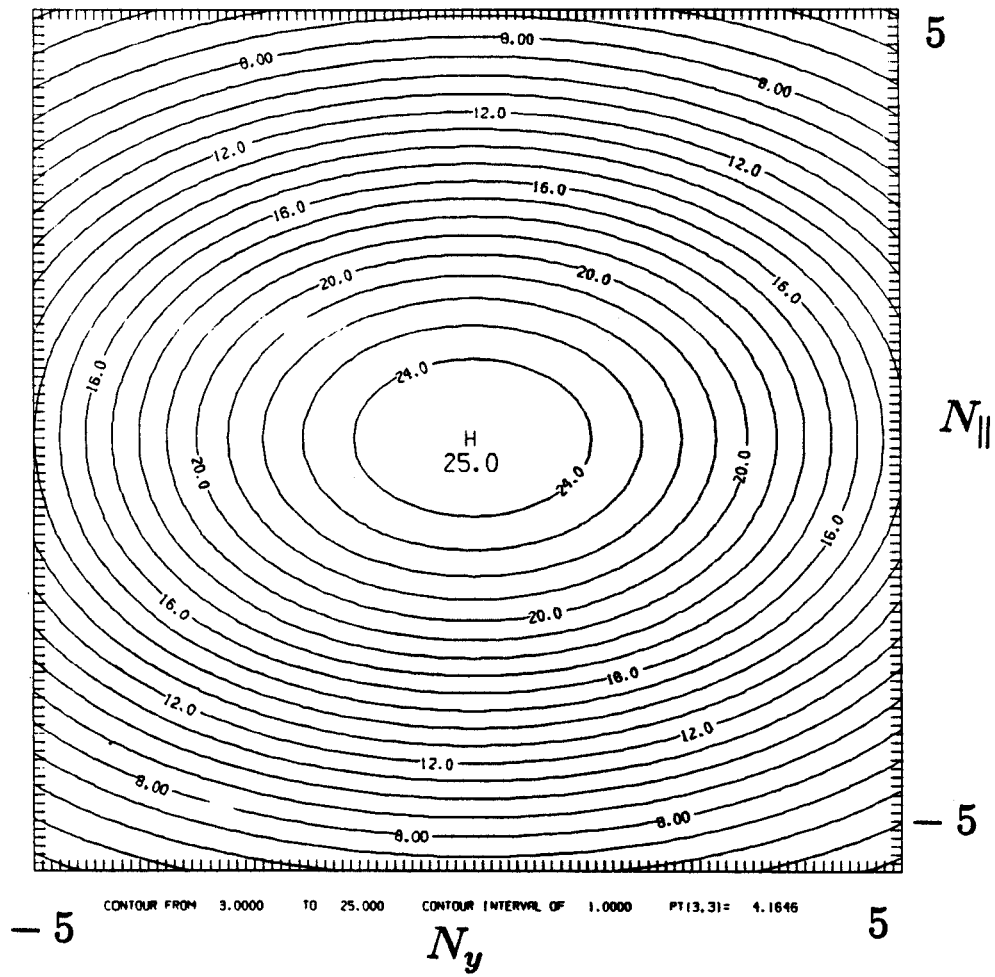
Figure 23: Spectrum of one slot 2 cm × 1 cm.
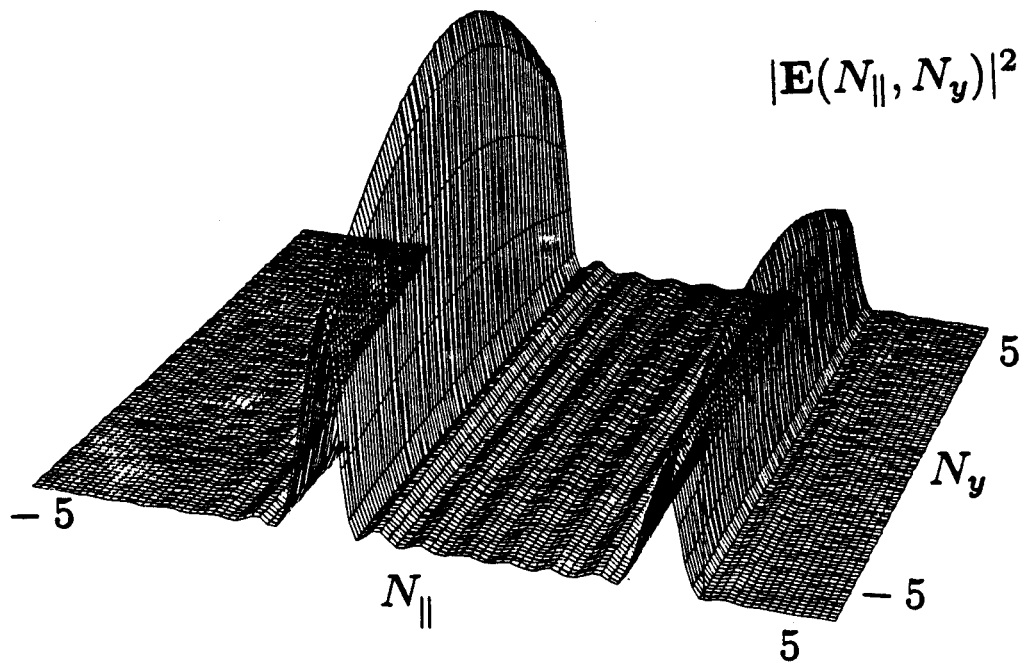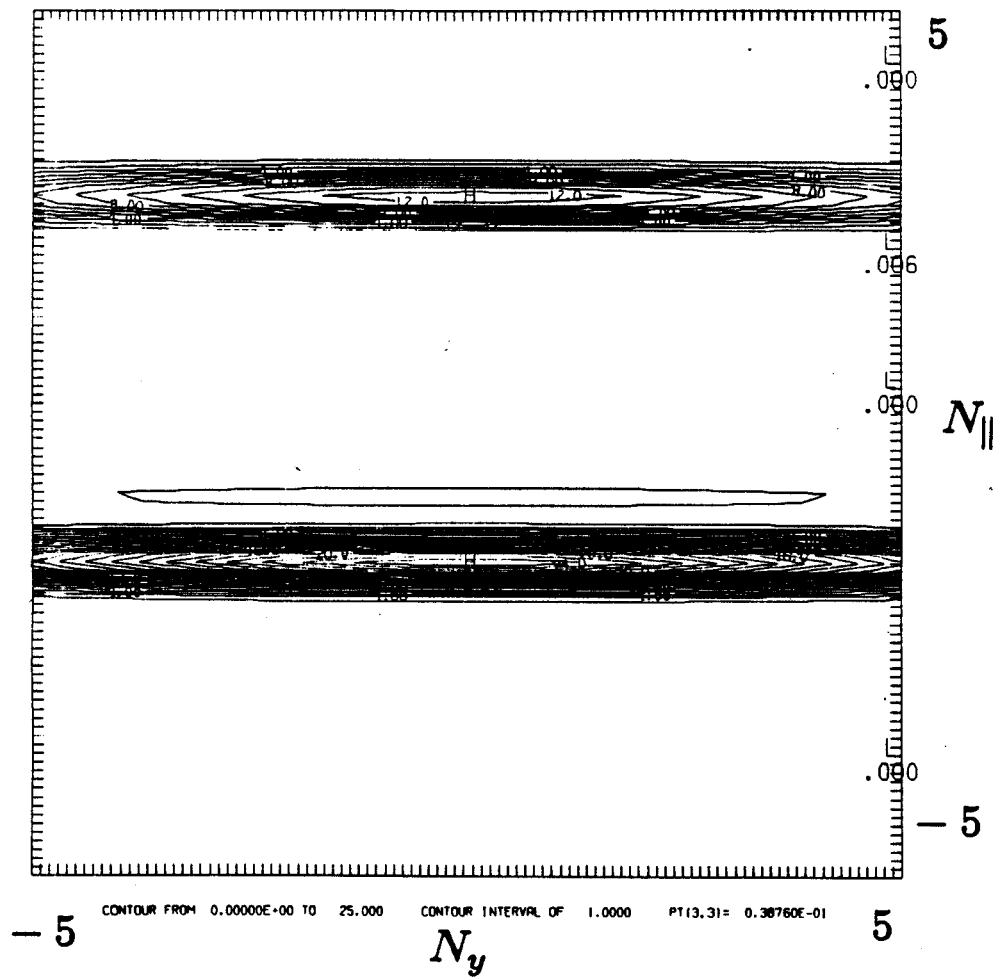
Figure 24: Spectrum of a probe-fed array of eight slots designed to radiate at $N_\| = -1.4$.
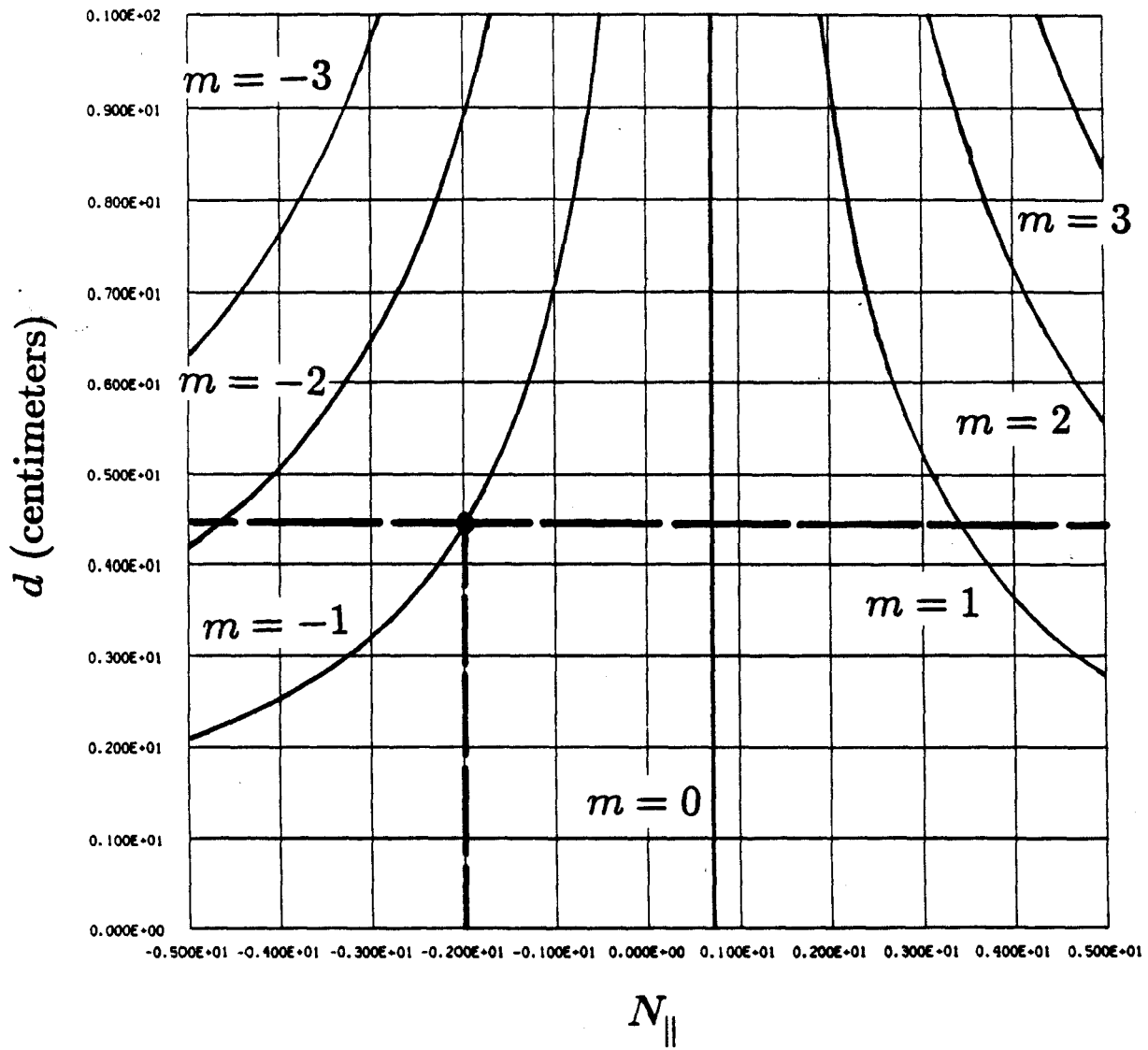
Figure 25: Interference plot for the antenna used on Versator-II.

CONTOUR FROM 0.00000E+00 TO 25.000   CONTOUR INTERVAL OF 1.0000   PT(3,3)= 0.34843E-03
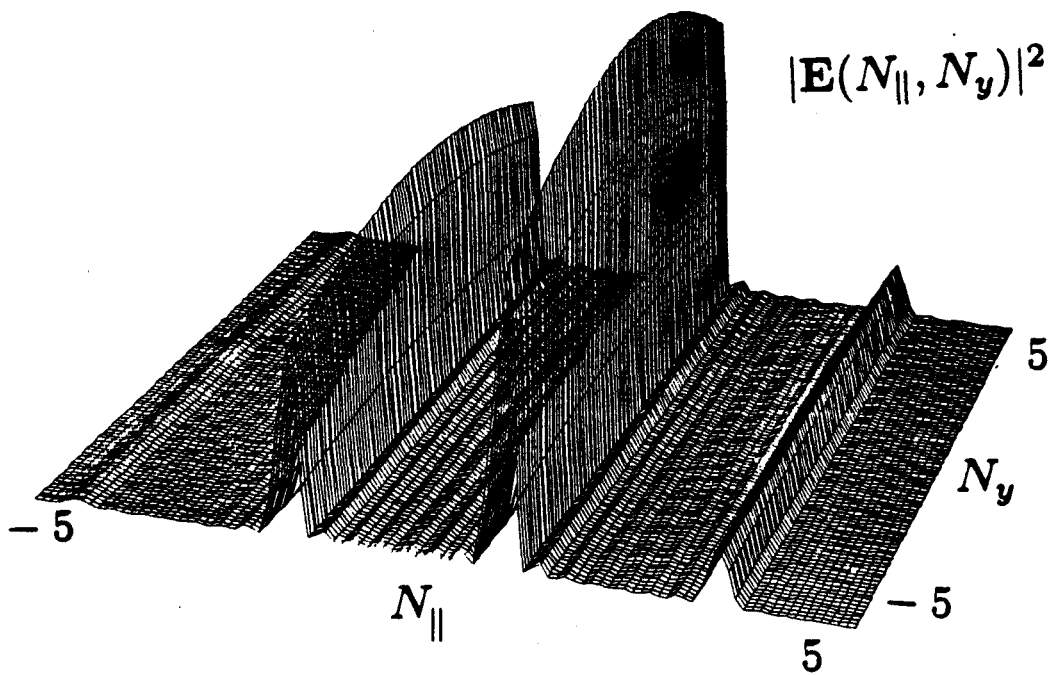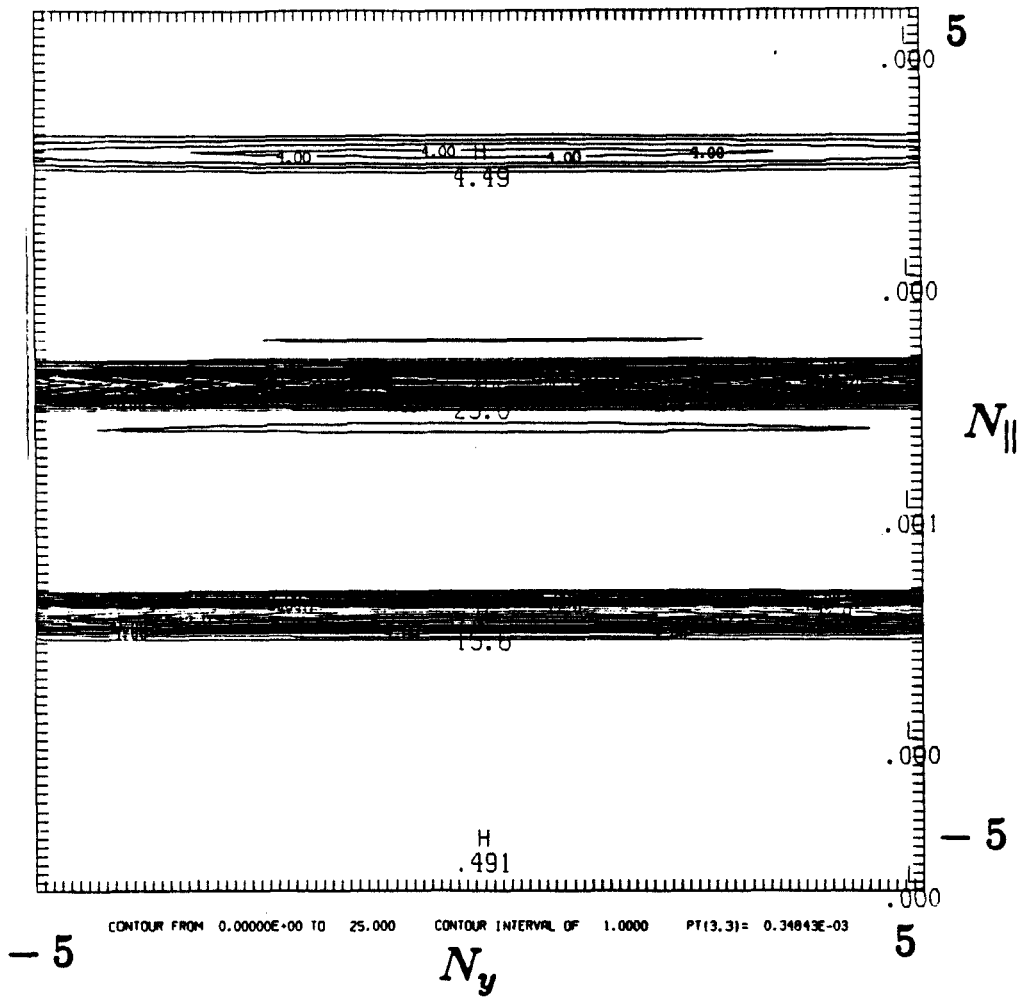
Figure 26: Spectrum of the antenna used on Versator-II.
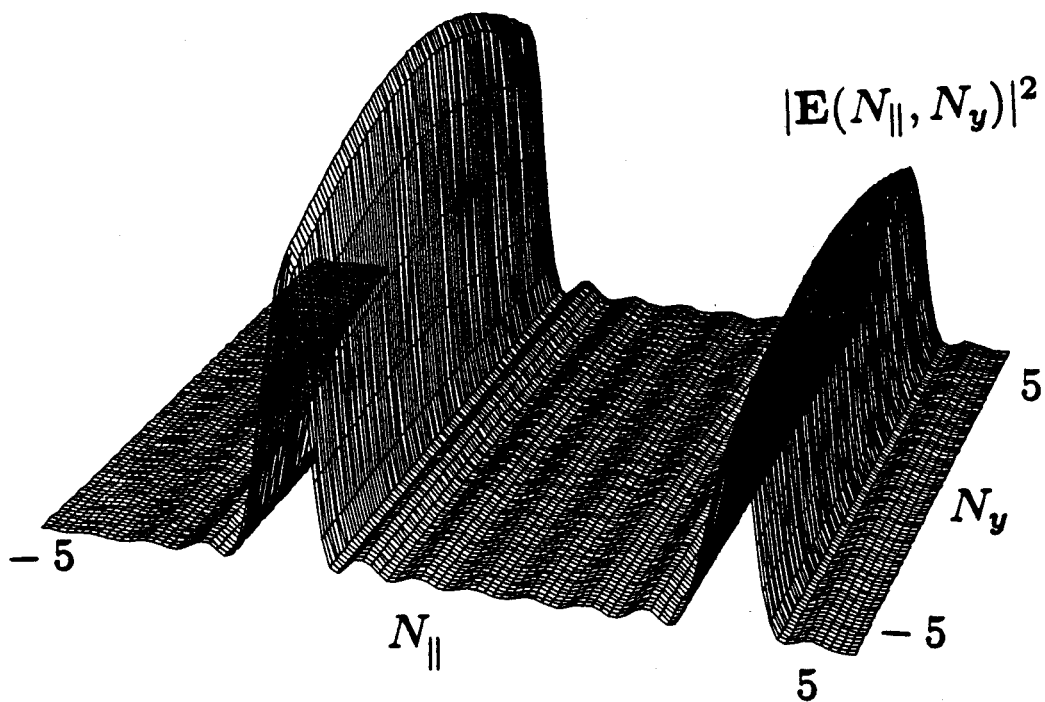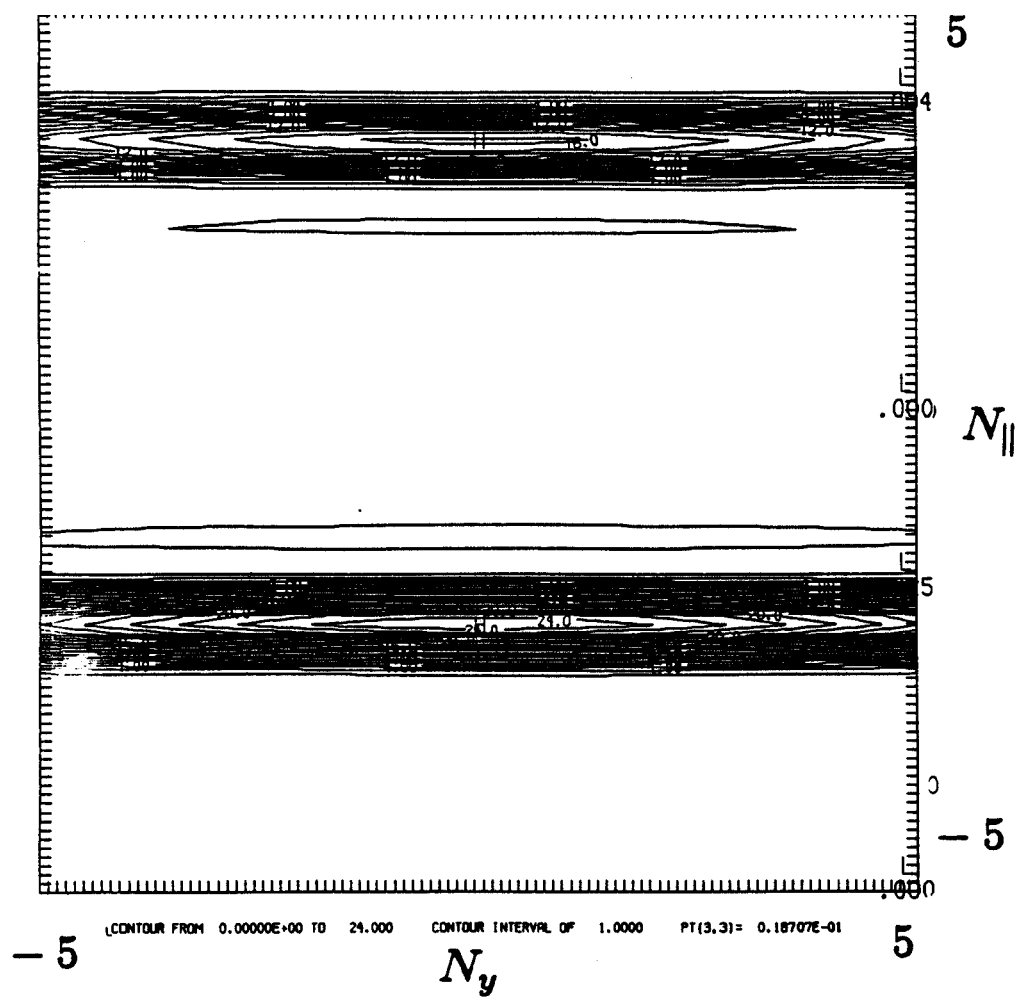
Figure 27: Spectrum of probe-fed antenna design radiating at $N_\parallel = -2$.

To solve the coupling problem for the slotted-waveguide, the slots are treated as waveguides, with a length equal to the wall-thickness of the main waveguide and transverse dimensions equal to the dimensions of the slot. At the operating frequency (for a resonant slot), all modes in the "slot-waveguide" are evanescent. The following approximations are made. The main waveguide propagates only the TE_{10}-mode. The plasma density is as shown in Figure 28, i. e. , there is a vacuum region just outside the antenna, followed by a plasma region with some arbitrary initial density and density gradient. The vacuum region is for analytical convenience and can be infinitesimally thin, but the plasma does not enter the slots. Inside the waveguide, the slots do not couple to each other, i. e. , the evanescent waves reflected into the guide by one slot do not reach another. The dogbone-shaped slots (so shaped to minimize their length while maintaining the resonant condition *perimeter* $\approx \lambda$) used on the Versator-II slotted-waveguide fast-wave coupler are modelled as rectangular. Only TE_{n0}-modes are excited in the slots. Slab geometry is used, as shown in Figure 29, and the guide is straight. The face of the antenna is flush with an infinite conducting sheet, and the plasma does not vary in the y- or z-directions.

The coupling calculation yields the total reflection coefficient and the power spectrum transmitted into the plasma, given certain plasma parameters. The outline of the calculation is as follows. First, a superposition of evanescent TE_{n0}-modes is assumed for each slot. Then, Equations 66 and 67 are used to obtain the fields of the propagating TE_{10}-modes produced in the guide traveling away from each slot. Each of these is proportional to a summation involving the amplitudes of the evanescent modes in the slot. A transmission-line analogy is then made, treating the slots as shunt elements. The power dissipated in the transmission-line element representing each slot is then equated to the Poynting flux leaving the slot. Keeping only the lowest-order evanescent mode in each slot, this yields a set of P equations for the $2P$ unknown mode amplitudes (forward and reflected). Next, the formalism
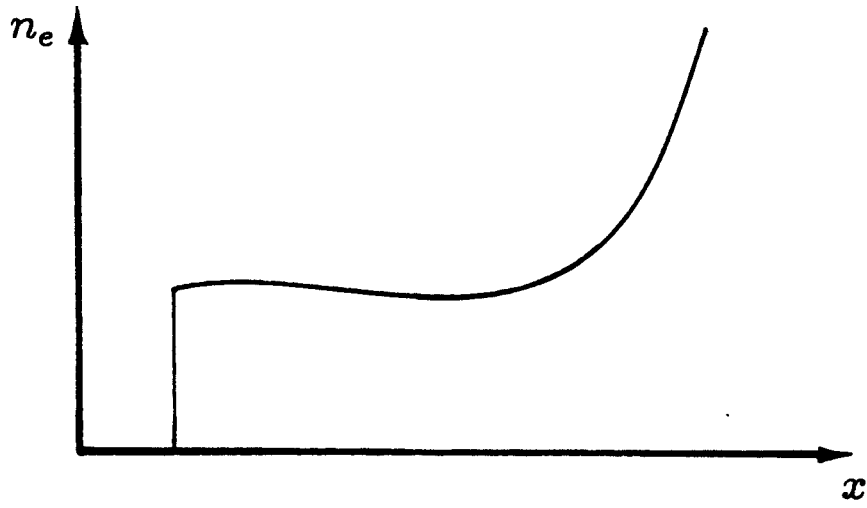
Figure 28:   Density versus distance fron the antenna for coupling calculation.
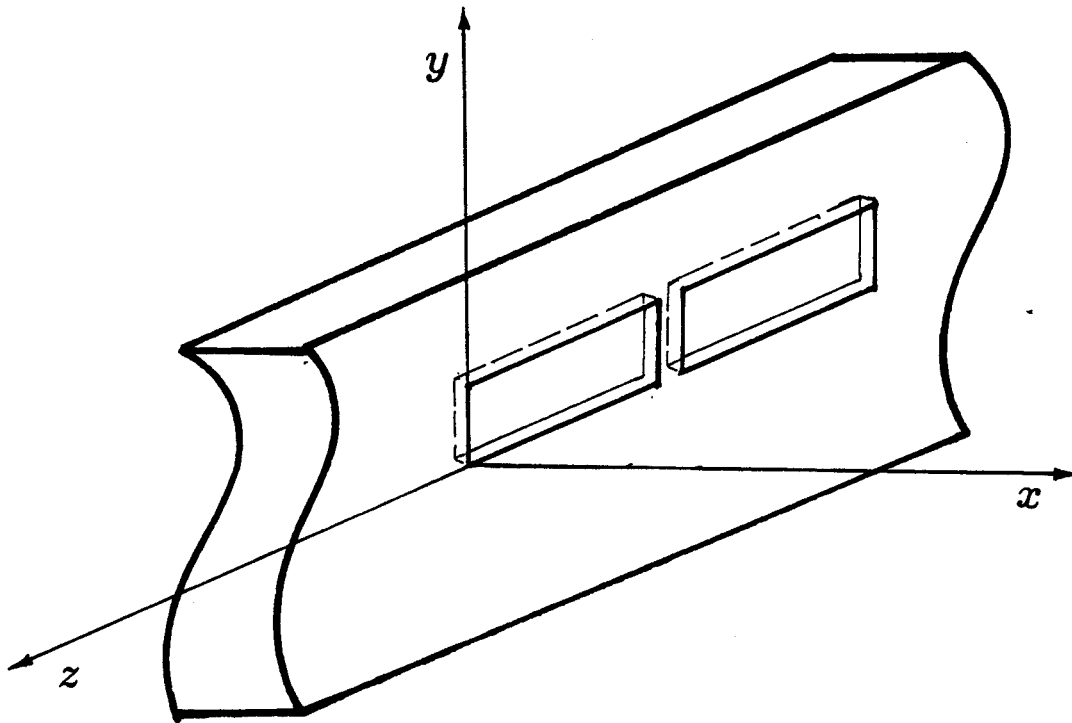
Figure 29:   Coordinate system for the coupling problem, using slab geometry.

introduced by Brambilla[38] is used to obtain an additional set of P equations relating the amplitudes of the forward- and backward-decaying evanescent modes in the slots. Combining these two sets gives one set of equations for all the modes in the slots in terms of $Y(k_y, k_z)$ and the slot dimensions. This system can be numerically inverted to yield the amplitudes of the slot-modes, the total reflection coefficient of the antenna, and the power spectrum transmitted into the plasma.

Equations 66 and 67 give the amplitude of the nmth propagating mode in a waveguide produced by a known field in a slot.[32]

$$4A_{nm}S_{nm} = \int_{slot} (-jE_g^y H_{nm}^z - E_g^z H_{nm}^y)e^{j\beta_{nm}z}dA \qquad (93)$$

$$4B_{nm}S_{nm} = \int_{slot} (-jE_g^y H_{nm}^z + E_g^z H_{nm}^y)e^{-j\beta_{nm}z}dA \qquad (94)$$

where A_{nm} is the amplitude of the right-traveling wave, and B_{nm} is the amplitude of the left-traveling wave.

Assuming the fields in the pth slot are superpositions of forward- and backward-decaying evanescent TE$_{n0}$-modes,

$$\mathbf{E}_p = \hat{y} \sum_{n=1}^{\infty} \sin nk_0(z - z_p) \left(\Phi_{pn}e^{-\gamma_n x} + \mathrm{R}_{pn}e^{\gamma_n x}\right) \qquad (95)$$

where the length of the slot is $\lambda/2$, λ is the free-space wavelength, Φ_{pn} and R_{pn} are the amplitudes of the nth forward- and backward-decaying modes in the pth slot, z_p is the z-coordinate of the edge of the pth slot, and γ_n is the decay constant of the nth mode.

Narrow slots that are long in the axial direction along the waveguide contain fields polarized only in the y-direction; Resonant slots are $\lambda/2$ long. Because only

the TE_{10}-mode propagates in the waveguide, only A_{10} and B_{10} are needed. The second terms of the integrands are zero because E_g^z is zero in the slot. The other quantities in Equations 66 and 67 are the following:

$$S_{10} = \frac{ab\beta_{10}}{4\omega\mu_0} \tag{96}$$

$$H_{10}^z = \frac{-j\pi}{\omega\mu_0 a} \sin \frac{\pi y}{a} \tag{97}$$

and E_g^y is obtained by setting $x = -t$ in Equation 95:

$$E_g^y = \sum_{n=1}^{\infty} \sin nk_0(z - z_p) \, (\Phi_{pn}e^{\gamma_n t} + R_{pn}e^{-\gamma_n t}). \tag{98}$$

Here S_{10} is the integrated Poynting flux for the TE_{10}-mode with unit amplitude in the waveguide, a and b are the guide dimensions, β_{10} is the propagation constant in the guide of the TE_{10}-mode, and H_{10}^z is the z-component of the magnetic field of the TE_{10}-mode. Substituting into Equations 66 and 67 and integrating gives the following:

$$A_{pn}^{10} = \frac{-w\pi}{2ja^2b\beta_{10}} \sin \frac{\pi y}{a}$$
$$\times \sum_{n=1}^{\infty} (\Phi_{pn}e^{\gamma_n t} + R_{pn}e^{-\gamma_n t}) \left[\frac{e^{jn\pi + j\beta_{10}\lambda/2} - 1}{j2\pi n/\lambda + \beta_{10}} - \frac{e^{-j\pi n + j\beta_{10}\lambda/2} - 1}{-j2\pi n/\lambda - j\beta_{10}} \right] \tag{99}$$

$$B_{pn}^{10} = \frac{-w\pi}{2ja^2b\beta_{10}} \sin \frac{\pi y}{a}$$
$$\times \sum_{n=1}^{\infty} (\Phi_{pn}e^{\gamma_n t} + R_{pn}e^{-\gamma_n t}) \left[\frac{e^{jn\pi - j\beta_{10}\lambda/2} - 1}{j2\pi n/\lambda - j\beta_{10}} - \frac{e^{-j\pi n - j\beta_{10}\lambda/2} - 1}{-j2\pi n/\lambda - j\beta_{10}} \right] . \tag{100}$$

66

To make the problem more tractible, we now assume only the first evanescent mode exists in the slots, so the field is sinusoidal across the length of the slot. The n subscript is dropped. The coefficient R_p is not zero, however. Because the field is an even function along the slot, the imaginary parts of Equations 66 and 67 vanish, making A_p^{10} and B_p^{10} pure real. This allows us to model the slots as *shunt conductances* in a transmission line,[32] as shown in Figure 30. The load is at $z = 0$, and the reflection coefficient $\Gamma(z)$ is defined at any point along the transmission-line as V_+/V_-, where V_+ and V_- are the amplitudes of the forward and reflected voltage waves at that point. The model is valid provided that only the TE_{10}-mode propagates in the guide and the slots do not internally couple, that is, the evanescent modes produced by one do not reach the next. The voltage is defined as the integral of the electric field across the center of the guide for the TE_{10}-mode. The following relations will be used. These relate the admittance at a point on a transmission-line to the admittance at any other point on the line, and the reflection coefficient at a point to the admittance at that point, respectively:

$$Y(-l) \;=\; \frac{Y_L + jY_0 \tan kl}{Y_0 + jY_L \tan kl} \tag{101}$$

$$\Gamma_L = \frac{Y_0 - Y_L}{Y_0 + Y_L} \tag{102}$$

Here Y_0 is the characteristic admittance of the line, and Γ_L is the reflection coefficient with everything to the right treated as a load.

Refering to Figure 30, we obtain an expression for the admittance looking to the right from just left of the first slot. It is $Y_1 = G_1 + Y_1'$ where

$$Y_1' \;=\; \frac{Y_2 + jY_0 \tan kl}{Y_0 + jY_2 \tan kl}. \tag{103}$$
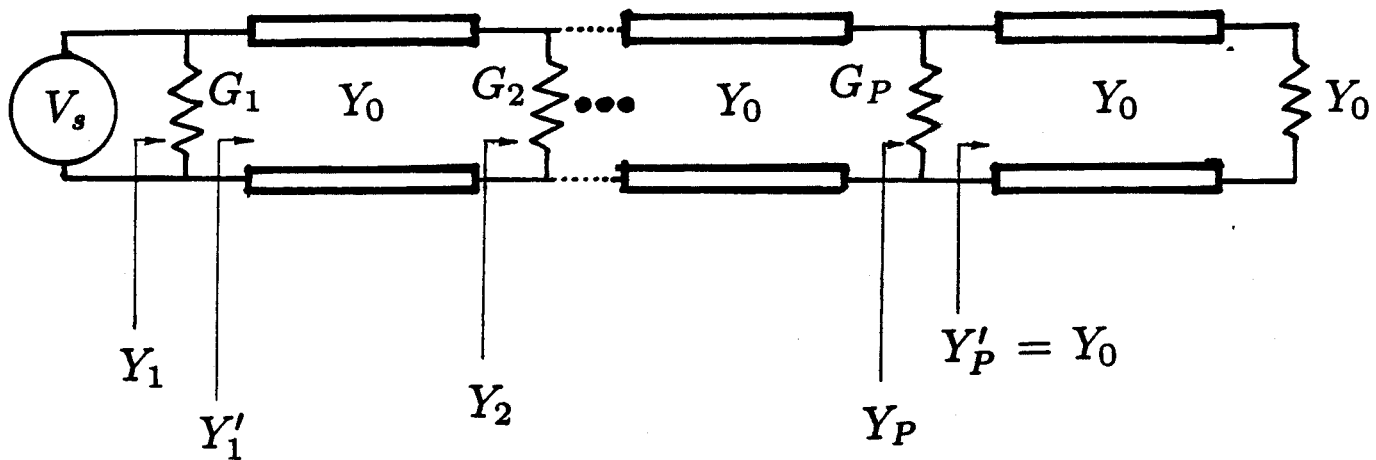
Figure 30: Transmission-line model of the antenna for the coupling problem.
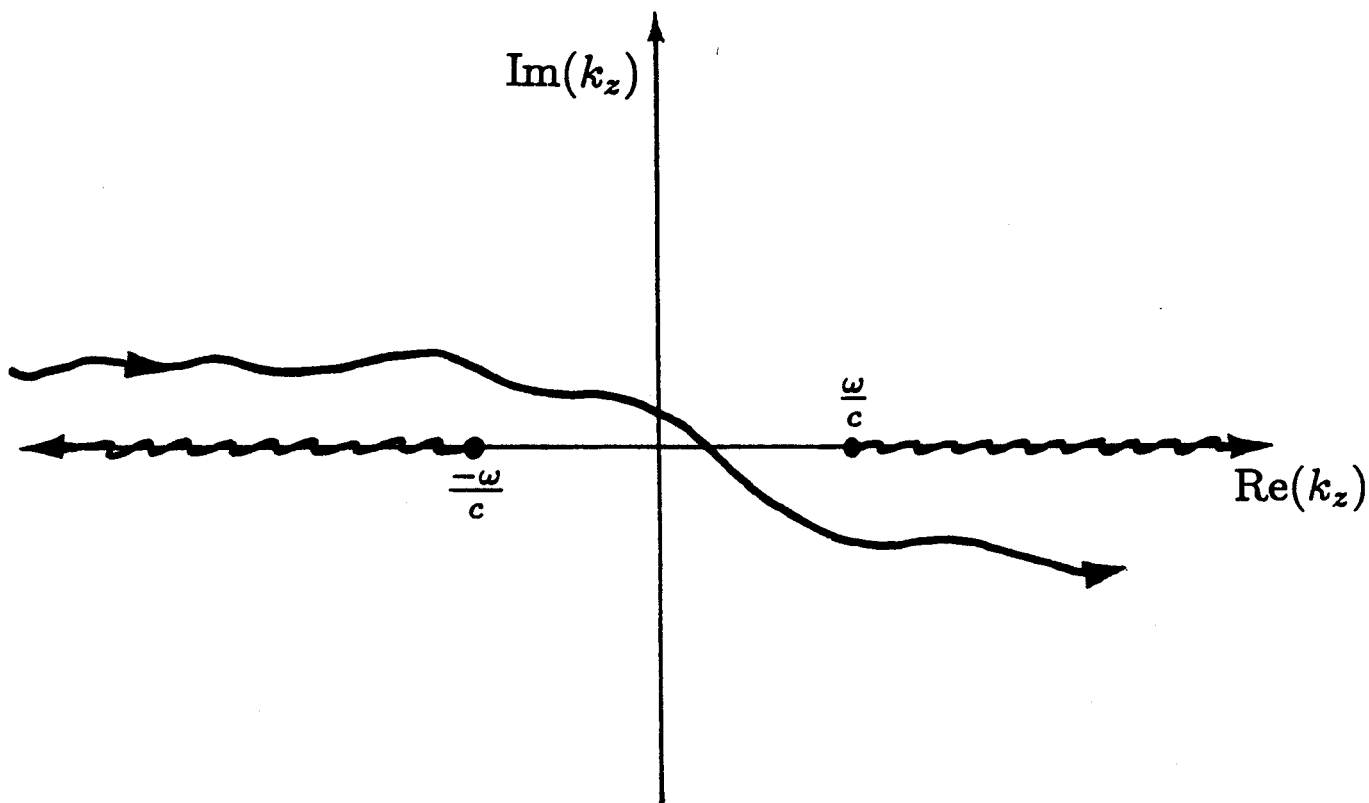
Figure 31: The contour dictated by causality for inverse transforming the wave fields in the complex k-plane.

Note that Y_2 is a function of $G_2, G_3, G_4, \ldots, G_P$.

From Equation 102, $Y_1 = Y_0(1 - \Gamma_1)/(1 + \Gamma_1)$. We now relate Γ_1 to A_1^{10} by writing expressions for the reflection coefficients Γ_1, Γ_1', looking to the right from just left and just right of G_1. this gives $A_1^{10} = bE_s(\Gamma_1 - \Gamma_1')/(1 + \Gamma_1')$. So we have

$$A_1^{10}(\Phi_1, \mathrm{R}_1) = \Delta(E_s, G_1, \ldots, G_P) \tag{104}$$

where E_s is given. Similarly for the pth slot,

$$A_p^{10}(\Phi_p, \mathrm{R}_p) = \Delta[E_p(G_1, \ldots, G_P), G_1, \ldots, G_P] \tag{105}$$

Solving each equation for G_p gives

$$G_p = G_p(\Phi_p, \mathrm{R}_p, G_1, \ldots, G_{p-1}, G_{p+1}, \ldots, G_P) \tag{106}$$

Treating the Φ_p's and R_p's as parameters, this gives P equations for the P unknown G_p's. So we can solve for them, yielding

$$G_p = G_p(\Phi_1, \ldots, \Phi_P, \mathrm{R}_1, \ldots, \mathrm{R}_P). \tag{107}$$

Now we equate the power dissipated in the transmission-line element representing the pth slot to the integrated Ponting flux leaving the slot:

$$\frac{1}{2}(bE_p)^2 G_p = \frac{1}{2}\Re \int_{p\text{th slot}} (\mathbf{E} \times \mathbf{H}) \cdot \hat{x} dA = f_p(\Phi_p, \mathrm{R}_p) \tag{108}$$

where $E_p = E_p(G_1, \ldots, G_P)$.

69

Substituting Equation 107 into Equation 108 gives

$$\frac{b^2}{2} F_p(\Phi_1, \ldots, \Phi_P, R_1, \ldots, R_P) = f_p(\Phi_p, R_p) \tag{109}$$

where $F_p = E_p^2 G_p$.

This gives P equations for the $2P$ unknown amplitudes Φ_p and R_p. An additional set is now obtained using the Brambilla formalism.[38]

The fields in the slots are the following:

$$\mathbf{E}^{slot} = \hat{y} \sum_{p=1}^{P} e^{j\phi_p} \Theta_p(y,z) \left(\Phi_p e^{-j\gamma_1 x} + R_p e^{j\gamma_1 x} \right) \sin k_0(z - z_p) \tag{110}$$

$$\mathbf{H}^{slot} = \sum_{p=1}^{P} e^{j\phi_p} \Theta_p(y,z) \left[\hat{x} \left(\Phi_p e^{-j\gamma_1 x} + R_p e^{j\gamma_1 x} \right) \frac{1}{j\eta_0} \cos k_0(z - z_p) \right.$$
$$\left. + \hat{z} \left(\Phi_p e^{-j\gamma_1 x} - R_p e^{j\gamma_1 x} \right) \frac{\gamma_1}{k_0 \eta_0} \sin k_0(z - z_p) \right], \tag{111}$$

where $\eta_0 = \sqrt{\mu_0/\epsilon_0}$ is the impedance of free space, $\Theta_p = 1$ for $z_p < z < z_p + a$ and $y_p < y < y_p + b$, and $\Theta_p = 0$ otherwise.

The fields in the vacuum region ($x > 0$) can be written as Fourier integrals. They are the following:

$$E_y^V = \int_{-\infty}^{\infty} \left[\sigma(k_y, k_z) e^{-jk_x x} + \rho(k_y, k_z) e^{jk_x x} \right] e^{-jk_y y - jk_z z} \, dk_y \, dk_z \tag{112}$$

$$H_z^V = \frac{1}{\omega \mu_0} \int_{-\infty}^{\infty} k_x \left[\sigma(k_y, k_z) e^{-jk_x x} - \rho(k_y, k_z) e^{jk_x x} \right] e^{-jk_y y - jk_z z} dk_y dk_z. \tag{113}$$

70

To satisfy causality at large positive and negative y and z, we must perform the above integrals along the contours in k_y- and k_z-space shown in Figure 31. Branch cuts must be introduced as shown along the horizontal axes, and the integration path must be above the axis in the left half-plane and below the axis in the right half-plane.[39]

The plasma admittance is defined by[38]

$$\rho(k_y, k_z) = -Y(k_y, k_z)\sigma(k_y, k_z). \tag{114}$$

We now match the vacuum and slot electric-field spectra at $x = 0$. The spectrum of the slot electric-field is defined as

$$\tilde{E}_y^{slot}(k_y, k_z) = \int_{-\infty}^{\infty} \int_{-\infty}^{\infty} E_y^{slot}(y, z) e^{jk_y y + jk_z z} dy\, dz \tag{115}$$

which gives

$$
\tilde{E}_y^{slot} = \sum_{p=1}^{P} e^{j\phi_p} \left(\Phi_p e^{-j\gamma_1 x} + R_p e^{j\gamma_1 x} \right) \left(\frac{e^{jk_y y_p} - e^{jk_y(y_p+b)}}{2k_y} \right)
$$
$$
\times \left[\frac{e^{j(k_0+k_z)(z_p+a)} - e^{j(k_0+k_z)z_p}}{j(k_0+k_z)} - \frac{e^{j(k_z-k_0)(z_p+a)} - e^{j(k_z-k_0)z_p}}{j(k_z-k_0)} \right] \tag{116}
$$

Writing the last two factors in Equation 116 as $F_p(k_y, k_z)$ for compactness, we get, upon matching the electric field spectra at $x = 0$,

$$\sigma(k_y, k_z)\left(1 - Y(k_y, k_z)\right) = \sum_{p=1}^{P} e^{j\phi_p} \left(\Phi_p + R_p \right) F_p(k_y, k_z). \tag{117}$$

71

The magnetic fields must also be matched, but due to surface currents in the wall of the waveguide, the tangential magnetic fields are only equal at the slots. Therefore, the field outside the slots is inverse transformed and matched to $H_z(y, z)$ in the slots, yielding

$$
\frac{1}{k_0 \eta_0} \int_{-\infty}^{\infty} k_x \sigma(k_y, k_z) \Big(1 + Y(k_y, k_z)\Big) e^{-jk_y y - jk_z z} dk_y dk_z
$$
$$
= \sum_{p=1}^{P} e^{j\phi_p} \Theta_p(y, z) \left(\frac{\gamma_1}{k_0 \eta_0}\right) \sin k_0(z - z_p)(\Phi_p + R_p).
$$
(118)

We now use the orthogonality of the waveguide fields to get an equation for the unknown coefficients Φ_p and R_p. Multiplying both sides of Equation 118 by $e^{-j\phi_q} \Theta_q(y, z) \sin k_0(z - z_q)$ and integrating both sides over y and z gives the following:

$$
\frac{e^{-j\phi_q}}{k_0 \eta_0} \int_{z_q}^{z_q+a} \int_{y_q}^{y_q+b} \sin k_0(z - z_q)
$$
$$
\int_{-\infty}^{\infty} \int_{-\infty}^{\infty} k_x \sigma(k_y, k_z) \big(1 + Y(k_y, k_z)\big) e^{-jk_y y - jk_z z} dk_y \, dk_z \, dy \, dz = \frac{ab\gamma_1}{k_0 \eta_0}(\Phi_q + R_q).
$$
(119)

Substituting this into Equation 117, we obtain

$$
\Phi_q + R_q = \frac{2e^{-j\phi_q}}{ab\gamma_1} \int_{z_q}^{z_q+a} \int_{y_q}^{y_q+b} \sin k_0(z - z_q)
$$
$$
\int_{-\infty}^{\infty} \int_{-\infty}^{\infty} k_x \sum_{p=1}^{N} e^{j\phi_p} (\Phi_p + R_p) F_p(k_y, k_z) \left(\frac{1 + Y(k_y, k_z)}{1 - Y(k_y, k_z)}\right) dk_y \, dk_z \, dy \, dz.
$$
(120)

This set of P equations along with Equations 109 can be solved numerically for the Φ_p's and R_p's. If care is not taken when numerically solving this problem,

72

difficulties may arise because the slot fields vary little in the x-direction (because $t \ll 1/\gamma_1$). Note from Equation 117 that if $Y(k_y, k_z) = 0$ (radiation into free space) the shape of the radiated spectrum $\sigma(k_y, k_z)$ is just given by the Fourier transform of the slot fields, corroborating the results of section 2.2.2 and yielding a simple design technique. However, the magnitude of $\sigma(k_y, k_z)$—which gives the total power radiated—must be found by solving the above problem to determine the coefficients Φ_p and R_p.

3 EXPERIMENTAL APPARATUS

3.1 Apparatus for Versator-II Experiment

The Versator-II tokamak is described well in previous theses.[40] [41] The apparatus used for the slotted-waveguide fast-wave coupler experiment on Versator-II consists of the antenna system and the 2.45 GHz rf system, including the power supply, capacitor banks, klystrons, waveguide components, and high- and low-power circuitry for fault detection and control. The rf system is well-described by Mayberry in his doctoral thesis.[10] Diagrams of the high- and low-power circuitry are shown in Figures 32 and 33. The antenna system is shown schematically in Figure 13. For the slotted-waveguide to move radially in the Versator tokamak, several new pieces of hardwave had to be designed and built.

The antenna was constructed from 0.080″ 304 stainless steel sheet stock machined and welded into the curvey piece of waveguide shown. Eight dogbone-shaped slots were cut into the front face before assembling the four walls. The end-flanges, machined from 304 stainless steel, were welded on last and the inner surfaces of all welds were inspected for defects to ensure no points existed where the electric field could concentrate and cause breakdown. The antenna is only 1.4 cm high (short dimension), so that when it was pulled back against the wall of the vacuum vessel, its front surface was at least 0.5 cm from the plasma edge (behind the limiter).

Because the antenna is long toroidally, it occupied two large ports on Versator and required a special system enabling it to move radially under vacuum while clearing the toroidal-field coils and other hardware. This system includes two bellows with port extenders attached to each and angled inward by 22.5° to allow the bellows to work together, as shown in Figure 13.

Two tapers were brazed from 0.080″ copper sheet stock and fitted with brass end-flanges. The tapers transferred power from the WR-340 standard guide of the
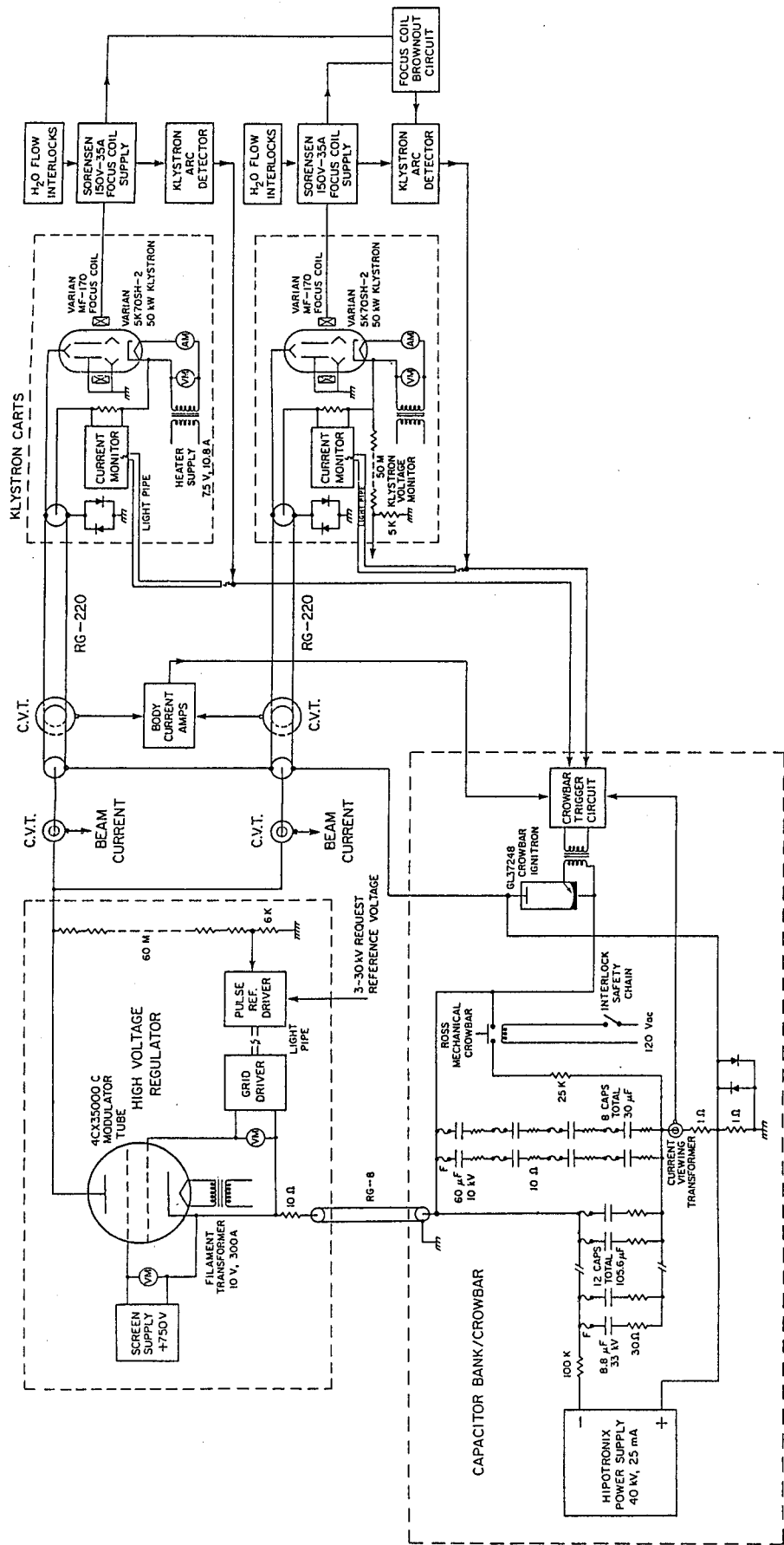
Figure 32: Schematic diagram of the 2.45 GHz rf power supply, including the capacitor banks, modulator tube regulation circuitry, and the klystron connections (from reference [10]).
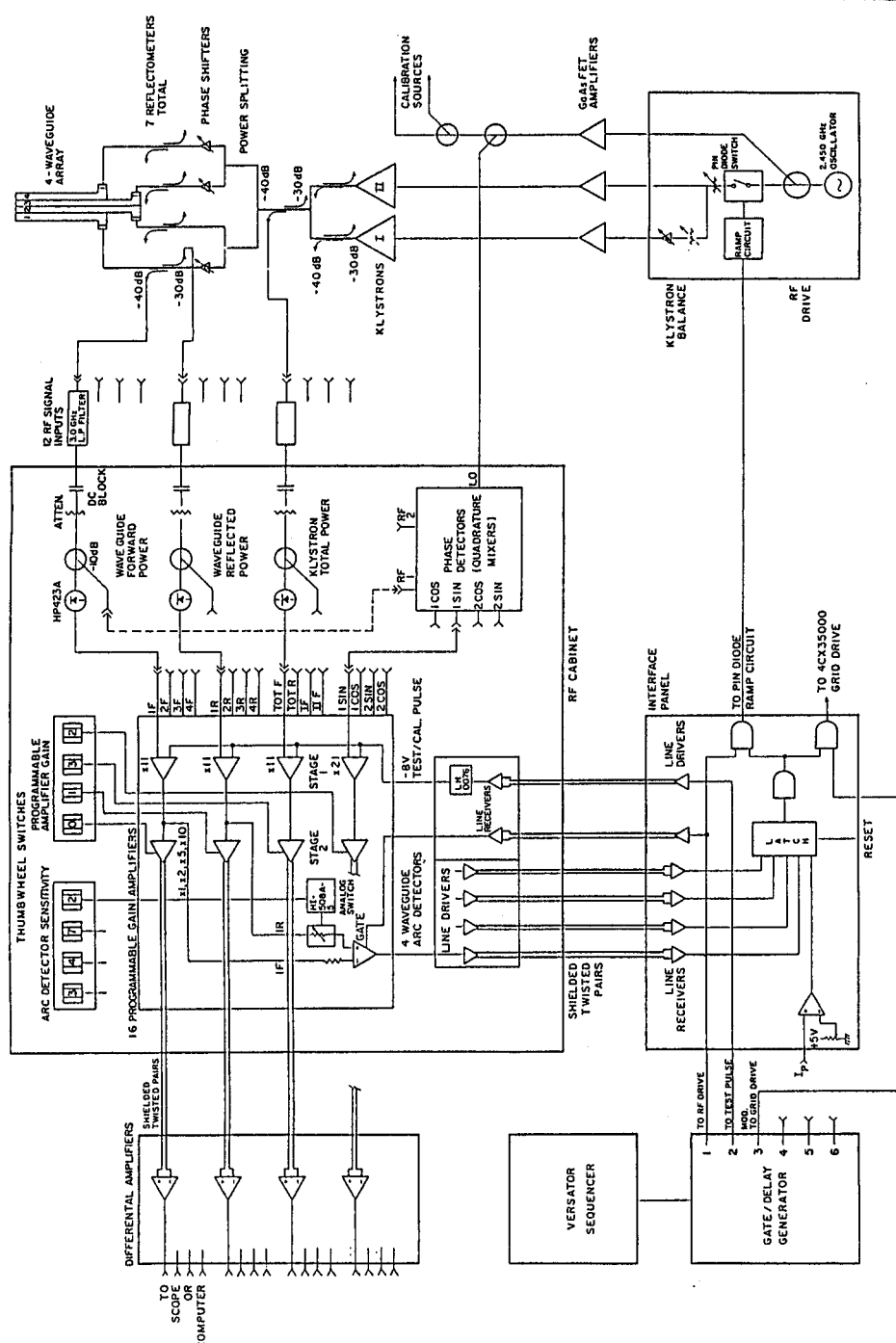
75

Figure 33: Schematic diagram of the low-power rf circuitry, including the drive and the waveguide power-, phase-, and arc-detector circuitry, shown for the original four-waveguide grill (from reference [10]).

directional couplers, matched loads, and all other standard waveguide components to the specially-sized waveguide of the antenna.

The vacuum break was made by two mica windows placed in machined recesses in large stainless steel vacuum flanges covering the bellows openings. Each window was sealed with O-rings and sandwiched between the recess in the stainless-steel flange and a protruding section of the small brass end-flange of the taper, which was bolted to the large flange.

Stainless-steel waveguide sections were constructed to connect the antenna to the large flanges. This was necessary because a single waveguide piece, including the antenna and long enough to pass through the port extenders and bellows, could not fit into the tokamak.

The rf power passed from the klystrons through a directional coupler, which measured the forward and reflected powers. Then it passed through the tapers to the vacuum break at the large flange, traveled through a hole cut in the flange (which acted as a waveguide) and through a stainless steel waveguide section (which passed through the bellows and port extender) to the antenna. The antenna radiated some of the power from its slots, some of the power was reflected, and the rest traveled forward through the second stainless steel waveguide section to the second window and out to the output taper, directional coupler, and matched load.

3.2 Test-Bench Apparatus

The test-bench apparatus is shown in Figure 34. Measurements were made in air of the single-slot conductance and the far-field radiation pattern and polarization. A tunable 30 mW Alfred oscillator was the rf source, and for the far-field

measurements, a traveling-wave-tube amplifier boosted the source power to about 3 W. A 3 GHz low-pass filter was placed on the output of this amplifier to eliminate higher harmonics. The output frequency was tuned to 2.4500 GHz using a resonant-cavity frequency meter. Power was fed via type-n coaxial line to a type-n/WR-340 waveguide transition, then through a taper from WR-340 to the narrow antenna. Power not radiated from the antenna or reflected passed out the other end of the antenna, through a taper, and into a matched load. The matched load was waveguide for the far-field measurements and a waveguide/type-n transition with a 50 Ω termination for the slot conductance measurements.

For the slot conductance measurements, a calibrated bi-directional coupler was placed in the line between the source and the antenna so that the source, reflected, and transmitted powers could be measured with all the slots but one covered (as shown in Figure 35).

The far-field radiation pattern was measured using a 20 dB horn mounted on a rolling tea-cart, as shown in Figure 34. The antenna was carefully aligned on a table, with the radiating face overhanging to prevent the table from interfering with the measurement. The position and orientation of the antenna was fixed relative to a coordinate system defined by the 12.00″ by 12.00″ floor tiles of the room. This coordinate system was accurate to 1%. A pointer was centrally fixed to the tea-cart to locate the center of the horn on the floor grid to within $\frac{1}{16}$″. A nail was embedded in the edge of the table so that its head was directly below the center of the antenna by about 10 cm, and a string was tied from the nailhead to the pointer on the cart, and then to the center of the rear of the cart. By positioning and orientating the cart so that the string was taut and the string sections between the nail and the pointer and the pointer and the rear of the cart were aligned, a circular arc of data points could be swept out with the horn pointed directly at the antenna center. Power received by the horn was measured by a calibrated Hewlett-Packard digital power-meter with a thermal head, and pieces of tape were marked on the floor to record the pointer location for each measurement.

The following pages are missing from the original

pp 79 - 80

4 EXPERIMENTAL RESULTS

4.1 Current-Drive Results

Current was driven with the antenna spectrum both forward and reversed, that is, with the plasma current traveling in the plus and minus $N_\parallel$-directions (see Figure 36). Data sets for typical forward and reverse shots are shown in Figures 37 and 38. When the rf turned on, the plasma current increased over the ohmic value of the previous shot, and the loop voltage was partially supressed. Later in the rf pulse, the density rose by up to 200%, and the hard X-ray and loop voltage signals showed bursts, indicative of the anomalous Doppler instability.[42] The density remained constant or fell during ohmic shots. This is probably because the increased current produced by the rf improved confinement by increasing the poloidal magnetic field.

The driven current was calculated assuming $I_{driven} = (\Delta I/\Delta t)\tau_{L/R}$. The figures of merit $\eta = \bar{n}_e IR/P_{rf}$ for the forward and reverse spectra were 0.007 and 0.0065, comparable to the flattopping figure of merit of 0.0072 obtained by the Versator-II slow-wave grill.[10] This is encouraging considering the relatively poor spectrum of the slotted waveguide used. Current-drive efficiency peaked sharply at densities of $5-7\times10^{12}$ cm^{-3}. Below this density, less current was driven, with no current-drive observed at densities below 2×10^{12}cm^{-3}. This is probably due to poor coupling at low density, and strongly indicates the antenna was coupling to the fast wave. The slow-wave cutoff is at a much lower density of 7.5×10^{10}cm^{-3}, but the fast-wave cutoff density of approximately 3×10^{12}cm^{-3} would explain the observed density threshold for current drive if the antenna were launching the fast wave. If a large fraction of the power launched by the antenna were in the slow wave, more current would be driven at $\bar{n}_e = 2 \times 10^{12}$cm^{-3} than at 5×10^{12}cm^{-3}, but this was not the case.
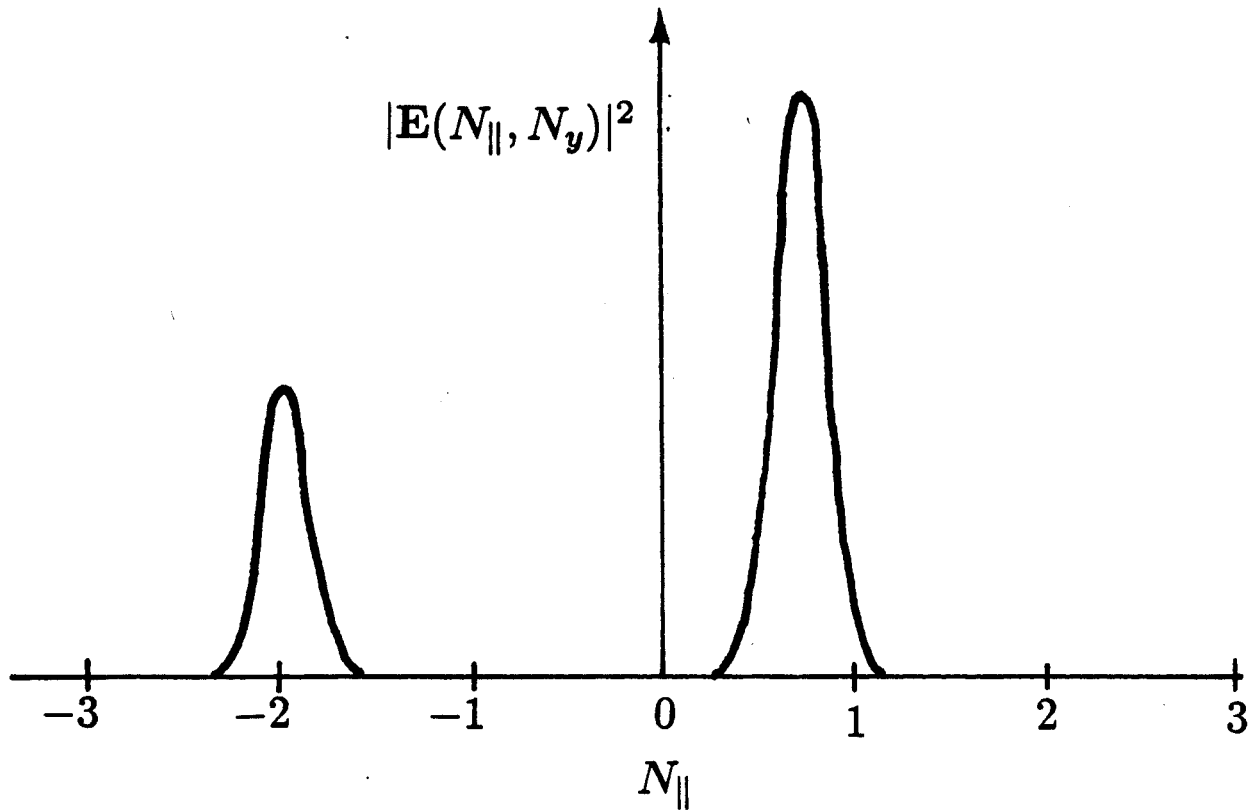
Figure 36: Definition of forward and reverse spectra. A wave with positive $N_\parallel$ travels in the same direction as the power in the waveguide.
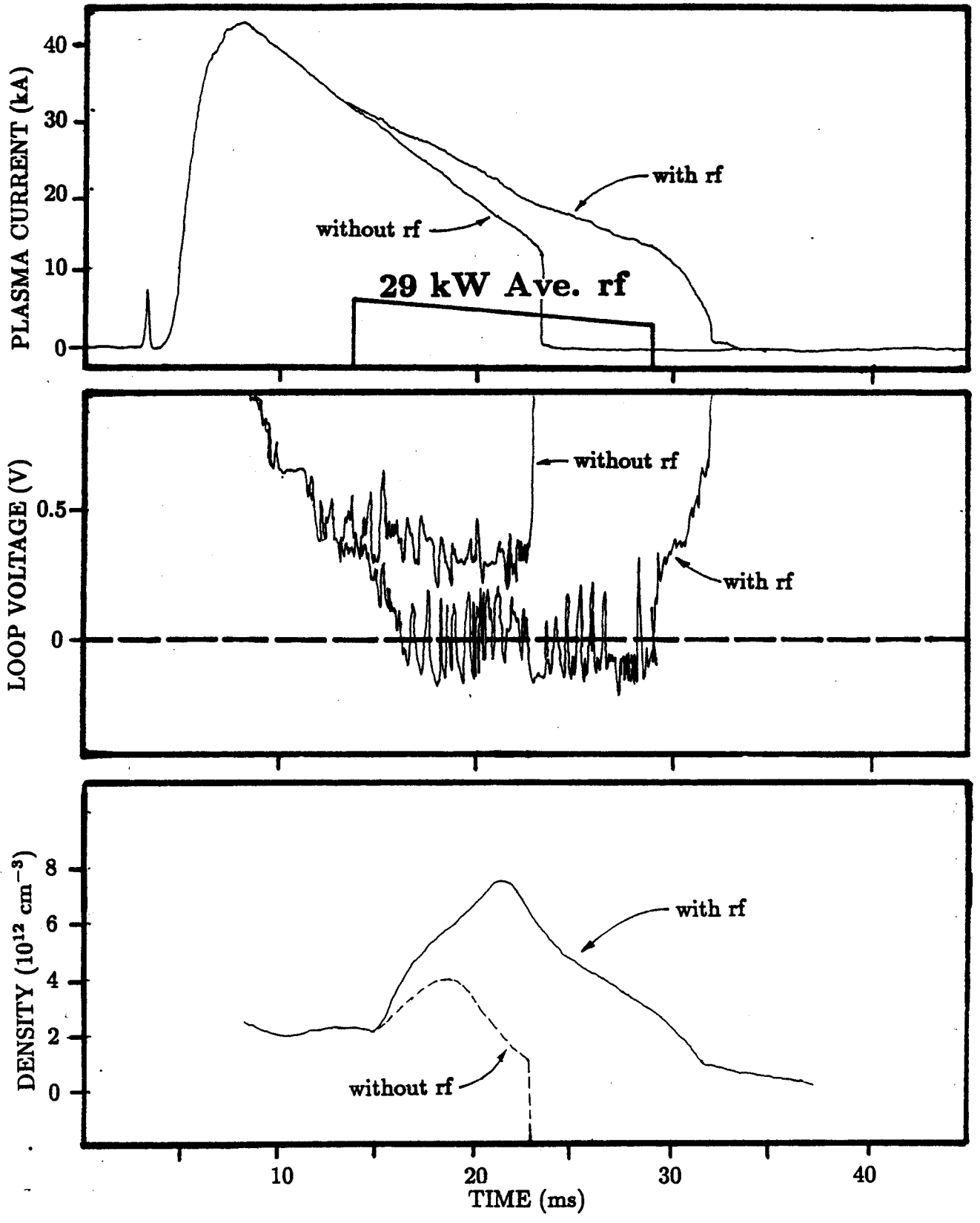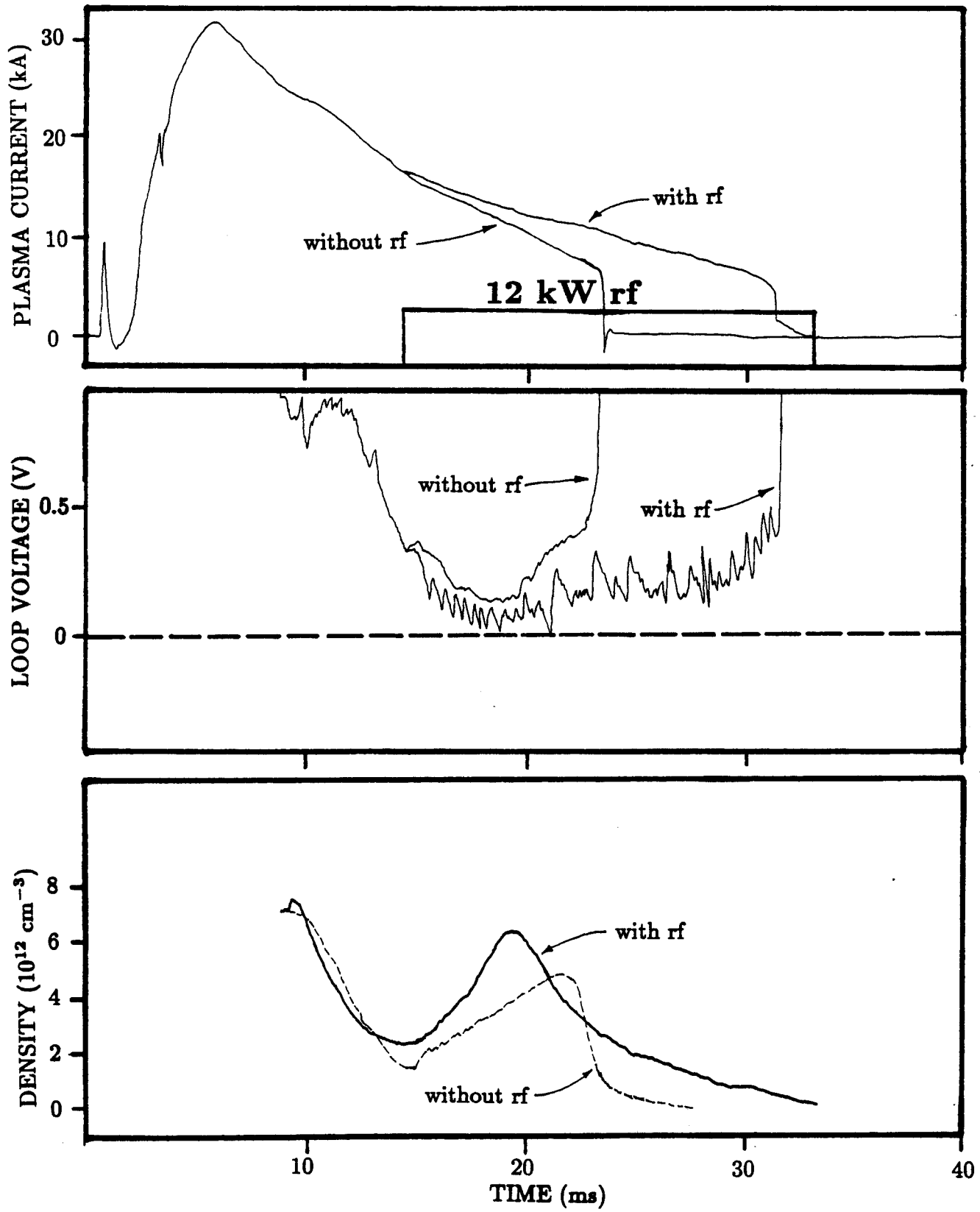
Figure 37: Data for forward shot.

Figure 38:   Data for reverse shot.

No current drive was observed at densities above about $8 \times 10^{12} \text{cm}^{-3}$. This may be due to a lack of source power or to a decrease in tail density. Several of the highest-power shots at $8 \times 10^{12} \text{cm}^{-3}$ drove no noticeable current, while current was driven by similar rf power levels at $6 \times 10^{12} \text{cm}^{-3}$.

Hard X-rays were observed by the large collimated detector placed under the tokamak (see Figure 39).These X-rays increased in intensity through the duration of the rf pulse and abruptly disappeared when the rf shut off, indicating that fast electrons are very poorly confined in Versator.

The current-drive efficiencies were approximately equal regardless of whether the antenna spectrum was forward or reverse. At first, this was puzzling because the antenna spectrum is thought to be asymmetrical. However, this result can be explained as follows.

Curvature of the antenna, toroidal coupling effects, and other approximations made in obtaining the antenna spectrum could cause the spectral peak at $N_\parallel = 0.7$ to be significantly broader than expected, thus containing much power in the range $N_\parallel > 1.0$. The antenna would then radiate significant power in both positive and negative spectral components with $|N_\parallel| > 1$. In this case it is possible that current could be driven equally well with a forward or reverse spectrum because the waves traveling in the direction of the electron tail (pre-formed by the ohmic transformer) would Landau damp on fast, current-carrrying electrons, driving current, and waves traveling in the opposite direction, having no preformed tail to damp on, would have little effect. This is shown schematically in Figure 40.

4.2 Coupling Results

The radiating efficiency of the antenna was measured as a function of radial position and plasma density, for the forward and reverse spectra. The radiating
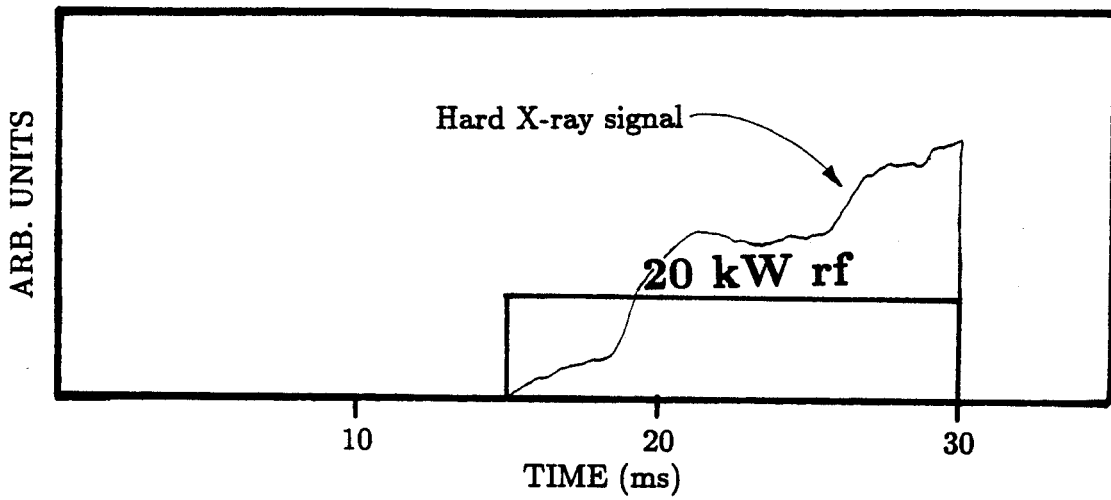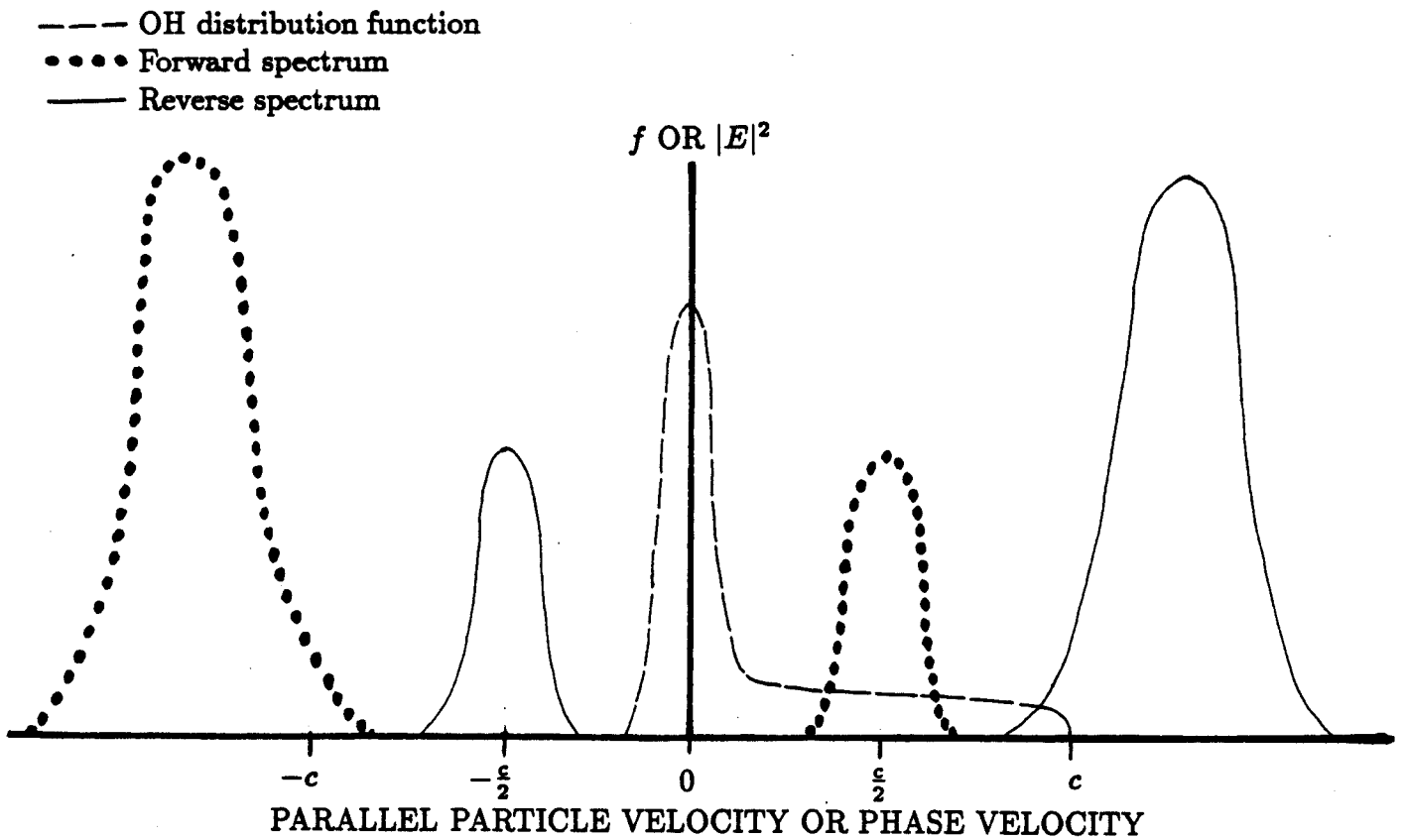
Figure 39:   Hard X-ray Data.

Figure 40:   Possible situation allowing equal current-drive
efficiencies for forward and reverse spectra (see text).

efficiency is defined as the power radiated out the slots divided by the total forward power coming from the klystrons. It is not a true measure of coupling efficiency, because much power may be radiated from the antenna that is not coupled to the fast wave in the plasma. This power may be coupled to surface waves or bounce between the fast-wave cutoff layer and the antenna or vacuum-chamber wall until it is collisionally damped at the plasma edge or is scattered into the slow-wave polarization and coupled to the plasma.

The interpretation of the coupling results is complicated because the calculated spectrum has two-thirds of its power in a large peak at $N_{\parallel} = 0.7$, and one-third in a peak at $N_{\parallel} = -2.0$. Spectral components with $|N_{\parallel}| < 1$ can propagate in free-space, but not in plasma, and components with $|N_{\parallel}| > 1$ propagate in plasma, but not in free-space. Therefore, when the antenna is placed at the edge of the plasma, it is difficult to assess what region of the spectrum is being radiated, or what percentage of the radiated power has $N_{\parallel} = 0.7$ and what percentage has $N_{\parallel} = -2.0$. As the antenna is moved farther away from the plasma, the peak at $N_{\parallel} = 0.7$ should begin to radiate, possibly bouncing between the fast-wave cutoff layer and the antenna and "leaking" out toroidally or poloidally. Concurrently, the peak at $N_{\parallel} = -2.0$ should become more strongly evanescent and the amount of power near this spectral component tunnelling to the fast-wave cutoff layer should be very small. On the other hand, as the antenna is moved up to the plasma, past the limiter, the spectral components near $N_{\parallel} = 0.7$ should be sharply reflected back into the waveguide, and the power at $N_{\parallel} = -2.0$ should tunnel most effectively to the fast-wave cutoff.

Because only the spectral components with $|N_{\parallel}| > 1$ can couple to the fast wave, the radiated power does not truly measure the coupling efficiency of the antenna. In fact, the radiating efficiency of the antenna in free-space, say, five feet from the plasma, when no power is coupled to the fast wave, should be twice that when the fast wave cutoff is at the antenna, and all the radiated power is coupled.

Without a direct measurement of the amplitude of the various spectral components in the plasma right in front of the antenna, it is impossible to know the

coupling efficiency of the components with $|N_\parallel| > 1$ as a function of antenna radial position (ARP). However, some information can be obtained from the radiating efficiency.

The radiating efficiencies are shown in Figure 41a and 41b as a function of the ARP for a density of $8 \times 10^{12} \text{cm}^{-3}$. The directional couplers were calibrated more carefully for the forward spectrum measurements.

The radiating efficiency increased slightly as the antenna was moved farther outside the limiter, and it was relatively constant for ARPs inside the limiter. This is consistent with the picture described above. Once the antenna is moved inside the limiter, it becomes the limiter itself, and the edge plasma characteristics probably change little relative to the antenna as it is moved in and out. However, as the antenna is moved outside the limiter, the power peak at $N_\parallel = 0.7$ radiates more and the peak at $N_\parallel = -2.0$ radiates less. Because the peak at $N_\parallel = 0.7$ carries twice the power of the peak at $N_\parallel = -2.0$, the net radiating efficiency goes up. A similar, but much weaker, dependence of the radiating efficiency on ARP was observed at a lower density of $2 \times 10^{12} \text{cm}^{-3}$.

Figure 42 is a plot of radiating efficiency versus density for a forward spectrum. The radiating efficiency increased moderately with plasma density when the antenna was inside the limiter. This indicates the antenna was launching the fast wave. If the slow wave were the dominant mode launched, the radiating efficiency would be independent of density for densities at the antenna above 10^{11}cm^{-3} or so.

The density at the antenna was measured to be well above this threshold, as shown in Figure 43. For a shot with a line-averaged central-chord density of $1 \times 10^{13} \text{cm}^{-3}$, the approximate line averaged density near the edge was $2 \times 10^{12} \text{cm}^{-3}$. The actual density 1 cm from the plasma was probably higher, because at the edge, the interferometer averages over a greater proportion of vacuum than at the central position.

Coupling versus density was not measured for ARPs outside the limiter radius nor for the reversed spectrum.
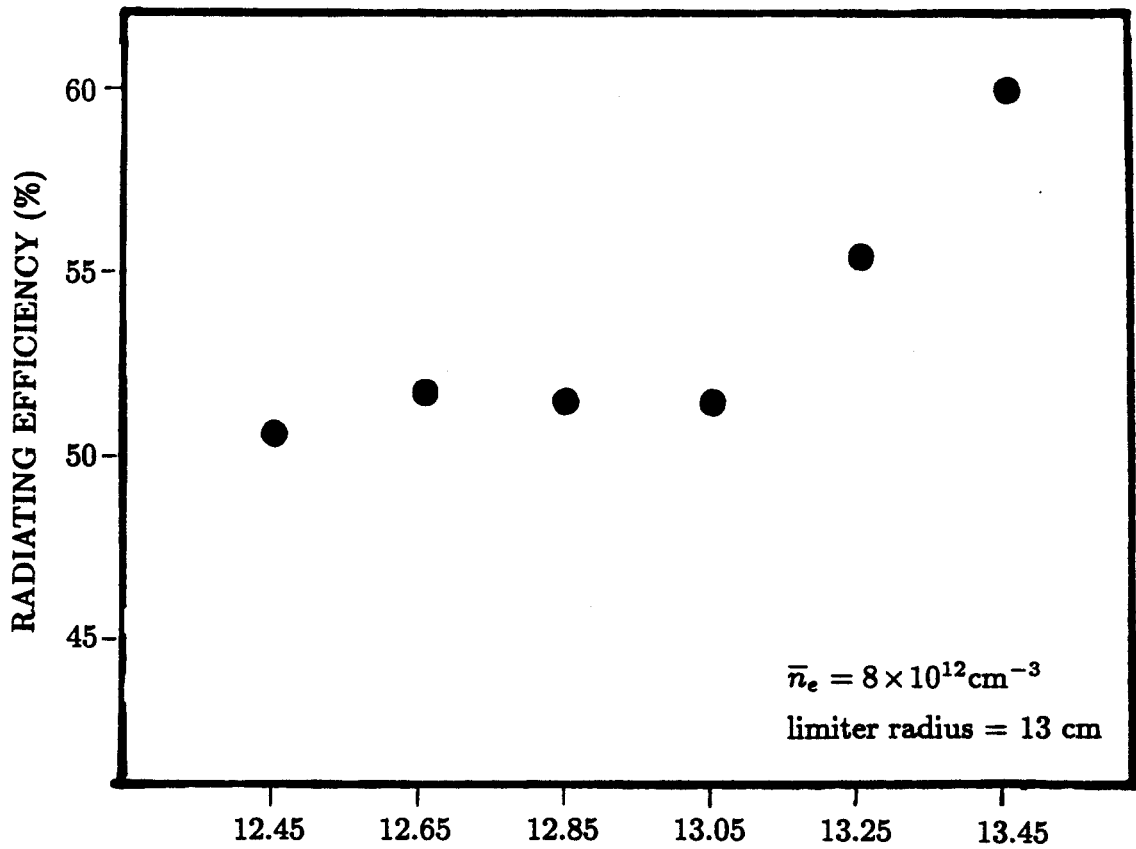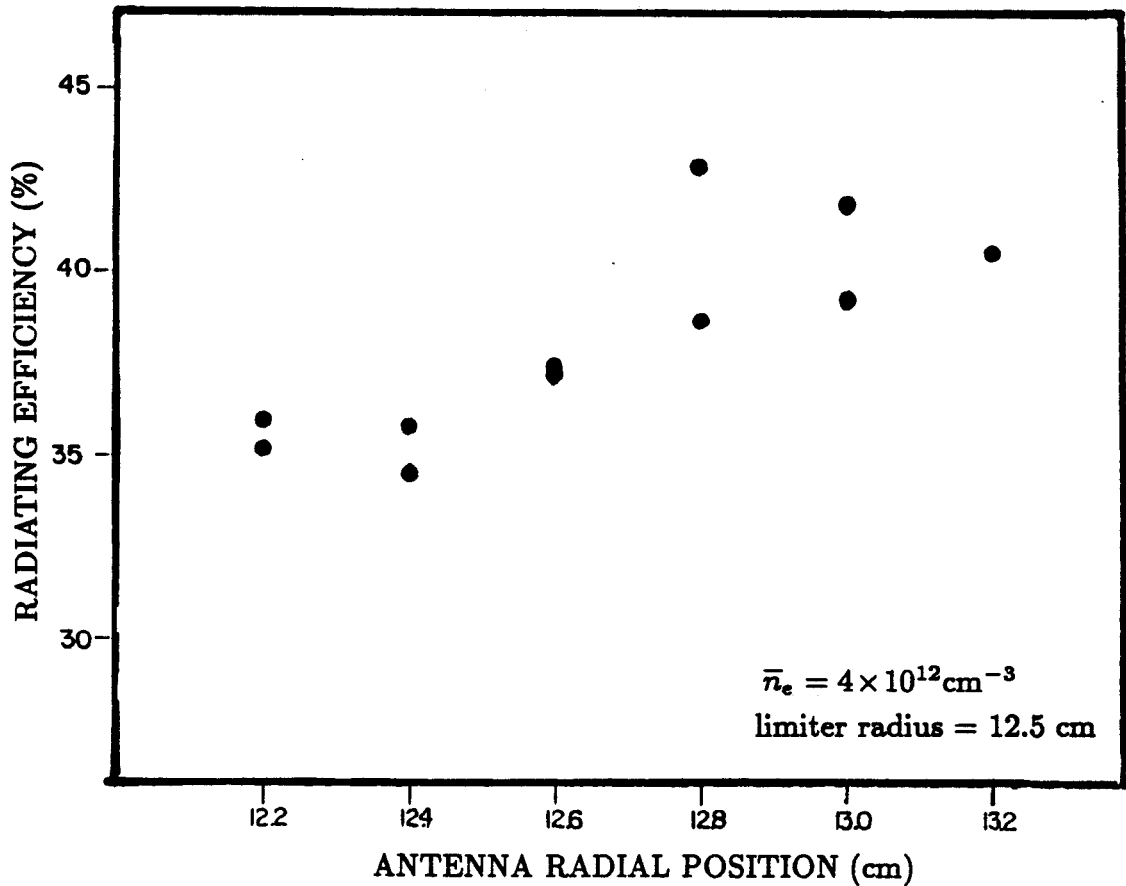
Figure 41a: Radiating efficiency versus ARP for forward spectrum.

Figure 41b: Radiating efficiency versus ARP for reverse spectrum.
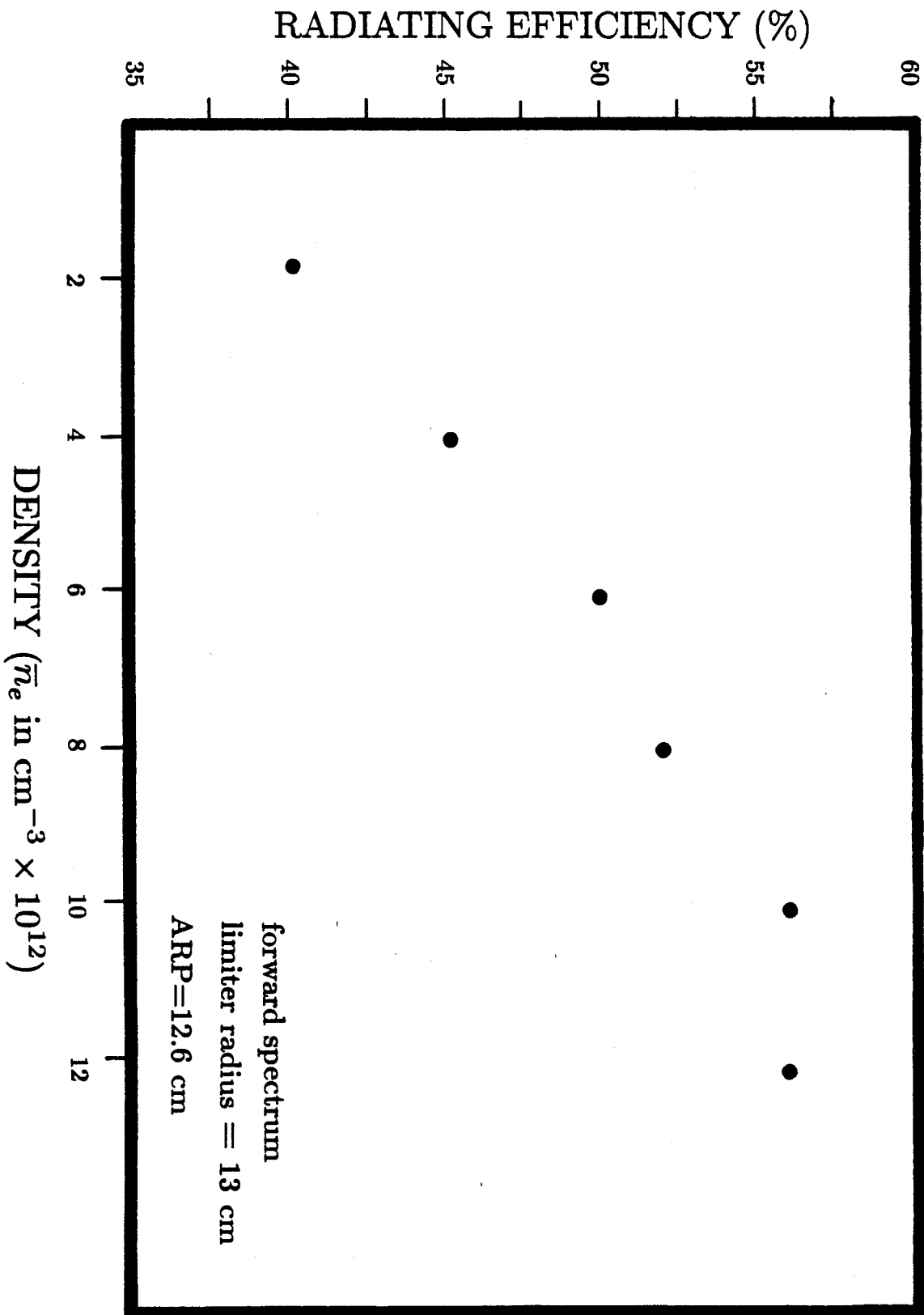
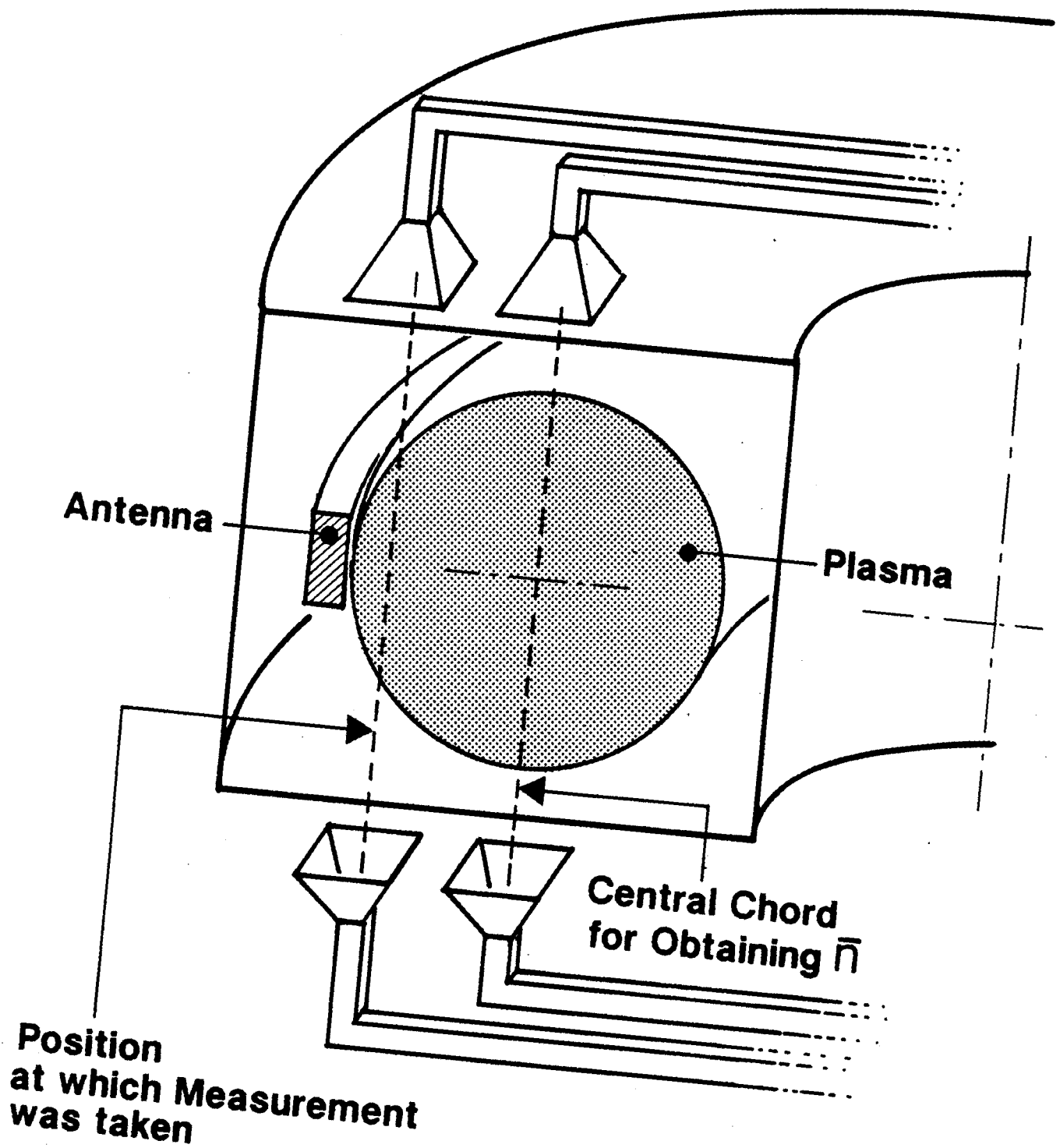Figure 42: Radiating efficiency versus density.

Antenna

Plasma

Central Chord for Obtaining $\bar{n}$

Position at which Measurement was taken

Figure 43:   Schematic diagram showing edge-density measurement.

4.3 Test-Bench Results

The single slot conductance, far-field radiation pattern, and far-field polarization were measured in air. The slot conductance was measured by covering all but one of the slots with copper tape, feeding power into one end of the antenna, and measuring the source, reflected, and transmitted powers. The theoretical normalized slot conductance g is 2.18, as given by Equation 85. To compute the measured conductance, g must be related to the incident and radiated powers.

The radiated power is given by

$$P_{rad} = \frac{1}{2}GV^2 = \frac{1}{2}gY_{10}E_{gs}^2b^2 \tag{121}$$

where G is the slot conductance, V is the guide "voltage" at the slot, defined as $E_{gs}b$, Y_{10} is the characteristic admittance of the TE_{10}-mode in the guide, and E_{gs} is the field of the TE_{10}-mode in the center of the guide at the slot.

The relevant fields for the TE_{10}-mode are

$$\mathbf{E} = \hat{y}E_{0g}\sin\frac{\pi x}{a}e^{-j\beta z} \tag{122}$$

$$H_x = Y_{10}E_{0g}\sin\frac{\pi x}{a}e^{-j\beta z} \tag{123}$$

where $Y_{10} = H_x/E_y = \beta/\omega\mu_0$. The incident power is given by

$$P_{inc} = \frac{1}{2}\int_{WG} E_y H_x^* \, dS = \frac{ba}{4}Y_{10}E_{0g}^2. \tag{124}$$

92

Due to reflection from the slot, E_{0g} and E_{gs} are not identical. They are related by the following:

$$E_{gs} = (1 + \Gamma)E_{0g} = \left(1 + \frac{1 - \Gamma_g - g}{1 + \Gamma_g + g}\right) E_{0g} \qquad (125)$$

where Γ_g is the reflection coefficient associated with the portion of the guide downstream from the slot.

Solving for E_{0g} in Equation 124, plugging into Equations 121 and 125 and solving for g gives

$$g = \frac{2}{f} - 1 - \Gamma_g \pm \frac{1}{2f}\sqrt{(2f + 2f\Gamma_g - 4)^2 - 4f^2 - 8f^2\Gamma_g - 4f^2\Gamma_g^2} \qquad (126)$$

where $f = aP_{rad}/2bP_{inc}$. Assuming $\Gamma_g = 0$ and plugging in the values measured for P_{inc} and P_{rad} yields $f = 0.17$ and $g = 19.32$ or 0.21 as possible solutions. The first solution is an order of magnitude higher than the design value of $g \approx 2$ and the second is an order of magnitude too low. The first solution should be discarded as unphysical. In design, it was intended that each slot have a conductance of about 0.5, but due to a computational error, each was placed such that its conductance was 2.18. For this placement, the theory used to predict the slot conductance is probably invalid. Also, the conductance measurement was very crude, with roughly one-third of the source power unaccounted for. This was ten times the radiated power. Given these problems, it is not surprising that the measured and predicted values for the slot conductance do not agree.

Agreement with theory was better for the far-field measurements. The radiated power as a function of $N_{\parallel}$ (or $\sin\theta$) is shown in Figure 44. The lobe at $N_{\parallel} \approx 0.7$ should be compared with that at $N_{\parallel} \approx 0.7$ in Figure 26. Some of the secondary

maxima may correspond to the ripples shown in Figure 26, or they may be caused by multiple reflections from the walls of the room.

The ×- and ⊗-marks on Figure 44 show relative power in the vertical and horizontal components of the electric field. These were measured by rotating the receiving horn 90°. The waveguide between the horn and the power meter was sufficiently long to prevent any but the dominant TE_{10}-mode from contributing to the power reading. This measurement shows that at the main lobe (where the bulk of the power is radiated), the ratio $P_{vert}/P_{hor} = |E_y|^2/|E_z|^2 \approx 12$. This is encouraging because the antenna was designed to launch waves with only vertical polarization.

4.4 Performance of Components

The antenna, bellows system, and klystrons performed well. The vacuum windows, capacitor banks, and control system performed poorly.

Apparently, the antenna did not arc throughout the experiment. It withstood considerable mechanical stress at times and was not damaged whatsoever by the plasma, even though it was the limiter for most of the shots. The port extenders worked well and the bellows, although somewhat tedious to adjust, withstood several severe compressions and expansions without leaking. The klystrons performed reliably throughout the experiment.

The mica vacuum windows repeatedly failed (see Figure 45). Apparently the rf caused severe arcing on the window surface, which led to disintegration of the mica. This occurred even to carefully cleaned windows. The damage may have been avoided by eliminating the slight jog in the waveguide at the large vacuum
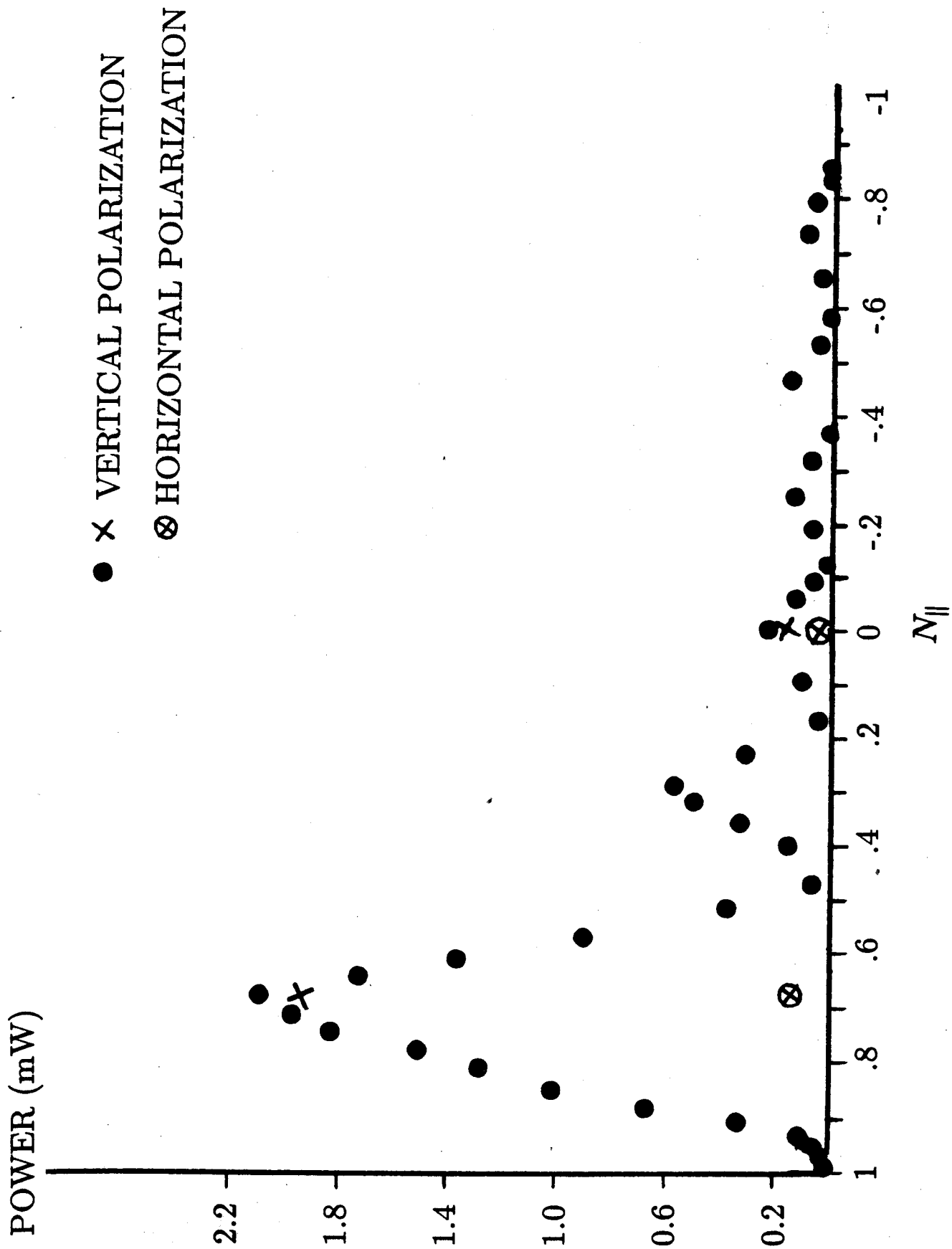
94

Figure 44: Far-field pattern and polarization data.
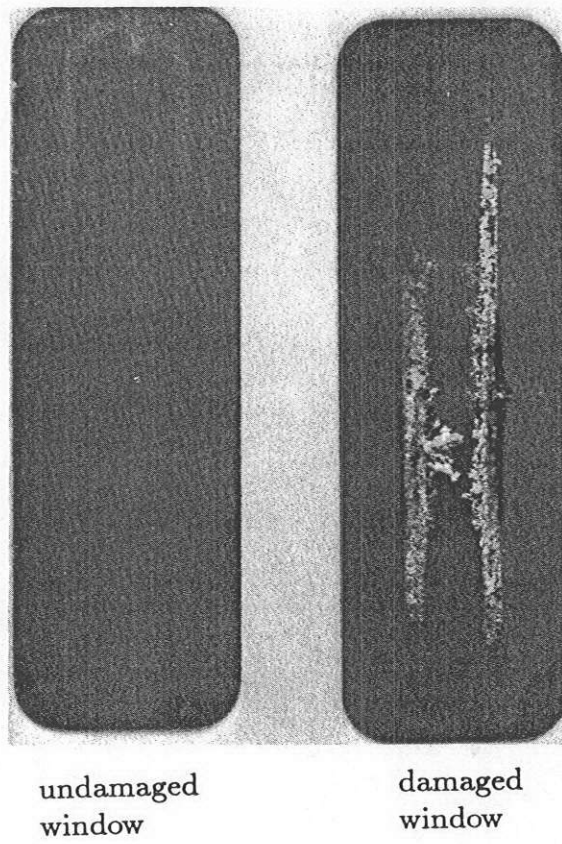
undamaged
window

damaged
window

Figure 45: Mica vacuum window destroyed by rf.

flange, but this is unlikely. The small reflection that may have been produced by this jog probably would not have been enough to cause the persistent and rapid destruction of the mica windows. On the average, one window was destroyed for every thirty to fifty plasma shots with high energy rf. This caused extensive delays because a vacuum break was needed each time a window failed. The problem could best be solved by using a window material with better microwave properties, such as ceramic.

The second major problem experienced was persistent tripping of the capacitor bank crowbar-circuit by the termination of the plasma discharge. Presumably this was due to ground loops. During current-drive operation, this happened every other shot at times. Recharging the capacitor bank usually required a few minutes, precluding data-taking for the subsequent shot. The problem could be solved by carefully checking the entire rf system for ground loops and completely isolating it electrically from the tokamak and its controls.

Lastly, the failure of one of the two capacitor banks, requiring its disconnection, limited the power-pulselength product of the klystron output to about 250 kW·msec before noticeable power droop occurred.

5 CONCLUSIONS AND FUTURE WORK

The slotted-waveguide antenna used on Versator-II launched the fast wave, as indicated by the coupling results and the absence of current drive at low densities. Current was driven by the antenna, and the efficiency was similar to that of the slow wave, although as little as one-third of the power launched from the antenna may have been coupled to the plasma. It was not possible to test the "density limit," because no abrupt density limit was observed previously with the slow-wave launcher at 2.45 GHz. In these previous experiments[10] and in the present fast-wave experiment, no noticeable current was driven at higher densities probably due to insufficient source power. It may be that, as probably happened on the 800 MHz experiments on PLT and JIPT-IIU, the slotted-waveguide launched the fast wave, but much power was mode-converted to the slow wave via a toroidal $N_\parallel$-shift, and the slow wave, which has a much higher Landau damping rate, drove most of the current.

The slotted-waveguide can be greatly improved by using probe-fed slots,[36] [37] as shown in Figure 15. The depth of each probe determines the conductance of the slot, and the location (above or below the slot) determines the polarization (up or down) of the radiated fields. Thus a phase shift of π radians can be introduced between adjacent slots in addition to the phase shift caused by their separation. This greatly improves the spectrum, as shown in Figure 27. Note the absence of significant power in spectral components with $|N_\parallel| < 1$. This eliminates the ambiguity in coupling and current-drive efficiency caused by the spectral peak at $N_\parallel = 0.7$. The fraction of power in desireable spectral components (near $N_\parallel = -2.0$) is double that of the present antenna, theoretically doubling the efficiency. It is unclear whether twice the power would be radiated or the ratio of power coupled to the plasma over power radiated would double. This depends on whether or not the

spectral components near $N_\parallel = 0.7$ from the present antenna were reflected back into the guide.

If future work goes as planned, a slotted-waveguide fast-wave coupler with probe-fed slots will be designed, constructed, and used on Versator. The probes will be tuned to maximize the radiated power, and ceramic vacuum windows will be used in an attempt to eliminate window disintegration. The control system will be checked extensively for ground-loops to eliminate high voltage trips during plasma discharge termination. The feasibility of detecting the fast wave in the plasma by microwave scattering will be determined, and the conjecture of mode-conversion to the slow wave will be tested by attempting to scatter off the slow wave. Finally, the coupling theory outlined in section 2.3 will be implemented in a computer code with a full electromagnetic form for the plasma admittance matrix $\overline{\overline{Y}}$, and ray-tracing and dispersion codes will be written.

REFERENCES

[1] Lawson, J.D., *Proc. Phys. Soc.*, Sect. B **70**, 6 (1957).

[2] Tamm, I.E., and Sakharov, A.D., in *Plasma Physics and the Problem of Controlled Theromonuclear Reactions, Vol. 1* edited by M.A. Leontovich (Pergamon Press, New York, 1961).

[3] Fisch, N.J., *Phys. Rev. Lett.* **41** 873 (1978).

[4] Ikuta, K., *Jpn. J. Appl. Phys.* **11** 1684 (1972).

[5] Fisch, N.J., *Nucl. Fusion* **24** 378 (1984).

[6] Bellan, P.M.,*Phys. Fluids* **27** 2191 (1984).

[7] Finn, J.M., and Antonsen, T.M. Jr., *Phys. Fluids* **30** 2450 (1987).

[8] Parker, R.R., MIT Plasma Fusion Center (1985).

[9] Porkolab, M., 8.624 course notes (unpublished).

[10] Mayberry, M.J., Ph.D. Thesis, Dept. of Physics, Massachusetts Institute of Technology (1986).

[11] Cordey, J.G., *Plasma Phys. and Controlled Fusion* **26**, 123 (1984).

[12] Fisch, N.J., and Boozer, A.H., *Phys. Rev. Lett.* **45** 720 (1980).

[13] Antonsen, T.M. Jr., in *Wave Heating and Current Drive in Plasmas*, V.L. Granatstein and P.L. Colestock, Eds. New York: Gordon and Breach, 1985, p. 287.

[14] Karney, C.F.F., and Fisch, N.J., *Phys. Fluids* **28** 116 (1985).

[15] Yamamoto, T., *Phys. Rev. Lett.* **45** 716 (1980).

[16] Luckhardt, S.C., et. al., *Phys. Rev. Lett.* **48** 152 (1982).

[17] Bernabei, S., et. al., *Phys. Rev. Lett.* **49** 1255 (1982).

[18] Porkolab, M., et. al., *Phys. Rev. Lett.* **53** 450 (1984).

[19] Mayberry, M.J., et. al., *Phys. Rev. Lett.* **55** 829 (1985).

[20] Pinsker, R.L., *Twenty-Eighth Annual Mtg., Div. Plasma Phys.* poster session (1986).

[21] Ando, R., et. al., *Nucl. Fusion* **26** 1619 (1986).

[22] Okhubo, K., et. al., *Phys. Rev. Lett.* **56** 2040 (1986).

[23] Yamamoto, T., et. al., Report JAERI-M 86-115 (1986).

[24] Goree, J., et. al., *Phys. Rev. Lett.* **55** 1669 (1985).

[25] Parker, R.R., MIT Plasma Fusion Center, private communication (1987).

[26] Golant, V.E., *Sov. Phys. Tech. Phys.* **16** 1095 (1962).

[27] Bonoli, P., MIT Plasma Fusion Center, private communication (1987).

[28] Bers, A., MIT Plasma Research Report No. PRR78/8, Feb., 1978.

[29] Andrews, P.L., and Bhadra, D.K., *Nucl. Fusion* **26** 897 (1986).

[30] Porkolab, M., et. al., *Phys. Rev. Lett.* **38** 230 (1977).

[31] Tripathi, V.K., *Phys. Fluids* **27** 2869 (1984).

[32] Eaton, J.E., et. al., in *Microwave Antenna Theory and Design*, S. Silver, ed. New York: McGraw-Hill, 1949, pp. 287-295.

[33] Stevenson, A.F., *J. Appl. Phys.* **19** 24 (1948).

[34] Booker, H., TRE Report No. T-1028.

[35] Dodds, J.W., et. al., McGill University Report No. PRA-104, Canada.

[36] Eaton, J.E. *op. cit.* p. 299.

[37] Clapp, R.E., MIT Radiation Laboratory Report No. 455, Jan. 25, 1944.

[38] Brambilla, M. *Nucl. Fusion* **16** 47 (1976).

[39] Pinsker, R.I., et. al., *Nucl. Fusion* **26** 941 (1986).

[40] Richards, B., Ph.D. thesis, Dept. of Physics, Massachusetts Institute of Technology (1981).

[41] Knowlton, S.F., Ph.D. thesis, Dept. of Physics, Massachusetts Instiute of Technology (1983).

[42] Luckhardt, S.C., et. al., MIT Plasma Fusion Center Report No. JA-84-42, December 1984.